

**A micromechanical investigation of biomimetic composites: experimental
characterization and three-dimensional computational modeling**

by

Aram Bahmani

A thesis

presented to the University of Waterloo

in fulfillment of the

thesis requirement for the degree of

Master of Applied Science

in

Mechanical and Mechatronics Engineering

Waterloo, Ontario, Canada, 2018

© Aram Bahmani 2018

Author's Declaration

I hereby declare that I am the sole author of this thesis. This is a true copy of the thesis, including any required final revisions, as accepted by my examiners.

I understand that my thesis may be made electronically available to the public.

Abstract

Biological and natural composites have been naturally optimized over millions of years. These materials benefit from high-performance responses under various loading conditions. Mimicking these materials offers the opportunity of understanding materials-design key features; and hence, the chance of developing such a high-performance material with synthetic constituents. The main objectives of this research are summarized as follows:

- (i) Develop a computational tool for assessing the elastic responses of biomimetic composites using 3D finite element micromechanical modeling.
- (ii) Make a 3D-printable nanocomposite ink comprised of a plant oil-based polymer and nanoparticles for bone-mimetic applications.
- (iii) 3D printing nanocomposite filaments having staggered nanostructures and testing in order to validate 3D micromechanical models using mechanical properties.

Two 3D finite element micromechanical models were developed to study biomimetic composites with non-uniformly dispersed staggered hexagonal platelets and cylindrical inclusions. A novel algorithm termed staggered hardcore algorithm (SHCA) was used to rapidly generate 3D periodic representative volume elements (RVE) for these types of microstructures. The spatial dispersions of inclusions in these generated 3D RVEs were assessed using autocorrelation analysis, demonstrating the effectiveness of the SHCA algorithm. A new technique was developed within the commercial finite element software ABAQUS to produce required matching mesh patterns on opposite surfaces of the 3D RVE, and to apply the corresponding periodic boundary conditions (PBCs) using custom PYTHON scripts. To verify the developed 3D RVEs, orthotropic elastic properties were computed and compared with available experimental data from literature for nacre-mimetic and short-fiber composites. Also, these data were compared with established

analytical models, namely modified shear-lag, Mori-Tanaka and Halpin-Tsai. These comparisons showed that 3D RVE predictions had excellent correlations with experimental data. The capabilities of the computational model were further demonstrated through a comparative study of orthotropic elastic constants for the cylindrical and hexagonal inclusion composites. The study revealed the necessity to use 3D micromechanical models with realistic inclusion dispersions for accurately assessing the response of high inclusion volume fraction biomimetic composites. These 3D RVE models were also validated and compared with experimental data obtained in this study.

Three-dimensional printable nanocomposite inks consisting of a plant oil-based polymer (epoxidized soybean oil acrylate (SOEA)), and nanohydroxyapatite (nHA) particles were made for different nHA volume fractions. Silanization process was implemented on nHA particles to enhance bonding between nHA and biopolymeric resins. A second ink was made by adding an additional monomer 2-hydroxyethyl acrylate (HEA) to SOEA for improving the rheology of the ink. Also, ethanol (EtOH) was employed during ink preparation to improve nHA particles dispersions. Using these two inks, bone-mimetic filaments with staggered nanostructures were fabricated with direct ink writing (DIW) technique. Thermogravimetric analysis (TGA), scanning electron microscopy (SEM), and energy-dispersive X-ray spectroscopy (EDX) were performed to characterize the material microstructure. These analyses revealed actual nHA volume fractions, the effective value of Si on nHA, as well as, nHA dispersions and alignments in different regions of 3D-printed nanocomposite inks. A number of uniaxial tensile tests using a very small universal machine and digital image correlation (DIC) measurements were conducted to determine the mechanical properties of biopolymeric resins and 3D-printed nanocomposite filaments. 17%Si-nHA/SOEA+HEA and 20% Si-nHA/SOEA ink had perfectly dispersed and aligned nanoparticles. Thus, the strength and toughness of SOEA+HEA and SOEA had been remarkably improved.

The extracted experimental data for both biopolymeric resins were used to run 3D finite element micromechanical models. While the experimental data for the nanocomposite filaments were employed to validate the 3D FE micromechanical models. Eventually, the results of 3D RVEs were compared with measured experimental data and Mori-Tanaka prediction. According to notable difference between the stiffness of biopolymeric resins and nanohydroxyapatite inclusions, the predictions of 3D RVEs were correlated well with experimental data particularly for Si-nHA/SOEA+HEA ink. These comparisons showed the influences of inclusion misalignments and agglomerations as well as limitations of generating staggered nanostructures.

The 3D RVEs had relatively good and acceptable predictions for nano-scale inclusions; while their predictions for micro-scale inclusions were more reliable. In future work, developed 3D FE micromechanical models may be used to predict the onset and evolution of local damage and cracking in different inclusion-reinforced biomimetic composites as well as local nonlinear or time-dependent behavior. Furthermore, these micromechanical models can be an applicable and efficacious tool in designing a variety of new composite material systems and optimizing their microstructures.

Acknowledgements

The writing of this thesis and the work it encompasses could not have been done without the support I received from mentors, friends, and family.

My supervisors, Dr. John Montesano and Dr. Thomas Willett, provided me with their support, responsibility, guidance, patience, and mentorship. In addition to learning from their exceptional knowledge, I am very fortunate to have supervisors who have taught me many life lessons. I am very proud that I have had the honor of working under their supervision.

Dr. Geng Li was excellent colleague, mentor, and friend who helped me during the computational phase of this project.

Dr. Patricia Comeau in the Composite Biomaterials Systems lab was an outstanding mentor who helped in all experiments of this study.

Daniel Dapaah, Raphael Badaoui, and Cullen James Tielemans my colleagues in the composite biomaterials systems lab were excellent friends who helped in the various parts of my experiments.

Dr. Jalil Nourisa, Dr. Pedram Samadian, Dr. Davood Salimi Majd, and Dr. Armin Abedini were outstanding experts who guided me with their practical ideas and discussions.

Finally, I owe special thanks to Mitra Ghaderi, for her unending love, encouragement, and patience over these long two years.

*To anyone who desires and strives to achieve the seemingly unachievable;
my mother is a prominent example.*

Table of Contents

List of Figures	x
List of Tables	xiv
Chapter 1: Introduction	1
1.1. Context and Motivation	1
1.2. Research Objectives	4
1.3. Outline of Thesis	4
Chapter 2: Theoretical Background and Literature Review	5
2.1. Overview of Biological and Natural Composites	5
2.2. Overview of Existing Biomimetic Composites	9
2.3. Overview of Fabrication Techniques	12
2.4. Micromechanics of Heterogeneous Materials	15
2.4.1. Mechanical Response of Heterogeneous Materials	15
2.4.2. Discontinuous Staggered Inclusion Reinforced Composites	21
2.4.3. Periodic Micro-Field	22
2.4.4. Periodic Boundary Conditions	24
2.4.5. Homogenization Theory	29
2.5. Analytical Models for Discontinuous Inclusion-Based Composites	33
2.5.1. Mori–Tanaka Model	34
2.5.2. Modified Shear lag	35
2.5.3. Halpin-Tsai Model	36
2.6. Computational Micromechanical Modeling of Biomimetic Composites	36
Chapter 3: Computational Models Development	39
3.1. Generating Non-uniformly Staggered Periodic Microstructure	39
3.2. 3D Assessment of Generated Staggered Random Dispersions	45
3.3. Modeling in ABAQUS	49
Chapter 4: Materials and Sample Fabrication	53
4.1. Silanization of Nano-hydroxyapatite	53
4.2. Preparation of 3D-printable Nanocomposite Inks	55
4.3. Direct Ink Writing (DIW)	59
4.4. 3D-printed filament Characterizations	64
Chapter 5: Mechanical testing methods	81
5.1. Specimen Preparation for Biopolymer Resin Mechanical Tests	81

- 5.2. Filament Test Specimens Preparation 83
- 5.3. Micro-mechanical and Micro-DIC Measurements..... 84
- Chapter 6: Results 90
- 6.1. Computational Model Verification 90
- 6.2. Experimental Results and Model Predictions 108
 - 6.2.1. Biopolymers testing results..... 109
 - 6.2.2. Nanocomposite filament testing results..... 111
 - 6.2.3. Comparisons of numerical, analytical, and experimental results for 3D-printed nanocomposites..... 121
- Chapter 7: Discussion..... 126
- Chapter 8: Conclusions 132
- 8.1. Conclusions 132
- 8.2. Recommendations for future works..... 134
- References 136

List of Figures

Figure 1. Typical staggered structures discovered in biological and natural materials; (a) mineral tablets in shells; (b) hydroxyapatite nanocrystals in collagen fibrils of bone; (c) tripocollagen molecules in collagen fibrils of tendon [4].	2
Figure 2. (a) Specific strength and stiffness Ashby plots [3] and (b) fracture toughness versus stiffness plot [3] for biological and biomimetic materials and their constituents. (c) Various universal staggered structures observed in natural and biological composites [8].	7
Figure 3. (Structure) Seven levels of bone hierarchy structure from macro-to nano-scale. (Mechanisms) Behind-crack tip and front-crack tip bone toughening mechanisms from macro-to nano-scale [1, 3].	8
Figure 4. The effects of different bio-mimicked hierarchy structures on improving toughening mechanism and crack propagation under the pure mode I loading [9].	9
Figure 5. Different inclusion shapes used in biomimetic composites. (a) aragonite micro-rods [40], (b) hexagonal alumina micro-platelets [41], (c) silicon carbide whiskers and carbon fibers [12].	12
Figure 6. A comparison between biomineralization and 3D printing of a biological and synthetic microstructure respectively [8].	14
Figure 7. Three-dimensional RVE for modeling staggered hexahedral morphologies of discontinuous cylindrical inclusions. The shaded and bolded parts are suitable for symmetry and periodic boundary conditions respectively [45].	22
Figure 8. Variation of strains $\epsilon_s(z)$ and displacements through $u_s(z)$ a typical 1D periodic composite comprise of material A and B with periodic unit of c_z . Small white dots represent the symmetry points of $\epsilon_s(z)$ and $u_s(z)$ [45].	23
Figure 9. A variety of RVEs with different shapes, sizes, and boundary conditions which can be employed to evaluate the mechanical performances of a periodic hexagonal distribution of circular heterogeneous micro-geometry [45].	25
Figure 10. Various equal minimum-size periodic RVEs for a non-uniformly dispersed particles with two non-orthogonal periodic vector pairs include (P_1, P_2) and (P'_1, P_2) [45].	26
Figure 11. Scheme of periodic boundary conditions (PBCs) applied on a rectangular 2D RVE [45].	28
Figure 12. (a) Heterogeneous periodic microstructure of a representative biomimetic composite. (b) a representative volume element (RVE) of composite microstructure with inclusion and matrix.	31
Figure 13. Flowchart of the 3D staggered hard-core algorithm (SHCA).	40
Figure 14. 3D and 2D views of overlap check function for hexagonal inclusions.	42
Figure 15. 3D and 2D views of overlap check function for cylindrical inclusions.	43

Figure 16. Inclusion dimensions used in aspect ratio (ρ) calculation for 3D RVE models. (a) hexagonal platelet, (b) cylindrical inclusion.	43
Figure 17. Created periodic 3D RVEs with randomly distributed (a-c) staggered hexagonal platelets and (e-g) aligned cylindrical inclusions with 30% volume fraction.	45
Figure 18. (a) 3D Autocorrelation analysis and density recovery profile (DRP) for 3D RVEs with hexagonal inclusions for 30% volume fraction. (b) autocorrelation tri-histogram plots.....	47
Figure 19. 3D Autocorrelation analysis and density recovery profile (DRP) for 3D RVEs with cylindrical inclusions for 30% volume fraction. (b) autocorrelation tri-histogram plots.....	48
Figure 20. Identical 3D mesh pattern on corresponding opposing surfaces of the 3D RVE generated in ABAQUS by customized copy mesh module. (a) meshing procedure flowchart (b) typical regions on facing exterior periodic surfaces of the 3D RVE.	50
Figure 21. The shape of hydroxyapatite nano-rods[81].	54
Figure 22. Energy-dispersive X-ray spectroscopy (EDX) results in various regions of Si-nHA powder...	55
Figure 23. Schematic of soybean oil epoxidized acrylate and Ciba Irgacure 819 [86].....	57
Figure 24. Energy-dispersive X-ray spectroscopy (EDX) results in various regions of Si-nHA/SOEA composition ink.....	59
Figure 25. 3D-printing configuration include tube and piston system with taped conical nozzle and UV light pen.....	61
Figure 26. Different nozzle shapes with various materials such as plastic, plastic-metal, and metal.....	62
Figure 27. SEM images for the cross-section of a 3D-printed Si-nHA/SOEA filament (20% Si-nAH volume fraction), while Si-nHA particles did not solve in EtOH.	63
Figure 28. SEM images for the cross-section of a 3D-printed Si-nHA/SOEA filament (20% Si-nAH volume fraction), while Si-nHA particles solved in EtOH.	64
Figure 29. Thermogravimetric analyses (TGA) for both inks and different volume fractions. (a) Si-nHA/SOEA ink and (b) Si-nHA/SOEA+HEA ink.	66
Figure 30. 3D-printed filaments cross-sections of Si-nHA/SOEA and Si-nHA/SOEA+HEA nanocomposite inks for various Si-nHA volume fractions.	68
Figure 31. Three various regions on 3D-printed filament cross-section for SEM imaging.	69
Figure 32. Si-nHA nanoparticle dispersions and alignments of two different magnifications for 3D-printed 7% Si-nHA/SOEA+HEA filament.....	70
Figure 33. Si-nHA nanoparticle dispersions and alignments of two different magnifications for 3D-printed 17% Si-nHA/SOEA+HEA filament.....	71
Figure 34. Si-nHA nanoparticle dispersions and alignments of two different magnifications for 3D-printed 25% Si-nHA/SOEA+HEA filament.....	72

Figure 35. Si-nHA nanoparticle dispersions and alignments of two different magnifications for 3D-printed 27% Si-nHA/SOEA+HEA filament.....	74
Figure 36. Si-nHA nanoparticle dispersions and alignments of two different magnifications for 3D-printed 10% Si-nHA/SOEA filament.....	75
Figure 37. Si-nHA nanoparticle dispersions and alignments of two different magnifications for 3D-printed 20% Si-nHA/SOEA filament.....	77
Figure 38. Si-nHA nanoparticle dispersions and alignments of two different magnifications for 3D-printed 25% Si-nHA/SOEA filament.....	78
Figure 39. Si-nHA nanoparticle dispersions and alignments of two different magnifications for 3D-printed 30% Si-nHA/SOEA filament.....	79
Figure 40. Si-nHA and coated gold particle sizes and contrast in SEM images.....	80
Figure 41. Prepared biopolymeric dog-bone using Teflon mold with one-side microscope glass slide and UV light curing nail box.....	82
Figure 42. Nanocomposite filament test specimen configuration.....	83
Figure 43. Small-scale universal and -2D DIC (microscope) test configuration.....	84
Figure 44. Speckle patterns on biopolymers doge-bone specimens.....	85
Figure 45. Speckle patterns on nanocomposite filament specimens.....	86
Figure 46. Loading profile of biopolymeric dog-bone specimen tests.....	88
Figure 47. Loading profile of 3D-printed nanocomposite filament specimen tests.....	88
Figure 48. Stress contours for hexagonal inclusion RVE model with (a) uniaxial applied load along 3-direction, (b) pure shear applied in 23-plane.....	92
Figure 49. Stress contours for cylindrical inclusion RVE model with (a) uniaxial applied load along 1-direction, (b) pure shear applied in 23-plane.....	93
Figure 50. Comparisons of Young's modulus versus volume fraction for different aspect ratios among established analytical models (i.e., Mori-Tanaka, modified shear lag, and Halpin-Tsai) and 3D RVE results (a) E_2 for hexagonal platelet and (b) E_1 for cylindrical inclusions model.....	98
Figure 51. Comparison of normalized Young's modulus (E / E_m , where E_m is the Young's modulus of the matrix) versus volume fraction between 2D RVE and both 3D RVE models (i.e., hexagon platelet in-plane (E_2 or E_3) and cylindrical inclusion in the longitudinal direction (E_1)).....	99
Figure 52. Computed orthotropic elastic constants for hexagonal platelet model versus volume fraction (φ_i) for various aspect ratios. (a) E_2, E_3 , (b) E_1 , (c) G_{12}, G_{13} , (d) G_{23} , and (g) ν_{12}, ν_{13} , and ν_{23}	102
Figure 53. Computed orthotropic elastic constants for cylindrical inclusion model versus volume fraction (φ_i) for various aspect ratios (a) E_2, E_3 , (b) E_1 , (c) G_{12}, G_{13}, G_{23} , (d) ν_{12}, ν_{13} , and ν_{23}	104

Figure 54. Computed orthotropic elastic constants for cylindrical and hexagonal inclusion models versus two aspect ratios ($\rho = 5$ and 15) for 10% volume fraction by altering dimensions of inclusion in two different cases (i.e., changing by only increasing L or h). (a) E_1 , (b) E_2 , (c) , (d) G_{12} , (e) G_{13} , (f) G_{23} , (g) ν_{12} , (h) ν_{13} and ν_{23}	108
Figure 55. The effects of UV light dose on the tensile strength of both biopolymers (i.e., SOEA and SOEA+HEA).	109
Figure 56. Stress-strain curves for both biopolymeric dog-bone specimens (i.e., SOEA+HEA and SOEA).	110
Figure 57. Stress-strain curves for 3D-printed Si-nHA/SOEA+HEA nanocomposite filaments with different Si-nHA volume fractions.	112
Figure 58. Stress-strain curves for 3D-printed Si-nHA/SOEA nanocomposite filaments with different Si-nHA volume fractions.....	114
Figure 59. Stress-strain comparisons among both biopolymeric matrices and 3D-printed nanocomposite inks in different Si-nHA volume fractions.....	119
Figure 60. Normalized stress-strain comparisons among both biopolymeric matrices and 3D-printed nanocomposite inks for different Si-nHA volume fractions.	120
Figure 61. Comparisons of Young's modulus versus various inclusion volume fractions among experimental, 3D RVE, and Mori-Tanaka results. (a) Si-nHA/SOEA+HEA nanocomposite (b) Si-nHA/SOEA nanocomposite.	122
Figure 62. Comparisons of normalized Young's modulus versus various inclusion volume fractions among experimental, 3D RVE, and Mori-Tanaka results. (a) Si-nHA/SOEA+HEA nanocomposite (b) Si-nHA/SOEA nanocomposite.	123
Figure 63. Computed orthotropic elastic constants using 3D RVE for both 3D-printed nanocomposites versus volume fraction. (a) E_2 and E_3 for Si-nHA/SOEA ink; (b) E_2 and E_3 for Si-nHA/SOEA+HEA ink; (c) G_{12} , G_{13} , and G_{23} for Si-nHA/SOEA ink; (d) G_{12} , G_{13} , and G_{23} for Si-nHA/SOEA+HEA ink; (e) ν_{12} , ν_{23} , and ν_{13} for Si-nHA/SOEA ink; (f) ν_{12} , ν_{23} , and ν_{13} for Si-nHA/SOEA+HEA ink.....	125
Figure 64. SEM image of a 3D-printed textured cellular microstructure using 20 wt% acetylated cellulose nanocrystal cylindrical shape nanoparticles [102].	127

List of Tables

Table 1. Various types of materials symmetry, anisotropy, transformation and of elastic tensors [42-45].	17
Table 2. Eshelby’s tensor element for elliptical inclusions.....	34
Table 3. Different elastic properties used in both 3D RVEs for different purposes.	51
Table 5. All tested biopolymeric dog-bone specimens and nanocomposite filaments.	87
Table 6. Comparison between normalized moduli (E_2/E_m), E_1 , and G_{12} from 3D RVEs (5 trials), analytical models, and experimental data of a nacre-mimetic material (i.e., alumina/chitosan) with a volume fraction (φ_i) of 10%. Error is calculated against the experimental data.....	95
Table 7. Comparison between normalized moduli (E_1/E_m) from 3D RVEs (5 trials), analytical models and experimental data from a short carbon fiber/polypropylene composite having a volume fraction (φ_i) of 10%.	96
Table 8. Young’s modulus, Poisson’s ratio, and tensile strength of SOEA+HEA for five different tested dog-bone specimens.....	110
Table 9. Young’s modulus, Poisson’s ratio, and tensile strength of SOEA for five different tested dog-bone specimens.....	111
Table 10. Young’s modulus and tensile strength of 3D-printed 7%Si-nHA/SOEA+HEA five different filaments with two different nozzle sizes.....	115
Table 11. Young’s modulus and tensile strength of 3D-printed 17%Si-nHA/SOEA+HEA five different filaments with two different nozzle sizes.....	115
Table 12. Young’s modulus and tensile of 3D-printed 25%Si-nHA/SOEA+HEA five different filaments with two different nozzle sizes.....	115
Table 13. Young’s modulus and tensile strength of 3D-printed 27%Si-nHA/SOEA+HEA five different filaments with two different nozzle sizes.....	116
Table 14. Young’s modulus and tensile strength of 3D-printed 10%Si-nHA/SOEA five different filaments with two different nozzle sizes.....	116
Table 15. Young’s modulus and tensile strength of 3D-printed 20%Si-nHA/SOEA five different filaments with two different nozzle sizes.....	117
Table 16. Young’s modulus and tensile strength of 3D-printed 25%Si-nHA/SOEA five different filaments with two different nozzle sizes.....	117
Table 17. Young’s modulus and tensile strength of 3D-printed 30%Si-nHA/SOEA five different filaments with two different nozzle sizes.....	118

Chapter 1: Introduction

1.1. Context and Motivation

In the initial stages of technological development of humanity, a number of industries and technologies were built by the aid of biological and natural materials namely wood, shells, leather, and bone. Over the years, these material systems were gradually substituted by their synthetic counterparts which offered improved performance. Researchers continue to show interest in the sophisticated microstructures and unique characteristics of natural and biological composite materials, including high specific mechanical properties when compared to that of the constituents. Cutting-edge laboratory facilities and modeling tools currently provide the chance of deciphering the complicated interactions of mechanisms from atomic to macroscopic scale by which natural and biological structures enrich the distinctive mechanical properties. Today, there are many demands for low-density material systems which can address higher efficient technologies for a variety of strategic fields including medicine, transportation, and construction among others. In order to overcome this challenge, developing material systems which would offer simultaneous combinations of stiffness, strength, and toughness in a lightweight structure would require to be fabricated in practical-scale bulk geometries, high volume, and inexpensive cost. Recently, this achievement is a fashion goal among a number of research groups. Although several biomimetic materials have generated in laboratory scale, there is a considerable doubt concerning their capabilities to be scaled-up for diverse practical engineering applications.

Human-engineered materials have been generated by the aid of synthetic compositions in an uncomplicated micro-scale structure. It has been ascertained that by manipulation of material nanostructures which previously were unattainable, a broad range of opportunities can be opened

to newly develop material systems. However, there is still the extensive number of limitations in regard to having control of the nano-scale characteristic of materials during fabrication. Any intelligent approach must include nano-, micro-, and macro-scale characteristics. For the purpose of accomplishing this, the critical design features of natural and biological structures, namely their design motifs must be extracted and translated to the other material systems. Nevertheless, it must be considered that current advanced engineering requires that any biomimetic process should be scaled-up for practical fabrication in order to speed up manufacturing as well as decrease the designing and executing time [3].

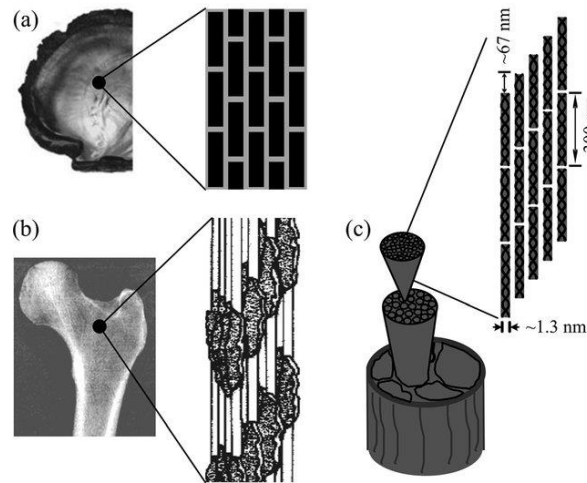


Figure 1. Typical staggered structures discovered in biological and natural materials; (a) mineral tablets in shells; (b) hydroxyapatite nanocrystals in collagen fibrils of bone; (c) tripocollagen molecules in collagen fibrils of tendon [4].

One exciting potential application of biomimetic composite materials is bone reconstruction. Indeed, various factors including chemical composition, nano/microstructure, and hierarchy architecture can be inspired from bone itself. Bone is composed of ~45 vol% stiff hydroxyapatite nanocrystals embedded in ~55 vol% compliant collagen fibrils and proteins arranged in sophisticated hierarchical architectures in different length scales. In effect, similar to other natural

or biological composites, bone is formed by the staggered hierarchy structure from nano- to macro scale (see Figure 1). In order to generate a bone-mimic (or bone-inspired) material, a composite material is required which is comprised of nano-scale inclusions and compliant matrix with chemical and physical bonding between inclusions and matrix.

There are a small number of studies conducted on these biomimetic composite materials due to the limitations of manufacturing nano-scale hierarchy architectures. In order to generate bone-like nanostructure, the fabrication process must be able to have control on the arrangement of nano-scale inclusion orientations and the many layers of structure at larger length scales. Furthermore, high nano-scale inclusion volume fraction, as well as in-vivo challenges namely biocompatibility and cytocompatibility which are related to the matrix of these materials systems, are other obstacles. Characterization of such bone-mimetic and other biomimetic composites with different inclusion shapes and sizes as well as complex structural arrangements and the establishment of general design guidelines is pivotal for widespread adoption of these materials. To facilitate this, it is essential to develop robust high-fidelity design and fabrication tools to assess the performance of these biomimetic composites.

By using reliable computational tools such as micromechanical models, different mechanical tests can be virtually performed for various material systems, and thus mechanical performances can be assessed prior to experimental implementations and tests. Accordingly, the influences of inclusion and matrix properties, as well as, inclusion shape, size, volume fraction and dispersion on the mechanical responses of material can be virtually investigated.

1.2. Research Objectives

The main objectives of this research are summarized as follows:

- (iv) Develop a computational tool for assessing the elastic responses of biomimetic composites using 3D finite element micromechanical modeling.
- (v) Make a 3D-printable nanocomposite ink comprised of a plant oil-based polymer and nanoparticles for bone-mimetic applications.
- (vi) 3D printing nanocomposite filaments having staggered nanostructures and testing in order to validate 3D micromechanical models using mechanical properties.

1.3. Outline of Thesis

In Chapter 2, theoretical background and literature review of mechanical responses and fabrication methods of biological and biomimetic inhomogeneous materials are described to understand the required knowledge, and realize limitations, gaps, and shortcoming of in this area. In Chapter 3, the development of novel, computational 3D finite element micromechanical models are described. In Chapter 4, the methods used to generate biomimetic nanocomposite filaments, such as ink preparation, extrusion-based 3D-printing process, and various material characterization tests, are described. In Chapter 5, the preparation of mechanical test specimens and their tensile tests are described. In Chapter 6, results from the computational and experimental studies are presented and compared. In Chapter 7, the findings of this project are discussed in the context of the literature. Finally, in Chapter 8, conclusions and recommendations are presented.

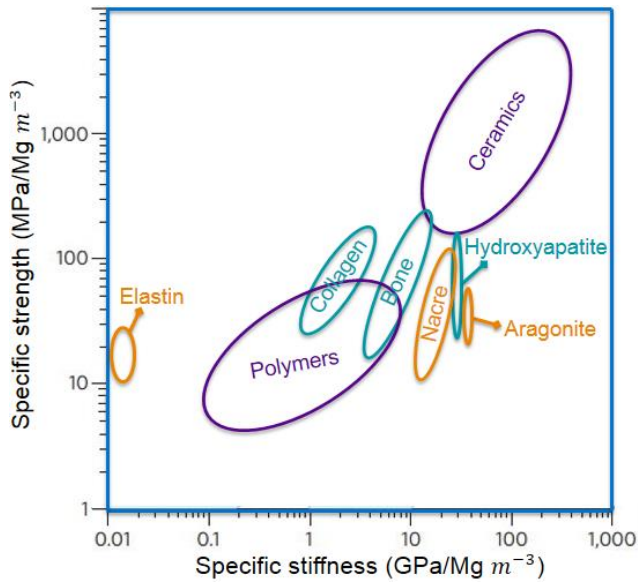
Chapter 2: Theoretical Background and Literature Review

In this chapter, the characteristic high performance of biological and natural composites are reviewed. Afterward, biomimetic materials that have been produced in seeking to achieve the same performance of biological and natural materials are reviewed. Thereafter, various fabrication techniques that have been used to manufacture biomimetic materials are introduced. In addition, micromechanical modeling aspects of heterogeneous materials, including discontinuous staggered structure, periodic micro-fields, periodic boundary conditions (PBCs), and homogenization theory are explained. Well-established analytical models for discontinuous microstructures are also described. Finally, micromechanical modeling, and associated algorithms, employed for biomimetic materials are reviewed. All these contents are required to understand and implement various steps of this project.

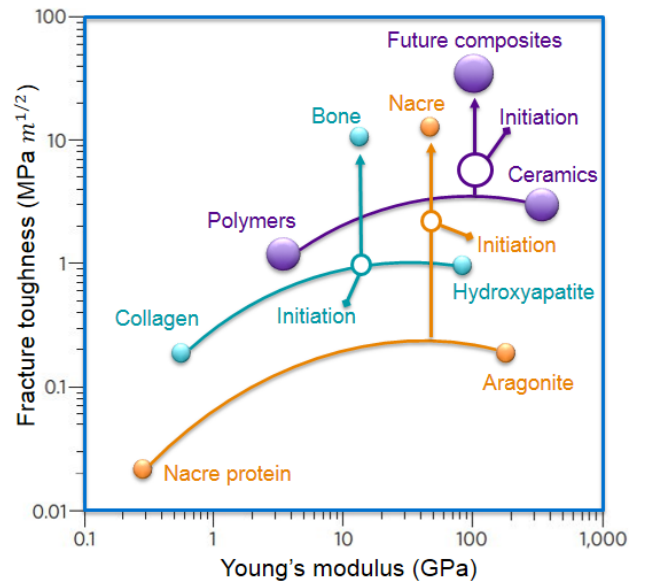
2.1. Overview of Biological and Natural Composites

Various biological materials, including bone, tooth enamel, mollusk shells, mantis shrimps, have been naturally optimized over millions of years and, presumably as a result, exhibit high mechanical performance. These biological composites benefit from simultaneous low density, high specific toughness, specific stiffness, and specific strength, which are unmatched in comparison to traditional engineering materials [1, 3, 5, 7]. Figures 2 (a-b) illustrate high strength versus high stiffness, and high fracture toughness versus high Young's modulus of two high-performance biological composites, namely bone and nacre. The key features or motifs that are pervasive among the materials mentioned above are overlapping stiff inclusions embedded in a compliant matrix having complex staggered architectures (Figure 2 (c)) [8].

The staggered microstructure is the main archetype by which many biomimetic composite materials are developed. Figure 2 (a-b) also, demonstrate that by means of biomimicking and using synthetic constitutes, various high-performance composite material systems can be generated for different engineering applications, such as biomedical implants, synthetic bone grafts, and many others [3, 8].



(a)



(b)

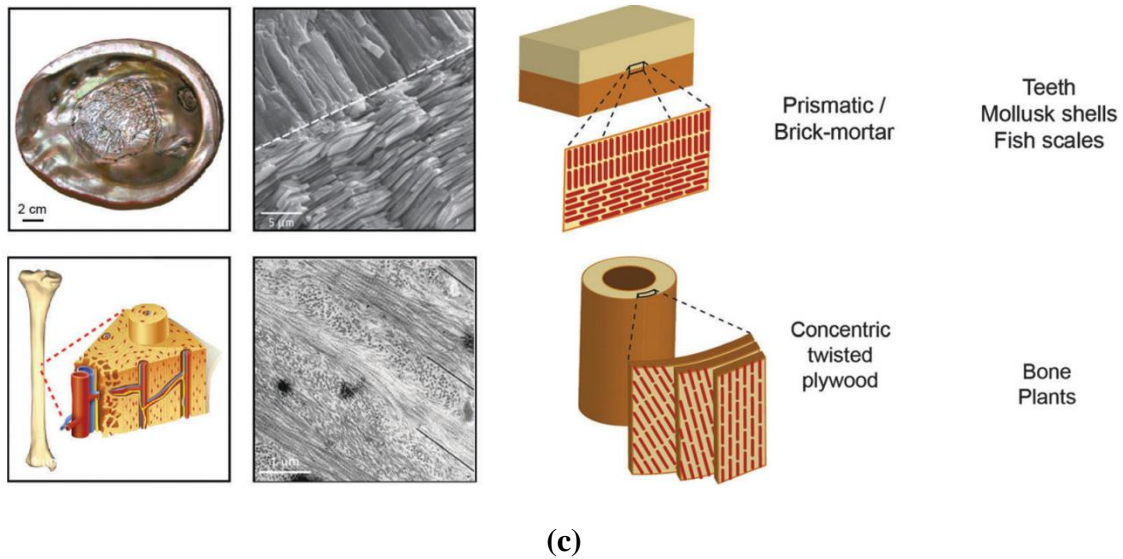


Figure 2. (a) Specific strength and stiffness Ashby plots [3] and (b) fracture toughness versus stiffness plot [3] for biological and biomimetic materials and their constituents. (c) Various universal staggered structures observed in natural and biological composites [8].

A number of biological composites, such as bone and nacre, demonstrate higher fracture toughness than their constituents (i.e., inclusions and matrix). They are able to sustain the onset of fracture and crack propagation using extensive intrinsic and extrinsic toughening mechanisms, such as collagen-fibril and un-cracked-ligament bridging in bone (see Figure 3), as well as, viscoelastic organic layer and inelastic shear resistance of nano-asperities in nacre. These phenomena increase crack propagation resistance (post crack growth initiation) significantly. Indeed, fabricating biomimetic composites is a challenging process when trying to mimic the interlocking mechanisms in their hierarchical architecture structure and high inclusion volume fractions (see Figure 3 and 4) [1, 3].

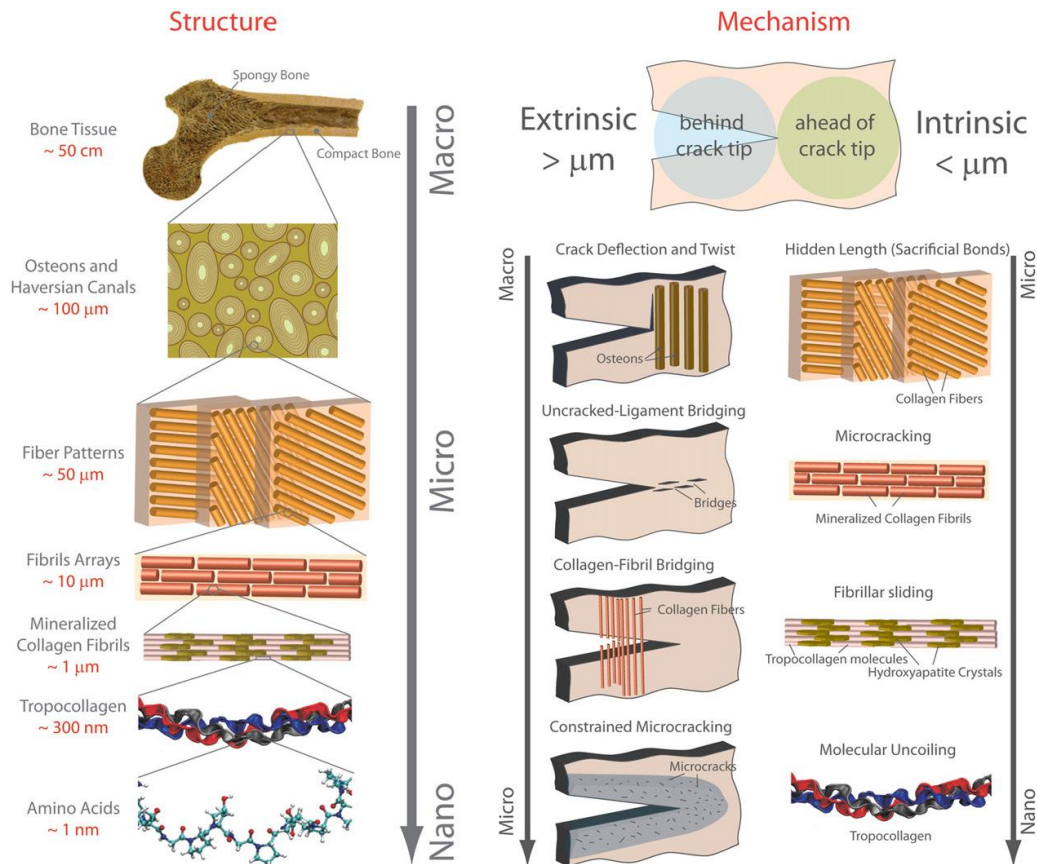


Figure 3. (Structure) Seven levels of bone hierarchy structure from macro-to nano-scale.

(Mechanisms) Behind-crack tip and front-crack tip bone toughening mechanisms from macro-to nano-scale [1, 3].

Presumable, by mimicking the staggered hierarchical structures found in bone and nacre in a synthetic biomimetic composite, similar mechanical performance can be attained [1, 8]. For instance, Figure 4 illustrates the considerable effects of various mimicked hierarchy structures on the toughening mechanism and crack trajectory subjected to the pure mode I (opening) [9]. Consequently, by inspiration and bio-mimicry, the aforementioned high-performance characteristics of biological and natural composites can be achieved and implemented for several different engineering applications.

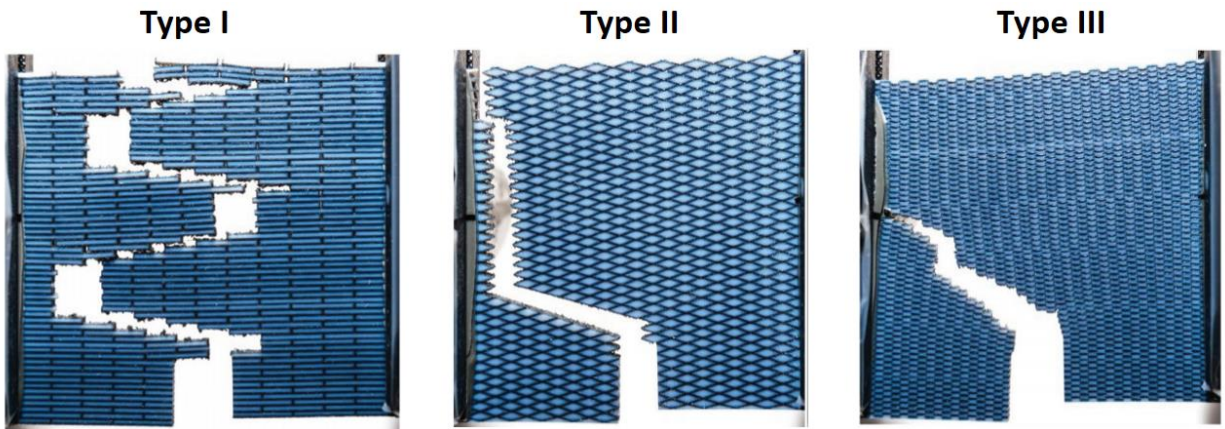


Figure 4. The effects of different bio-mimicked hierarchy structures on improving toughening mechanism and crack propagation under the pure mode I loading [9].

2.2. Overview of Existing Biomimetic Composites

Various research groups have been motivated to develop and fabricate synthetic bone- and nacre-like composites in order to investigate the structure-property relationship [1, 8]. Dimas et al. [9] generated bone-like composites to mimic the behavior of various staggered structures in bone- and nacre-like materials. Grossman et al. [10] fabricated a nacre-mimetic composite using alumina micro-platelets. Not only they achieved a simultaneous stiffness and toughness, but also the high fracture toughness due to the fracture mechanisms in this material system was attained. Le Ferrand et al. [11] manufactured a biomimetic tooth-shaped composite containing a bilayer microstructure for locally tuning composition and alumina micro-platelet orientation. Compton and Lewis [12] produced various geometries of cellular architectures which were reinforced via rod-shaped whiskers. They notably tailored the stiffness and strength of these material systems. Martin et al. [13] fabricated a biomimetic composite which its elastic properties were locally tuned to exhibit the role of reinforcement architectures in driving crack propagation trajectory. Also, they

remarkably increased the stiffness, Vickers hardness, and failure strain. Erb et al. [14] generated a biomimetic composite with bilayer microstructure of micro-rods inspired from pinecone using gelatin reinforced by ultra-high magnetic response tablets to create different controllable self-shape behavior before and after swelling. Bargardi et al. [15] implemented a bilayer microstructure of micro-platelets on ceramic composites to make programmable self-shape behavior through sintering. Feilden et al. [16] fabricated bone-mimetic ceramic filament composites using micro-platelets inclusions. Gurbuz Guner and Dericioglu [17] manufactured a nacre-mimetic glass/epoxy composite with the staggered structure of glass micro-platelets. Yaraghi et al. [18] generated helicoid and herringbone microstructure inspired from the dactyl segment of mantis shrimp in order to tailor the impact resistance. They found that critical shear strains can occur in helicoid architecture compared with herringbone one. Thus, herringbone architecture benefits from better impact resistance. Zaheri et al. [19] mimicked a helicoidal bio-composite using discontinuous fibers inspired from a particular beetle. They investigated the effects of pitch or twist angle on various mechanical responses such as stress-strain, crack initiation, stiffness degradation, strain heterogeneities, and fracture propagation and surface. Gu et al. [20] fabricated a biomimetic conch shell architecture to tune the impact performance and crack arresting mechanism. They tailored the impact resistance of this material system up to 70% by hierarchy and adding a second layer. Guiducci et al. [21] created a periodic honeycomb structure inspired by plants to achieve different behavior before and after swelling. In order to mimic the behavior of shark skin, Wen et al. [22] generated stiff denticles on the flexible layer. Araya et al. [23] produced a segmentary armor jacket inspired from fish skin. Mirkhalaf et al. [24] overcame glass brittleness by inspiring from micro-architectures. They locally tuned glass using jigsaw-like interfaces, thus, the crack initiation and propagation resistance of glass significantly amplified. Yin et al. [25] generated biomimetic

simultaneous tough and deformable glass inspired from cross-ply architectures. They increased initial stiffness, tensile strength, deformation failure, energy absorption, and fracture energy of glass simultaneously. Mirkhalaf et al. [26] mimicked various topological interlocked structure to boost simultaneous strength and toughness. They have tested the maximum load capacity and energy absorption of each topological interlocked structure under static and impact loading. They showed that octahedron and tetrahedron interlocking topology has maximum load and energy absorption.

There are some notable shortcomings in the performance of the abovementioned biomimetic materials resulting from the material and manufacturing processes. Some of the limitations include (i) micro-scale inclusions were employed in these materials; while to achieve the high performances properties of natural and biological materials, nano-scale hierarchy architectures are required. (ii) In most manufacturing processes, the orientation and alignment of nano-scale inclusions cannot be controlled and steered. (iii) The inclusion volume fraction in these materials is much lower than many natural and biological composites. (iv) Nano-scale physical and chemical bonding namely interlocking and bridging have not yet been developed in these materials.

To design and fabricate bone-mimetic composite materials, a wide range of polymers have been reinforced via different micro-particles using a variety of fabrication techniques [1, 3, 8, 35]. However, several shortcomings make these materials inferior in comparison with bone. For instance, the level of stiffness, toughness, and strength has not been amplified significantly. Other important limitations for generated bone-like composites are that most matrix phase of these materials are fabricated by the molten, non-biocompatible, or non-biodegradable polymers, and they reinforced using microscale particles; while bone possesses nano-hydroxyapatite (nHA) crystals. Furthermore, achieving ~45 vol% mineral particles for some of these techniques is

impossible. Also, the bone-like staggered structure of inclusions could not be executed; while particles dispersion and clustering is another obstacle. Moreover, in some of them, the interface between nHA crystals with matrix was not appropriately enhanced. A number of these methods are challenging, expensive, and time-consuming.

2.3. Overview of Fabrication Techniques

A number of inclusion types, including hexagonal (i.e., flake-like) platelet and rod shape (i.e., cylindrical), have been utilized to generate biomimetic composites (see Figure 5) employing a variety of fabrication techniques. Examples of these techniques include sputtering [27], centrifuging and casting [28], layer-by-layer assembly [29], freeze casting [30], [31], sedimentation [32], vacuum filtration process [33], solution casting [34], doctor blading [35], ink-jet printing [36], gel casting [37], hot pressing [38], laser engraving [24], magnetic alignment [39], magnetically assisted slip casting [11], hot-press assisted slip casting [17], and robocasting [16].

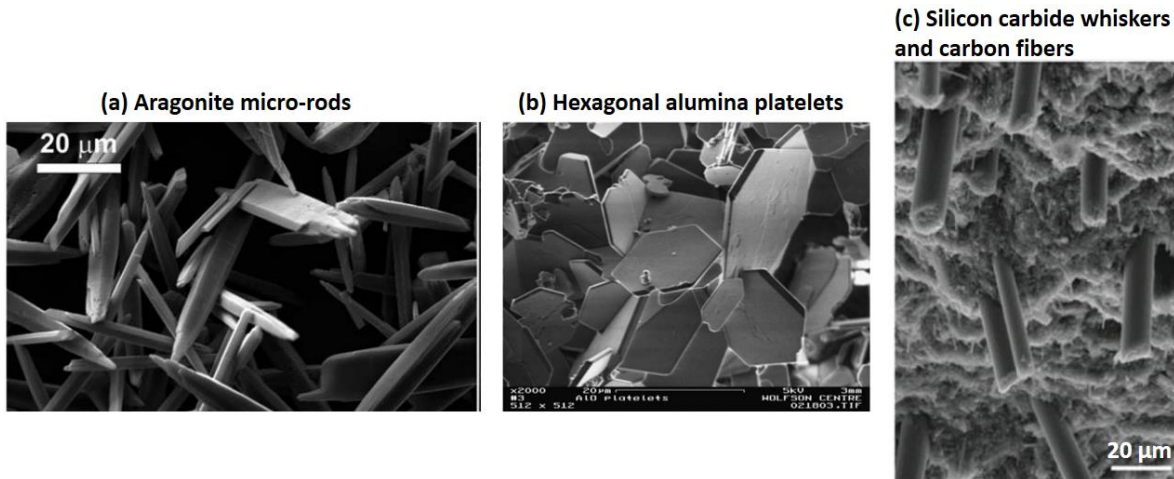


Figure 5. Different inclusion shapes used in biomimetic composites. (a) aragonite micro-rods [40], (b) hexagonal alumina micro-platelets [41], (c) silicon carbide whiskers and carbon fibers [12].

During the past decades, additive manufacturing (AM) particularly 3D-printing has revolutionized rapid prototyping fields by generating high-detailed intricate geometries which were impossible employing traditional processing routes. Using the capabilities of AM biomimetic composites with complex microstructures and locally graded chemical compositions can be generated; while these were not possible using conventional techniques [8]. The discovery of this feature has been inspired and exploited based on the sophisticated hierarchical architectures found in biological and natural composite materials created via living organisms. In effect, the microstructural features of natural and biological composite materials can be reproduced with synthetic components using AM. By employing AM potentials, the local microstructures and chemical compositions can be controlled in the layer by layer form. This layer-by-layer method in AM can make similar feature with the process of living organisms generate biological and natural composite materials (see Figure 6). Figure 6 (a) illustrates the biomineralization process in which mineral phases are generated within the organic structure using selected inorganic matters in cells. On the other side, 3D printing can continuously produce a layer-by-layer or droplet structure in the filament form. Both these two processes are layer-by-layer additive technique in two different manufacturing methods. These similar features include: (i) supplying structure continuously and step by step, (ii) a programmed code by which the local scheme of microstructure can be assembled, (iii) various mechanisms which can execute the code and hence, govern the orientation and chemical compositions of generated microstructure, and (iv) a stabilization step whereby the generated microstructure is configured to a heterogeneous layer.

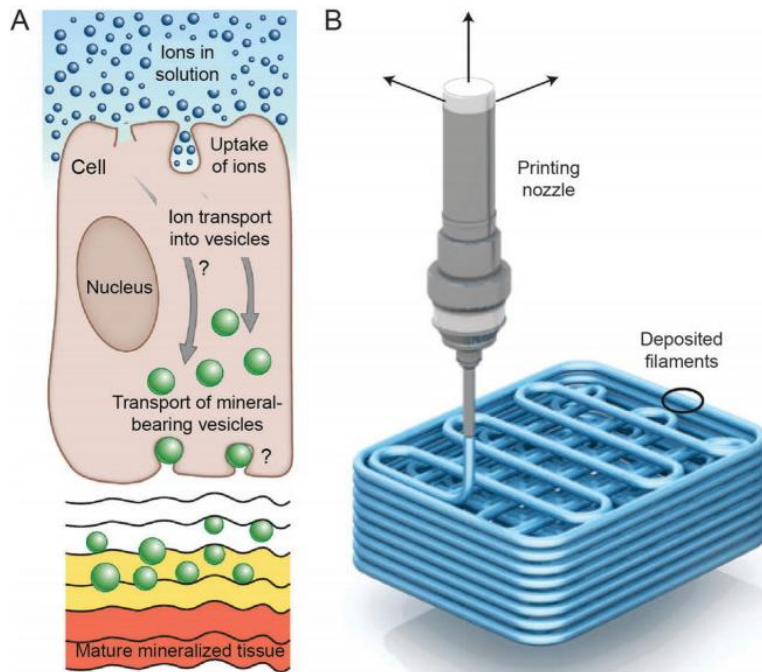


Figure 6. A comparison between biomineralization and 3D printing of a biological and synthetic microstructure respectively [8].

Although by employing existed manufacturing technologies the complexities and functionalities of biological composite material systems cannot be reached, the similar highlighted features propose that AM can be an interesting route to generate synthetic inhomogenous material systems and boost material characteristics up to natural and biological composites materials. Consequently, 3D printing applicability and capabilities are employed by means of different AM techniques across a broad range of biomimetic composites for various engineering applications. Examples of these techniques include: PolyJet 3D printing, direct ink writing (DIW), 3D magnetic printing, multi-material magnetically-assisted 3D printing (MM-3D printing), Magnetically-assisted slip casting [8].

2.4. Micromechanics of Heterogeneous Materials

In this sub-section, mechanical characteristics of heterogeneous materials and their different types of anisotropy are reviewed. Afterward, some micromechanical approaches for discontinuous staggered composites are described. In regard to micromechanical modeling, periodic boundary conditions and homogenization theory also are briefly explained.

2.4.1. Mechanical Response of Heterogeneous Materials

A number of engineering and biological materials are heterogeneous. They comprise of distinct phases which are discernible at different length scales. Each phase may exhibit distinct properties and orientation. Well-known examples of these materials include biomimetic materials which were described in Section 2.2 and also different industrial composites, porous and cellular materials, polycrystalline materials, functionally graded materials among others. The performances of heterogeneous materials are characterized via the materials property, geometry, and topology of phases. The responses of heterogeneous materials can be assessed at a range of length scales from sub-atomic to continuum level. In this study, the micro-level of heterogeneous materials is investigated. The overall properties of multi-phase materials can be determined using a micromechanical model and homogenization by considering the properties of constituents, interfaces, topology, and morphology [42-45].

One of the significant features in continuum micromechanics is the heterogeneity level of constituents. This parameter is often defined via the phase contrast. For instance, the elastic contrast of a matrix-inclusion composite is defined as

$$C = \frac{E_i}{E_m}, \quad (1)$$

where E_i and E_m denote the Young's moduli of inclusion and matrix respectively.

Heterogeneous materials may exhibit various anisotropy behaviors. Indeed, anisotropy is the directional dependency of material characteristics and responses. Based on symmetries in the internal structure, various types of anisotropy can be specified. The elastic tensor arrangements tend to be more straightforward when the internal symmetries in the material increase [42-45]. Each type of symmetry can change stiffness tensor by rotation and reflection through a particular axes and plane to retain the symmetry transformations which can be presented in the following:

$$Q = Q_{ij} e_i \otimes e_j \quad (2)$$

where Q is the orthogonal second order tensor as well as e_i and e_j are unit vectors. Also,

$Q^{-1} = Q^T$ and:

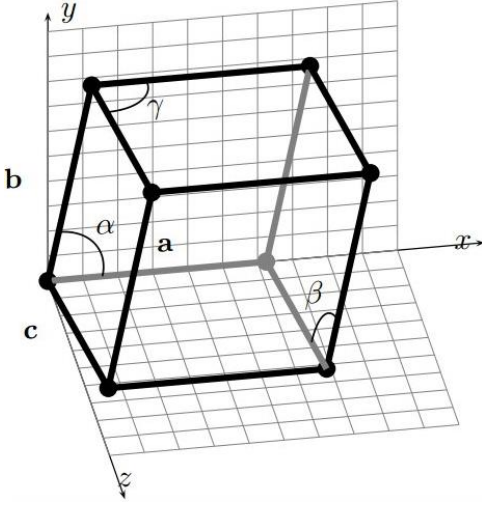
$$\det(Q_{ij}) = \begin{cases} +1 & \text{rotation} \\ -1 & \text{reflection} \end{cases},$$

The elastic tensor (C) is transformed using the following equation:

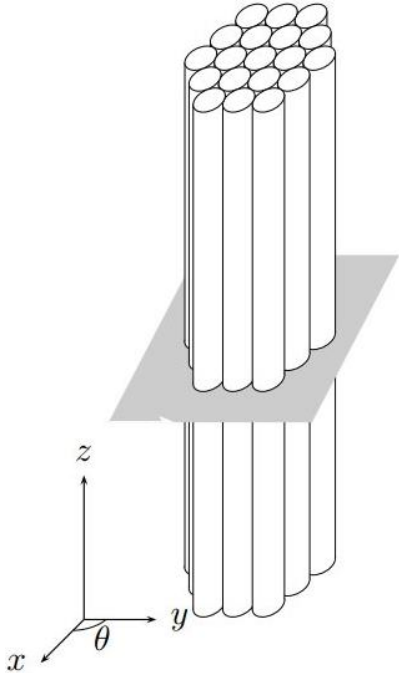
$$C_{ijkl} = Q_{ip} Q_{jq} Q_{kr} Q_{ls} C_{pqrs} \quad (3)$$

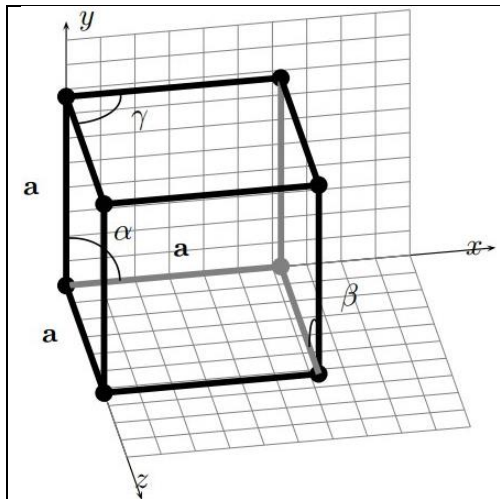
Herein, different types of material symmetry, implications on anisotropy, their symmetry transformations and elastic tensor are briefly described in Table 1. In this project, orthotropic symmetry is employed.

Table 1. Various types of materials symmetry, anisotropy, transformation and of elastic tensors [42-45].

<p>Triclinic</p> 	Without any symmetry planes, and completely anisotropic
	$\alpha, \beta, \gamma < 90$
	Number of independent coefficients: 21
	Symmetry transformation: None
	$C = \begin{bmatrix} C_{1111} & C_{1122} & C_{1133} & C_{1123} & C_{1113} & C_{1112} \\ & C_{2222} & C_{2233} & C_{2223} & C_{2213} & C_{2212} \\ & & C_{3333} & C_{3323} & C_{3313} & C_{3312} \\ & & & C_{2323} & C_{2313} & C_{2312} \\ & & & & C_{1313} & C_{1312} \\ & & & & & C_{1212} \end{bmatrix}$
<p>Monoclinic</p>	Symmetry in xy-plane
	$a \neq b \neq c, \alpha = \beta = \gamma = 90, \alpha < 90$
	Number of independent coefficients: 13
	Symmetry transformation: z-axis reflection
	$Q = \begin{bmatrix} 1 & 0 & 0 \\ 0 & 1 & 0 \\ 0 & 0 & -1 \end{bmatrix}$

	$C = \begin{bmatrix} C_{1111} & C_{1122} & C_{1133} & 0 & 0 & C_{1112} \\ & C_{2222} & C_{2233} & 0 & 0 & C_{2212} \\ & & C_{3333} & 0 & 0 & C_{3312} \\ & & & C_{2323} & C_{2313} & 0 \\ & & & & C_{1313} & 0 \\ & & & & & C_{1212} \end{bmatrix}$
<p style="text-align: center;">Orthotropic</p>	<p style="text-align: center;">Reflection symmetry in xy- xz- and yz-plane</p> <p style="text-align: center;">$a \neq b \neq c, \alpha = \beta = \gamma = 90$</p> <p style="text-align: center;">Number of independent coefficients: 9</p> <p style="text-align: center;">Symmetry transformation: x-axis, y-axis, and z-axis reflection</p> $Q = \begin{bmatrix} -1 & 0 & 0 \\ 0 & 1 & 0 \\ 0 & 0 & 1 \end{bmatrix}, Q = \begin{bmatrix} 1 & 0 & 0 \\ 0 & -1 & 0 \\ 0 & 0 & 1 \end{bmatrix},$ $Q = \begin{bmatrix} 1 & 0 & 0 \\ 0 & 1 & 0 \\ 0 & 0 & -1 \end{bmatrix}$ $C = \begin{bmatrix} C_{1111} & C_{1122} & C_{1133} & 0 & 0 & 0 \\ & C_{2222} & C_{2233} & 0 & 0 & 0 \\ & & C_{3333} & 0 & 0 & 0 \\ & & & C_{2323} & 0 & 0 \\ & & & & C_{1313} & 0 \\ & & & & & C_{1212} \end{bmatrix}$

<p>Transversely isotropic</p> 	<p>Symmetric in axis which is normal to isotropy plane</p>
	<p>Reflection symmetry in xy- xz- and yz-plane, and z-axis axial symmetry</p>
	<p>Number of independent coefficients: 5</p>
	<p>Symmetry transformation: x-axis, y-axis, and z-axis reflection and all z-axis rotations</p> $Q = \begin{bmatrix} -1 & 0 & 0 \\ 0 & 1 & 0 \\ 0 & 0 & 1 \end{bmatrix}, Q = \begin{bmatrix} 1 & 0 & 0 \\ 0 & -1 & 0 \\ 0 & 0 & 1 \end{bmatrix},$ $Q = \begin{bmatrix} 1 & 0 & 0 \\ 0 & 1 & 0 \\ 0 & 0 & -1 \end{bmatrix},$ $Q = \begin{bmatrix} \cos \theta & \sin \theta & 0 \\ -\sin \theta & \cos \theta & 0 \\ 0 & 0 & -1 \end{bmatrix}, 0 \leq \theta \leq 2\pi$
	$C = \begin{bmatrix} C_{1111} & C_{1122} & C_{1133} & 0 & 0 & 0 \\ & C_{1111} & C_{1133} & 0 & 0 & 0 \\ & & C_{3333} & 0 & 0 & 0 \\ & & & C_{2323} & 0 & 0 \\ & & & & C_{2323} & 0 \\ & & & & & \frac{1}{2}(C_{1111} - C_{1122}) \end{bmatrix}$
<p>Cubic</p>	<p>Reflection symmetry and 90° rotation in xy- xz- and yz-plane</p>



$$a = b = c, \alpha = \beta = \gamma = 90$$

Number of independent coefficients: 3

Symmetry transformation: x-axis, y-axis, and z-axis

reflection and 90° rotations

$$Q = \begin{bmatrix} -1 & 0 & 0 \\ 0 & 1 & 0 \\ 0 & 0 & 1 \end{bmatrix}, Q = \begin{bmatrix} 1 & 0 & 0 \\ 0 & -1 & 0 \\ 0 & 0 & 1 \end{bmatrix},$$

$$Q = \begin{bmatrix} 1 & 0 & 0 \\ 0 & 1 & 0 \\ 0 & 0 & -1 \end{bmatrix}, Q = \begin{bmatrix} 0 & 1 & 0 \\ -1 & 0 & 0 \\ 0 & 0 & 1 \end{bmatrix},$$

$$Q = \begin{bmatrix} 0 & 0 & 1 \\ 0 & 1 & 0 \\ -1 & 0 & 0 \end{bmatrix}, Q = \begin{bmatrix} 1 & 0 & 0 \\ 0 & 0 & 1 \\ 0 & -1 & 0 \end{bmatrix}$$

$$C = \begin{bmatrix} C_{1111} & C_{1122} & C_{1122} & 0 & 0 & 0 \\ & C_{1111} & C_{1122} & 0 & 0 & 0 \\ & & C_{1111} & 0 & 0 & 0 \\ & & & C_{1212} & 0 & 0 \\ & & & & C_{1212} & 0 \\ & & & & & C_{1212} \end{bmatrix}$$

2.4.2. Discontinuous Staggered Inclusion Reinforced Composites

A variety of engineering materials have discontinuous inclusion structures namely discontinuous short-fiber composites. As mentioned in previous sections, a number of natural and biomimetic composite materials also benefit from discontinuous inclusions with different shapes including hexagonal platelets and cylindrical particles. Due to the complex microstructures of discontinuous inclusion reinforced composites, notable efforts have been made to accurately represent the inclusion architecture for subsequent analytical or computational performance assessment. The morphologies of discontinuously reinforced composites are basically three-dimensional. The three-dimensional periodic staggered or aligned hexahedral was employed as a simplest representative volume element (RVE) for discontinuously reinforced composites. This geometry is computationally inexpensive and relatively easy to create (see Figure 7). However, it can have several limitations in regard to inclusion morphologies and loading and boundary conditions [42-45]. By employing larger RVE with realistic inclusion dispersion, periodic boundary conditions (PBCs) can be supported and the full mechanical responses of staggered cylindrical and hexagonal inclusion arrangements can be assessed [42-45].

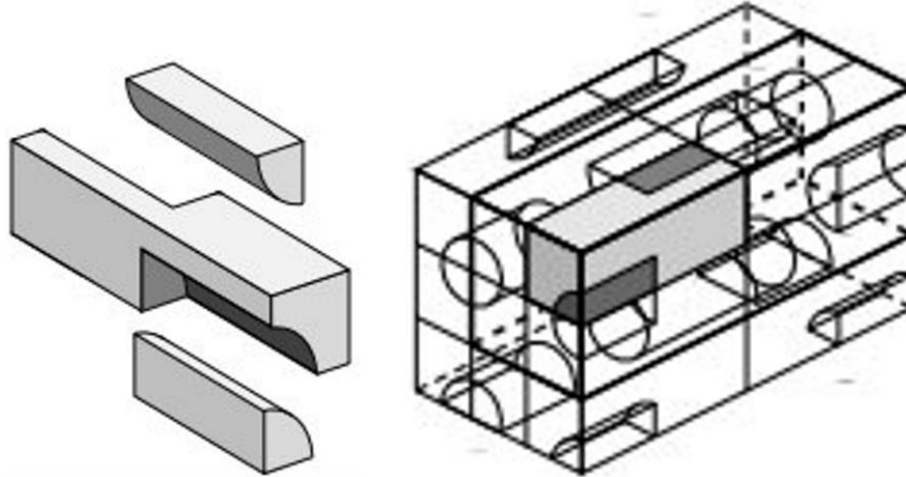


Figure 7. Three-dimensional RVE for modeling staggered hexahedral morphologies of discontinuous cylindrical inclusions. The shaded and bolded parts are suitable for symmetry and periodic boundary conditions respectively [45].

2.4.3. Periodic Micro-Field

One method for approximating microscopic and macroscopic mechanical responses of heterogeneous materials is the periodic micro-field approach. By employing this approach, periodic microstructure material models can be assessed using periodic RVEs. Likewise, the performances of infinite periodic arrays and microstructures under various loading and boundary conditions can be evaluated. Moreover, a large number of micromechanical models have been implemented to determine the optimum shape, size, and morphology of representative volume elements (RVEs) for various sophisticated microstructures including heterogeneous materials [42-45].

In periodic micro-field method, the stress and strain fields are separated into averaged macroscopic $\langle \sigma \rangle$ and $\langle \varepsilon \rangle$ as well as variable microscopic components $\sigma'(z)$ and $\varepsilon'(z)$. Figure 8 depicts the

idealized periodic micro-field with the variations of strain and corresponding displacements through z in a typical 1D periodic composite consisting of material A and B using periodic unit cell with length of c_z .

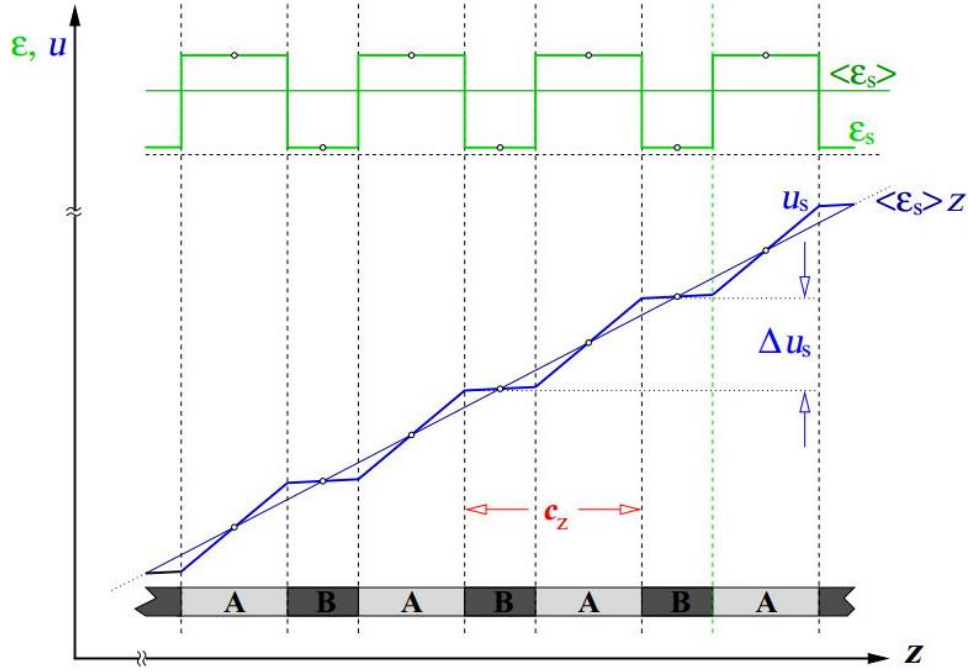


Figure 8. Variation of strains $\varepsilon_s(z)$ and displacements through $u_s(z)$ a typical 1D periodic composite comprise of material A and B with periodic unit of c_z . Small white dots represent the symmetry points of $\varepsilon_s(z)$ and $u_s(z)$ [45].

The relation between volume averaged strain $\langle \varepsilon_s \rangle$ and the incremental displacement per c_z can be written as follows:

$$\langle \varepsilon_s \rangle = \frac{\Delta \bar{u}_s}{\bar{c}_z} \text{ and } \bar{u}_s(z + p_z) = \bar{u}_s(z) + \langle \varepsilon_s \rangle \bar{c}_z \quad (4)$$

2.4.4. Periodic Boundary Conditions

RVEs with applied boundary conditions must be able to capture all deformation states, as well as stress and displacement compatibility at the surfaces for micromechanical problems. Accordingly, inclusion overlaps and gaps, as well as, other unphysical constraints must not have any effects on the deformations of RVEs. It means RVEs must be geometrically compatible. Hence, the boundary conditions of RVEs must be applied in a particular method that all deformation states can be captured via the model. Three different main boundary conditions can be employed in a periodic micro-field assessment include periodicity, symmetry, and anti-symmetry. In the periodicity micro-field approach models, one of these three types of boundary conditions or the combination of them can be applied, regardless of the numerical approach which is used to solve the equilibrium relations [42-45].

In general, for the typical periodic arrays, various RVE shapes and size can be employed particularly when point or symmetries have existed in the micro-geometry. For instance, Figure 9 indicates a 2D periodic hexagonal dispersion of circular heterogeneities. As it can be seen, many RVEs with different size, shape and boundary conditions can be utilized to assess the mechanical responses of this micro-geometry. One of the important capabilities of this approach is that for each type of arrangement in RVE, a particular boundary condition can be applied.

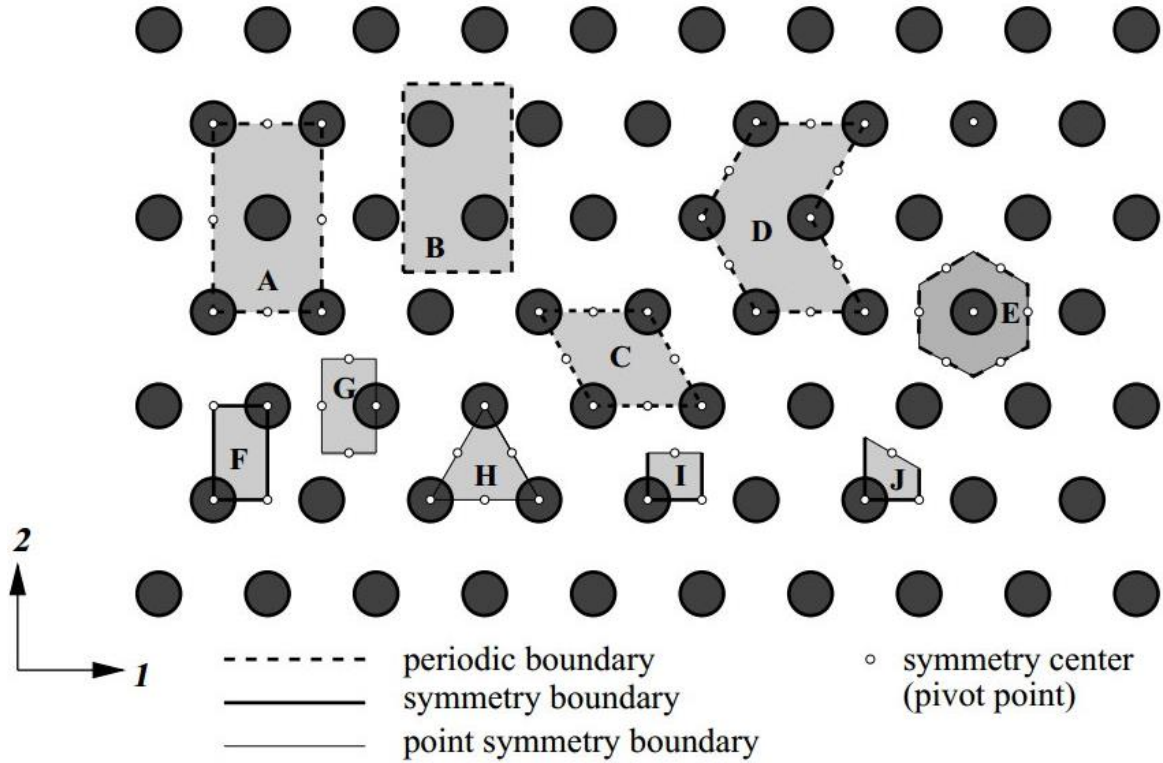


Figure 9. A variety of RVEs with different shapes, sizes, and boundary conditions which can be employed to evaluate the mechanical performances of a periodic hexagonal distribution of circular heterogeneous micro-geometry [45].

One of the most common and efficient types of boundary conditions for RVE is periodicity. By using periodic boundary condition, the total physical deformation states of the RVE can be captured; thus, heterogeneous materials such as biomimetic composites can be modeled with this concept.

For the purpose of defining N-dimensional periodic micro-geometry with non-uniformly dispersed inclusion, an optimum RVE and a set of N linear independent periodic vectors P_n are required (see Figure 10). The opposite surfaces of the RVE which are subjected to PBCs must comprise of at least N pairs of opposing faces Γ_k . The pattern of elements must also be analogous to create the

given pairs of k^- and k^+ which are shifted corresponding to each other via shift vectors \mathbf{c}_k . Any shift vector must be a linear combination of periodic vectors which can be defined as follows

$$\bar{\mathbf{c}}_k = \sum_l m_l^k \bar{\mathbf{P}}_l, \quad (5)$$

where m_l^k are integer numbers.

Figure 10 shows different matching opposite faces pairs which are marked by same line style and color.

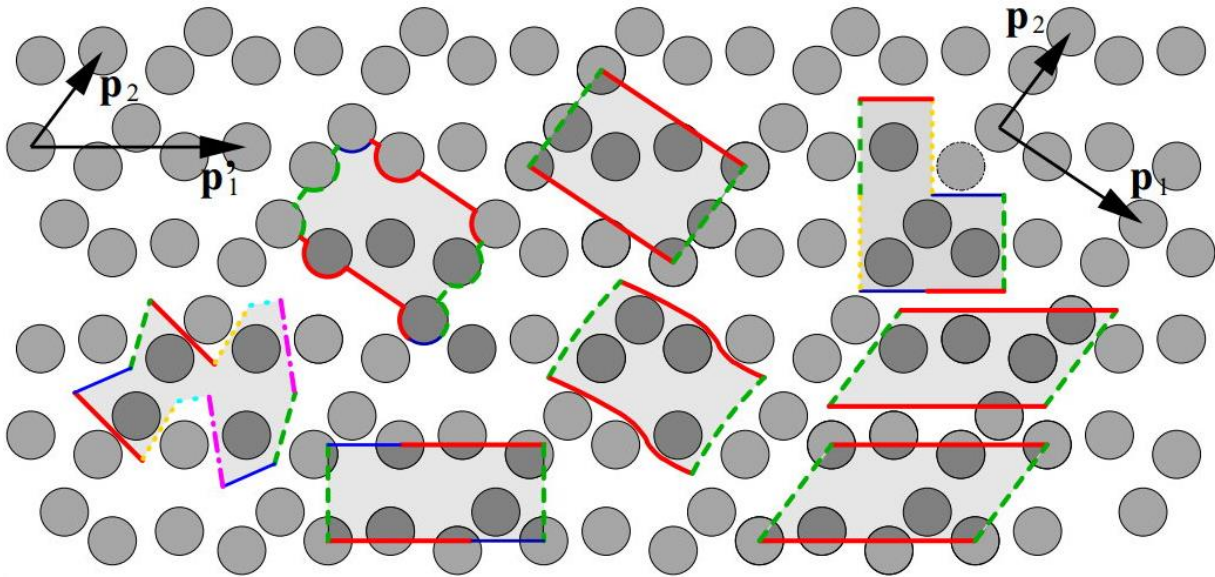


Figure 10. Various equal minimum-size periodic RVEs for a non-uniformly dispersed particles with two non-orthogonal periodic vector pairs include (P_1, P_2) and (P'_1, P_2) [45].

Accordingly, selecting a simple shape of RVE can promote the application of PBCs. These RVEs are generated and discretized for subsequent finite element analyses (FEA) which will be described in chapter 5. In fact, the meshing process of the low- or negative-angle intersections among boundaries, faces, and edges in the selected RVE can significantly be challenging. Selecting the shape of RVE also can be automated using various Voronoi tessellations; however, this method

can choose an irregular volume or shape. On the contrary, if orthogonal periodic vectors to be employed in selecting the shape or volume of RVE, then periodic rectangular or hexahedral RVEs with regular faces, edges, and vertices can be generated for micro-geometries.

For the multi-dimensional RVEs, Eq. (4) can be expanded by adding shift vector of c_k (see Figure 8) as

$$\bar{u}(z + c_k) = \bar{u}(z) + \varepsilon * \bar{c}_k \quad (5)$$

where u is displacement and c_k is equivalent to c_z for multi-directional RVEs. For any matching opposite faces, edges, and vertices pair, using Eq. (6) PBCs in the small strain regime can be applied (see Figure 8)

$$\Delta u_k = u_{k^+} - u_{k^-} = u(s_k + c_k) - u(s_k) = \langle \varepsilon \rangle * c_k \quad (6)$$

where s_k and $s_k + c_k$ are the position of mating nodes on opposing typical faces or edges; also, u_{k^-} and u_{k^+} are the displacements of corresponding node pairs. Thus, the deformed expression of shifting vector is $\hat{c}_k = c_k + \Delta u_k$. Based on Eq. (6) in which macroscopic strain $\langle \varepsilon \rangle$ was defined in displacement form, the displacement vector can be defined as the following

$$u_{k^+} = u_{k^-} + u_{M^+} - u_{M^-} \quad (7)$$

where u_{M^+} and u_{M^-} are the displacements of a typical matching node pair. By means of these nodal control, the information of \hat{c}_k is transported. These types of constraints compel all unit cells to have a monolithic fit condition in all deformation states.

For a rectangular 2D RVE shown in Figure 11. Eq. (7) can be written as follows:

$$u_N(\tilde{s}_1) = u_s(\tilde{s}_1) + u_{NW} \quad (8)$$

$$u_E(\tilde{s}_2) = u_w(\tilde{s}_2) + u_{SE}$$

which can directly imply for vertices as the following

$$u_{NE} = u_{NW} + u_{SE} \quad (9)$$

where \tilde{s}_k are local edge coordinates which are employed to specify mating nodes. In this RVE which is represented in Figure 11, the vertex SW is completely fixed.

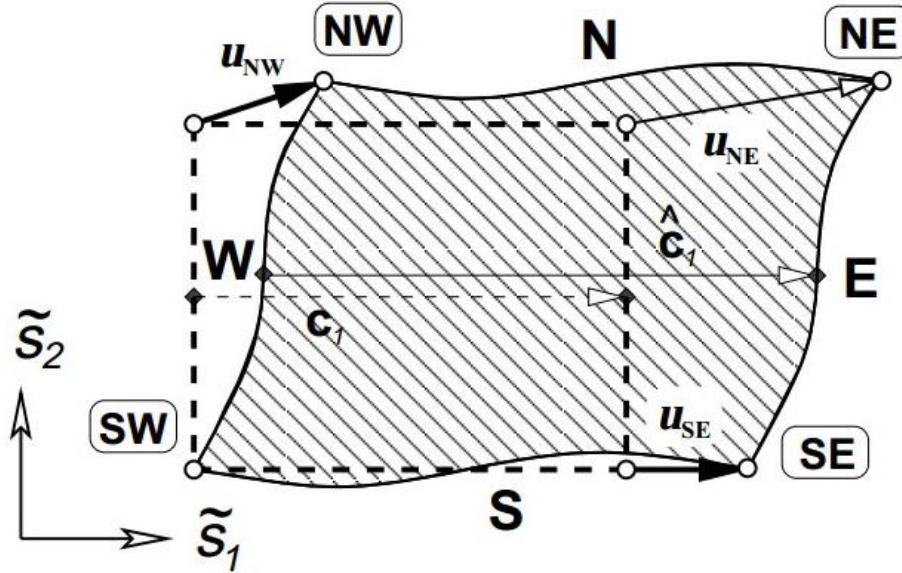


Figure 11. Scheme of periodic boundary conditions (PBCs) applied on a rectangular 2D RVE

[45].

For numerical analysis, the discretization of opposing faces and edges must have the analogous nodal coordinates \tilde{s}_k and each nodal pair must have separated constrain shifting vector. Thus, Eq. (8) leads to be the sets of three nodal displacement degree of freedoms (DOFs) in the form of linear constraints. By comparing Eqs. (6) and (8) demonstrates that the displacements of the master nodes

(i.e., SE and NW) which have the macroscopic strain tensor $\langle \varepsilon \rangle$ information. Furthermore, the displacements of the slave nodes (i.e., N and E in Figure 13) are totally controlled via master nodes displacements (i.e., S and W in Figure 11). Indeed, these types of implementation can be applied for any 2D and 3D periodic RVE which has even number of faces or edges.

2.4.5. Homogenization Theory

For the purpose of computing the bulk mechanical properties of the inhomogeneous materials (e.g., biomimetic composites) using 3D RVEs, a homogenization process as shown in Figure 12 must be employed [46-49]. Figure 12 (a) illustrates a heterogeneous periodic microstructure with volume, φ , under external forces per area, \bar{F} , on the boundaries, A_t , as well as exterior displacements per area, \bar{u} , on boundaries, A_u . Equilibrium relations, strain-displacement law, constitutive equations, and boundary conditions for a heterogeneous microstructure can be expressed using Eq. (10) to Eq. (14) respectively.

$$\sigma_{ij,j} + f_i = 0 \text{ in } \varphi, \quad (10)$$

$$\varepsilon_{ij} = \frac{1}{2}(u_{i,j} + u_{j,i}) \text{ in } \varphi, \quad (11)$$

$$\sigma_{ij} = C_{ijkl} \varepsilon_{kl} \text{ in } \varphi, \quad (12)$$

$$\sigma_{ij} n_j = \bar{F}_i \text{ on } A_t, \quad (13)$$

$$u_i = \bar{u}_i \text{ on } A_u, \quad (14)$$

where $\sigma_{ij,j}$ is the derivative of stress tensor components with respect to j , f_i are the prescribed body forces per unit volume, ε_{ij} represents strain tensor components in equilibrium equations, C_{ijkl} is the linear elastic material stiffness matrix, n_j denotes outward normal vectors on the volume boundaries. For inhomogeneous materials such as biomimetic composites, the stiffness matrix may vary in different regions of the microstructure, and hence the solution of Eqs. (10-14) becomes intricate. Therefore, addressing homogenized responses or averaged mechanical properties is essential for continuum-based calculations. As indicated in Figure 12 (b), by means of a simple RVE or unit cell with volume, φ_e , a heterogeneous periodic microstructure can be generated for homogenization. The terms φ_m and φ_i denote the matrix and inclusions volume fraction of the RVE respectively. Thus, $\varphi_e = \varphi_m \cup \varphi_i$ is the total volume of the RVE, and $A_e = A_{tm} \cup A_{um}$ represents the summation of exterior boundaries, where A_{tm} and A_{um} are regions under tractions and displacements respectively. Also, the interaction between inclusions and matrix can be assumed to be perfectly bonded.

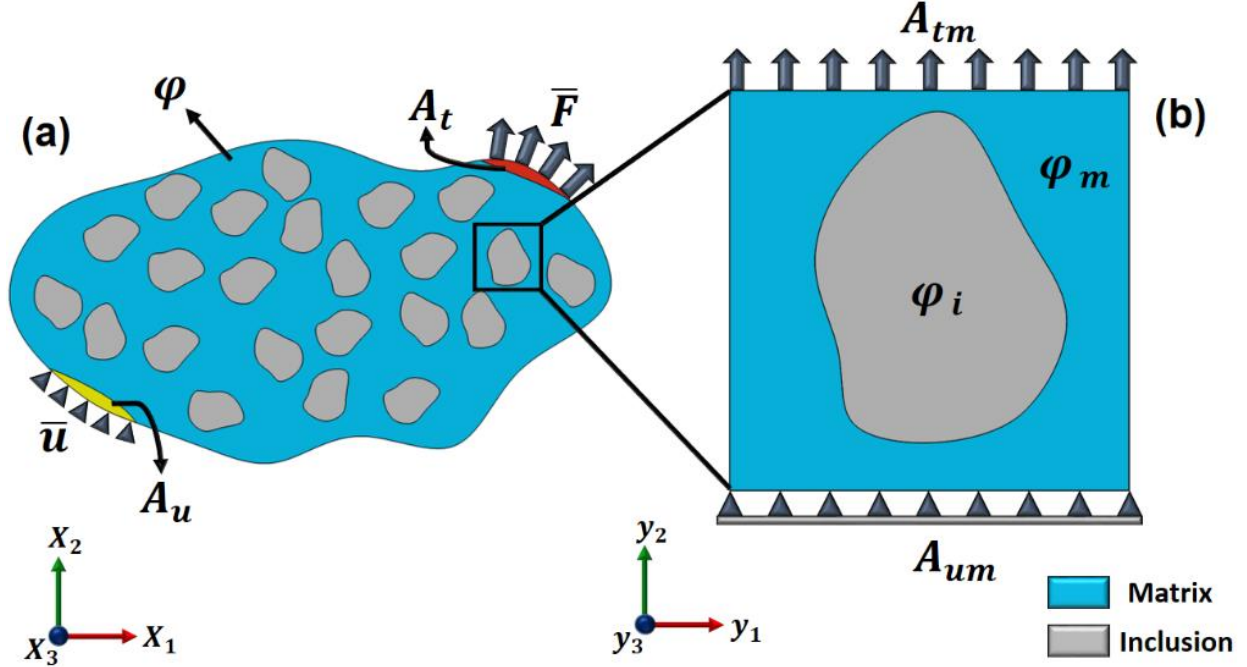


Figure 12. (a) Heterogeneous periodic microstructure of a representative biomimetic composite.

(b) a representative volume element (RVE) of composite microstructure with inclusion and matrix.

Jansson [46] derived the relation between volume average stress and volume average strain for the inhomogeneous materials which were defined as:

$$\langle \varepsilon_{ij} \rangle = \frac{1}{|\varphi_e|} \int_{\varphi} \varepsilon_{ij}^0(x, y) d\varphi_e = \varepsilon_{ij}^{(0)} \quad (15)$$

$$\langle \sigma_{ij} \rangle = \frac{1}{|\varphi_e|} \int_{\Psi} \sigma_{ij}^0(x, y) d\varphi_e = C_{ijkl}^H(\varepsilon^0) \langle \varepsilon_{kl} \rangle, \quad (16)$$

where $\langle \varepsilon_{ij} \rangle$ and $\langle \sigma_{ij} \rangle$ are sequentially volume averaged strain and stress for the RVE. ε_{ij}^0 and σ_{ij}^0 denote local strain and stress in the RVE respectively. The equivalent homogenized stiffness

matrix is introduced by C_{ijkl}^H . For a homogenized elastic microstructure, the relation between stress and strain can be expressed via Eq.(16). Additionally, for 3D RVEs, C_{ijkl}^H constants are calculated via applying six independent unit macrostrains and PBCs for six independent models.

$\varepsilon_{ij}^{(0)} = \frac{1}{2} \left(\frac{\partial u_i^0}{\partial x_j} + \frac{\partial u_j^0}{\partial x_i} \right)$ expresses imposed unit macroscopic strains for any six independent

loading cases. Thus, by means of the computed volume averaged stresses and strains in each case, one column of effective stiffness matrix can be calculated using the following

$$\begin{bmatrix} \sigma_{11} \\ \sigma_{22} \\ \sigma_{33} \\ \tau_{23} \\ \tau_{13} \\ \tau_{12} \end{bmatrix} = \begin{bmatrix} C_{1111} & C_{1122} & C_{1133} & 0 & 0 & 0 \\ C_{2211} & C_{2222} & C_{2233} & 0 & 0 & 0 \\ C_{3311} & C_{3322} & C_{3333} & 0 & 0 & 0 \\ 0 & 0 & 0 & C_{2323} & 0 & 0 \\ 0 & 0 & 0 & 0 & C_{1313} & 0 \\ 0 & 0 & 0 & 0 & 0 & C_{1212} \end{bmatrix} \begin{bmatrix} \varepsilon_{11} \\ \varepsilon_{22} \\ \varepsilon_{33} \\ \gamma_{23} \\ \gamma_{13} \\ \gamma_{12} \end{bmatrix} \quad (17)$$

The inverted form of C_{ijkl}^H matrix is compliance matrix S_{ijkl}^H . The elastic constants are calculated using the following S_{ijkl}^H coefficients:

$$[C] = [S]^{-1} \rightarrow [S] = \begin{bmatrix} \frac{1}{E_1} & \frac{-\nu_{21}}{E_2} & \frac{-\nu_{31}}{E_3} & 0 & 0 & 0 \\ \frac{-\nu_{12}}{E_1} & \frac{1}{E_2} & \frac{-\nu_{32}}{E_3} & 0 & 0 & 0 \\ \frac{-\nu_{13}}{E_1} & \frac{-\nu_{23}}{E_2} & \frac{1}{E_3} & 0 & 0 & 0 \\ 0 & 0 & 0 & \frac{1}{G_{23}} & 0 & 0 \\ 0 & 0 & 0 & 0 & \frac{1}{G_{13}} & 0 \\ 0 & 0 & 0 & 0 & 0 & \frac{1}{G_{12}} \end{bmatrix} \quad (18)$$

2.5. Analytical Models for Discontinuous Inclusion-Based Composites

Established analytical models, including Mori-Tanaka, modified shear lag and Halpin-Tsai, have been utilized to calculate the elastic properties of composites materials. These models are reviewed herein, while relevant predictions are presented in results section. In addition, several analytical solutions have been proposed to investigate the characteristics and properties of various natural and biological composites, such as stiffness, strength, toughness, and interfacial properties [50-53]. However, all of these models were 2D analytical solutions, and the third dimension, which defines inclusion shape and dictates whether plane strain constraint is imposed, has not been considered. Furthermore, analytical models often cannot account for the complexities of biomimetic composite microstructures, such as non-uniform inclusion distributions. computational micromechanical models can be used to better represent the material microstructure.

2.5.1. Mori–Tanaka Model

The Mori–Tanaka model can predict the elastic stiffness tensor of a composite material with assumed elliptical inclusions and interaction among inclusions and matrix using [42, 54-56]:

$$C_c = C_m + \varphi_i \langle (C_i - C_m) A_i \rangle \left[(1 - \varphi_i) I + \varphi_i \langle A_i \rangle \right]^{-1} \quad (19)$$

where C_c , C_m , and C_i are stiffness tensors of the composite, matrix, and inclusion respectively. φ_i is the inclusion volume fraction, I is fourth order unit tensor, and A_i is the dilute mechanical strain concentration which can be expressed as follows:

$$A_i = \left[I + S (C_m)^{-1} (C_i - C_m) \right]^{-1} \quad (20)$$

The elements of Eshelby's tensor S are the function of inclusion aspect ratio (ρ) and matrix Poisson's ratio (ν_m), which are presented in Table 2 and by Eqs. (21)-(25).

Table 2. Eshelby's tensor element for elliptical inclusions.

s_{11}	$4Q/3 + R I_3 + 2\rho^2 T$
$s_{22} = s_{33}$	$Q + R I_1 + 3T/4$
$s_{23} = s_{32}$	$Q/3 - R I_1 + 4T/3$
$s_{21} = s_{31}$	$-R I_1 - \rho^2 T$
$s_{12} = s_{13}$	$-R I_3 - T$
s_{44}	$Q/3 - R I_1 + T/4$
$s_{55} = s_{66}$	$2R - R I_1/2 + (1 + \rho^2) T/4$
All other s_{ij}	0

$$I_1 = \frac{2\rho}{\sqrt{(\rho^2 - 1)^3}} \left(\rho\sqrt{\rho^2 - 1} - \cosh^{-1}(\rho) \right) \quad (21)$$

$$Q = \frac{3}{8(1 - \nu_m)} \quad (22)$$

$$R = \frac{1 - 2\nu_m}{8(1 - \nu_m)} \quad (23)$$

$$T = Q \frac{4 - 3I_1}{3(\rho^2 - 1)} \quad (24)$$

$$I_3 = 4 - 2I_1 \quad (25)$$

2.5.2. Modified Shear lag

Another well-known analytical model for discontinuous composites is shear lag model, which many versions have been developed [43, 44]. A modified shear lag model is employed herein to predict longitudinal modulus (E_1) of aligned discontinuous composites using the following:

$$E_1 = E_i \varphi_i \left[1 - \frac{(E_i - E_m) \tanh \left(\frac{l}{h} \left[\frac{2E_m}{E_i (1 + \varphi_m) \ln \left(\frac{l}{\varphi_i} \right)} \right]^{0.5} \right)}{E_i \left(\frac{l}{h} \left[\frac{2E_m}{E_i (1 + \varphi_m) \ln \left(\frac{l}{\varphi_i} \right)} \right]^{0.5} \right)} \right] + E_m (1 - \varphi_i) \quad (26)$$

where E_i and E_m represent Young's modulus of inclusion and matrix respectively. φ_i and φ_m denote inclusion and matrix volume fraction respectively, and l is the length of cylindrical inclusions or diameter of hexagonal inclusions. Moreover, h is the diameter of cylindrical inclusions or the thickness of hexagonal inclusions.

2.5.3. Halpin-Tsai Model

Another well-known model used to predict the longitudinal Young's modulus of discontinuous composites is Halpin Tsai model, which is defined as follow [43, 44]:

$$E_1 = E_m \left[\frac{1 + \left(\frac{2l}{h}\right) \left(\frac{\left(\frac{E_i}{E_m}\right) - 1}{\left(\frac{E_i}{E_m}\right) + \frac{2l}{h}} \right) \varphi_1}{1 - \left(\frac{\left(\frac{E_i}{E_m}\right) - 1}{\left(\frac{E_i}{E_m}\right) + \frac{2l}{h}} \right) \varphi_1} \right] \quad (27)$$

this model also is used to predict and compare the Young's modulus of discontinuous composites with other analytical models and finite element micromechanical models.

2.6. Computational Micromechanical Modeling of Biomimetic Composites

Micromechanical finite element (FE) modeling provides an efficient means to conduct virtual experiments for various material systems during design, while at the same time allowing for greater flexibility with regards to assessing material nonlinearities and local damage progression of bioinspired composites. Mirkhalaf and Barthelat [35] developed a 2D RVE to assess the longitudinal performance of nacre-mimetic composites. Recently, Mirkhalaf and Ashrafi [54] proposed 2D RVEs to explore the effects of voids on the mechanical performance of staggered microstructures. During the past decade, Barthelat and coworkers [57-61] have proposed 2D and 3D RVEs to characterize the interfaces and junctions of the nacreous layer from mollusk shells. These studies have made notable contributions; however, most proposed FE models for biological or biomimetic composites utilized 2D RVEs, the limitations of which include the inability to assess out-of-plane mechanical properties or 3D damage evolution under realistic and practical multiaxial

stress states. Although several 3D FE micromechanical models have been proposed to characterize various staggered and aligned discontinuous inclusion-reinforced composites, overall microstructure, inclusion shape, and boundary conditions are often simplified and not an accurate representation of the material. Also, complicated algorithms are often employed to generate 3D RVE geometries, mesh schemes, and apply periodic boundary conditions [62]-[66]. In addition, the influences of various inclusion shapes and aspect ratios under different stress states have not been broadly compared using micromechanical FE models. Hence, to accurately assess the local damage evolution or 3D mechanical properties of biomimetic materials, 3D RVEs with staggered or aligned microstructures consisting of non-uniformly dispersed inclusions with various shapes are required. This is challenging, particularly if periodic geometries and boundary conditions are required.

One of the significant obstacles in modeling 3D multi-inclusion RVEs is to randomly generate non-uniform inclusion distributions efficiently, in particular for RVEs with high fiber volume fractions. In this regard, a number of algorithms have been developed [67-75]. The hard-core random distribution algorithm (HCRDA) was established by Yang et al.[67], while extensions such as the close packing model [68], stirring method [69] and random sequential expansion (RSE) algorithms [70] were also developed to overcome the jamming limitation of the HCRDA. The HCRDA is not efficient in generating RVEs with high fiber volume fractions [71]. The nearest neighbor algorithm (NNA) was later developed by Vaughan and McCarthy [73]. Due to the inter-fiber problem of NNA, the modified NNA (MNNA) was proposed by Wang et al. [74]. Furthermore, Zhang and Yan [75] proposed elastic collision algorithm (ECA). The principal drawback for the aforementioned algorithms is an inefficiency or inability to randomly generate RVEs with non-uniform dispersions and high fiber volume fractions. Moreover, due to jamming

limitations, these algorithms are not efficient in randomly generating 3D RVEs with non-uniformly dispersed periodic staggered inclusions with high volume fractions. Recently, Li et al. [76] and Bahmani et al. [49] proposed an algorithm employing event-driven molecular dynamics to generate high spherical inclusion volume fraction 3D RVEs; however, this new approach cannot still be utilized for various inclusion shapes.

Therefore, in order to compute other mechanical properties of these materials, a computational tool is required. In the following chapter different steps of the developing this computational tool which is enabled to calculate orthotropic elastic properties are described.

Chapter 3: Computational Models Development

In this chapter, the required algorithm to generate the geometry of micro-and nanostructure of various biomimetic composites are described. Afterward, 3D FE micromechanical modeling requirements include periodic geometry, mesh, and boundary conditions are explained.

3.1. Generating Non-uniformly Staggered Periodic Microstructure

In order to randomly generate 3D RVEs with non-uniformly dispersed periodic staggered or aligned inclusion coordinates, the 3D Staggered Hard-Core algorithm (SHCA) was used. This algorithm was compiled based on the well-known Hard-Core model. In the primary hard-core model, randomly dispersed particles are generated through an isotropic core (i.e., disc or sphere), non-periodic, and non-staggered morphology. However, for the studied biomimetic materials, hexagonal or cylindrical particles with various aspect ratios in a non-uniformly staggered or aligned scheme were considered in the SHCA, while RVEs had periodic geometries for applying PBCs. The 3D SHCA flowchart illustrated in Figure 13 was implemented into MATLAB software for generating non-uniformly staggered and aligned inclusions in 3D RVEs with inclusion volume fractions up to 40%. A volume fraction of 40% is remarkably high for 3D discontinuous staggered and aligned inclusion-reinforced composites.

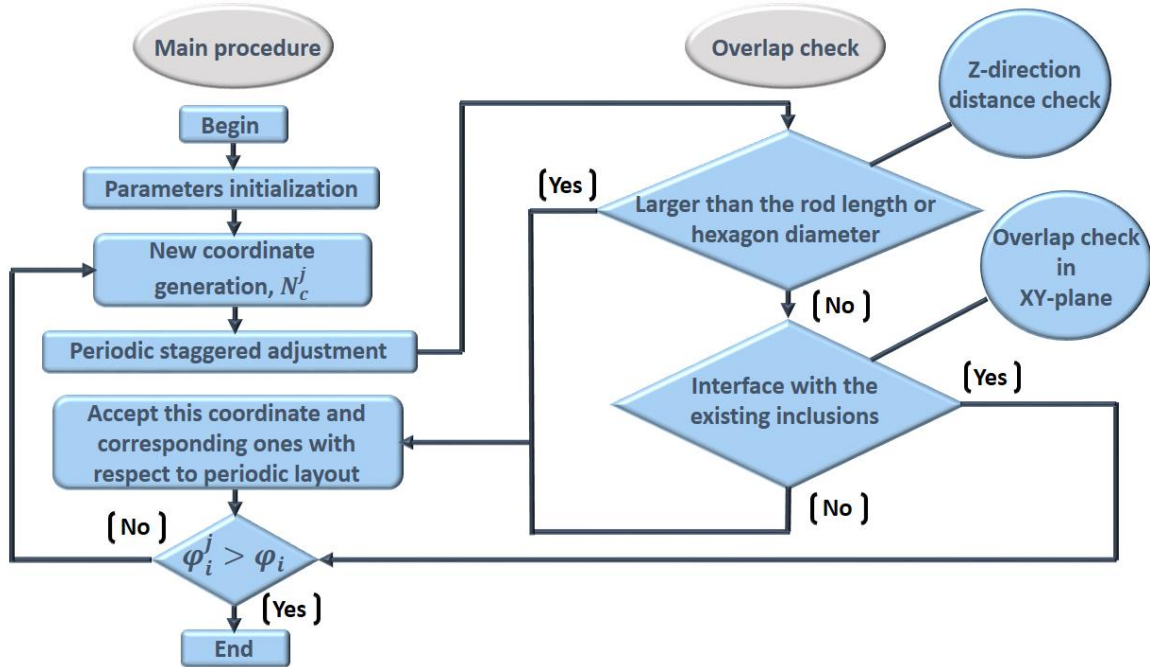


Figure 13. Flowchart of the 3D staggered hard-core algorithm (SHCA).

As can be seen in Figure 13, the SHCA includes a main procedure and an overlap check function. The main procedure begins with parameters initialization which consists of the RVE dimensions, inclusion shapes and aspect ratios, as well as, desired inclusion volume fraction. Subsequently, the new coordinate is generated by random function in MATLAB software. Periodic staggered adjustment is executed while the coordinate is adjacent to corners, exterior edges, and surfaces. Afterward, specific field and new coordinates will be generated to maintain geometric periodicity. Moreover, inclusion intersections for each generated coordinate are examined using overlap check function. The depiction of overlap check functions for hexagonal and cylindrical inclusions are shown in Figure 14 and Figure 15 respectively. For overlap check function of hexagonal inclusions, each hexagon edge and vertex must be checked to distinguish inclusion intersections. Figure 14 exhibits closest aggregate hexagons. Hexagon R_f in the middle is reference one and others are nearest hexagons to R_f . In order to avoid inclusion intersections, the center of newly

generated hexagon must be retained outside of the orange dash-dot line. Further depictions are indicated in the fourth quarter of XY-plane in Figure 14 (b) where O_r is XY-coordinate origin and center of R_f , also, O_1 , O_2 , and O_3 are the center of three typical nearest hexagons to R_f . Thereupon, the function of orange dash-line can be expressed as:

$$\begin{cases} |y' - y_r| = \sqrt{3}r, (\theta \geq 60^\circ) \\ |y' - y_r| = (2\sqrt{3}r - \sqrt{3}(|x' - x_r|)), (\theta < 60^\circ) \end{cases}, \quad (28)$$

where (x_r, y_r) and (x', y') are the center coordinates of R_f and newly generated hexagon respectively.

r is the radius of the hexagon circumscribed circle, and θ is defined as:

$$\theta = \arctan\left(\frac{(y_r - y')}{(x_r - x')}\right) \quad (29)$$

Other three quadrants follow the same procedure to guaranty generating of newly non-intersected hexagons. With regards to inclusion intersections in Z-direction illustrated in Figure 14 (c), YZ-coordinates must be checked, if Z-coordinate of the newly-generated hexagon is within range of R_f thickness.

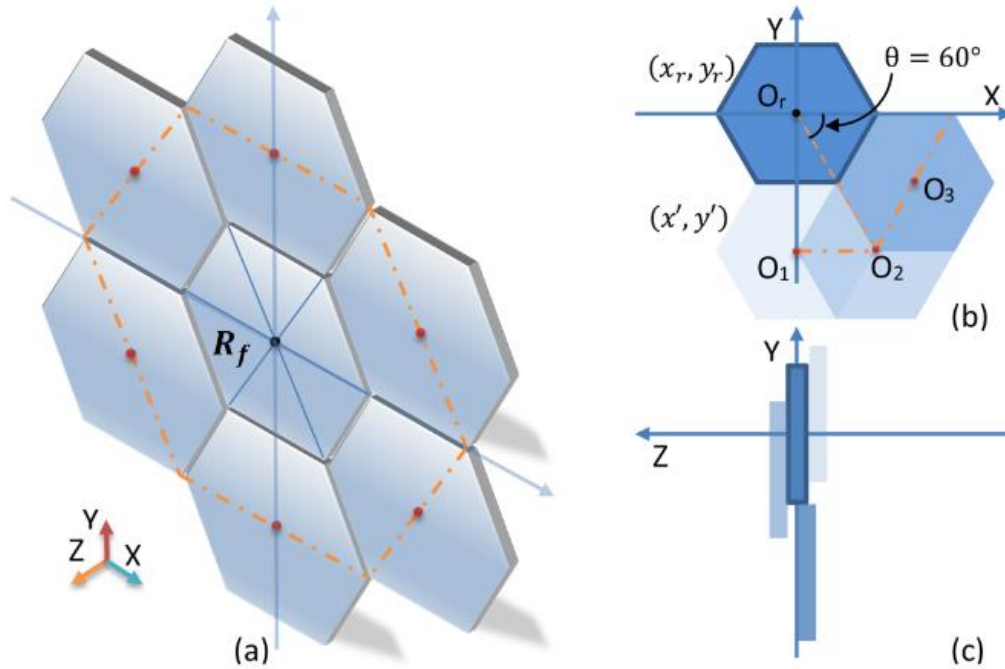


Figure 14. 3D and 2D views of overlap check function for hexagonal inclusions.

With regards to the overlap check function for cylindrical inclusion, analogous principals are applied. However, as it is shown in Figure 15 (a-b), in the XY-plane, the distance between cylinder R_f and newly generated rod must be greater than R_f diameter while in Z-direction distance between two cylinders must be less than rod length (see Figure 15(c)).

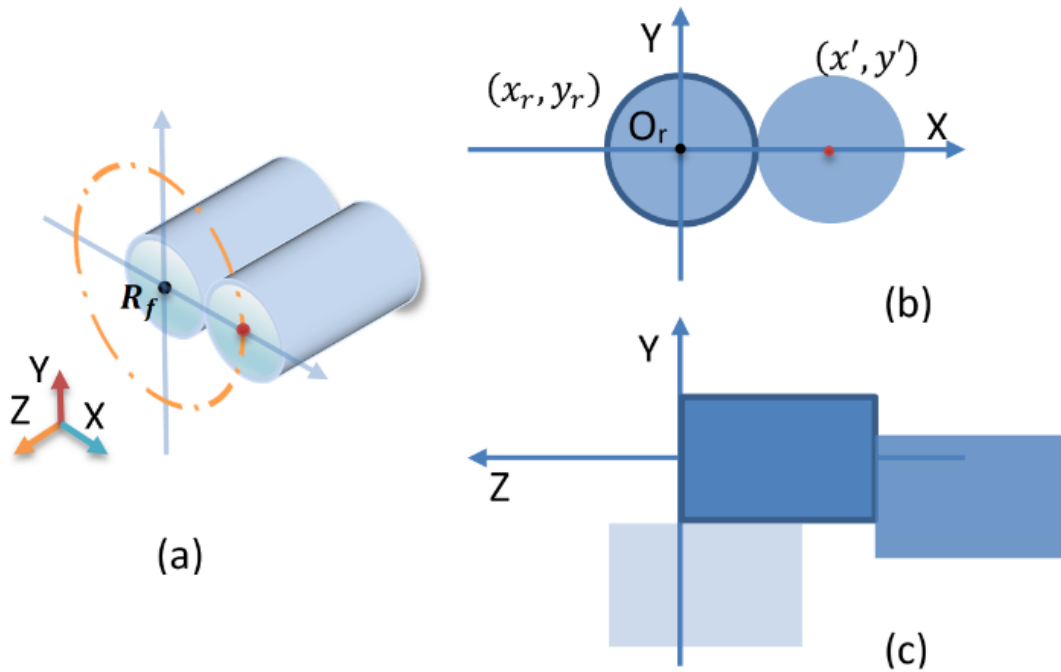


Figure 15. 3D and 2D views of overlap check function for cylindrical inclusions.

Eventually, the inclusion coordinates, as generated above, were imported into the commercial finite element software ABAQUS to produce 3D periodic staggered or aligned RVEs using customized PYTHON scripts for subsequent finite element analysis. Figure 16 (a) and (b) depict the dimensions of both considered inclusions, along with the definition of aspect ratio, $\rho = L / h$

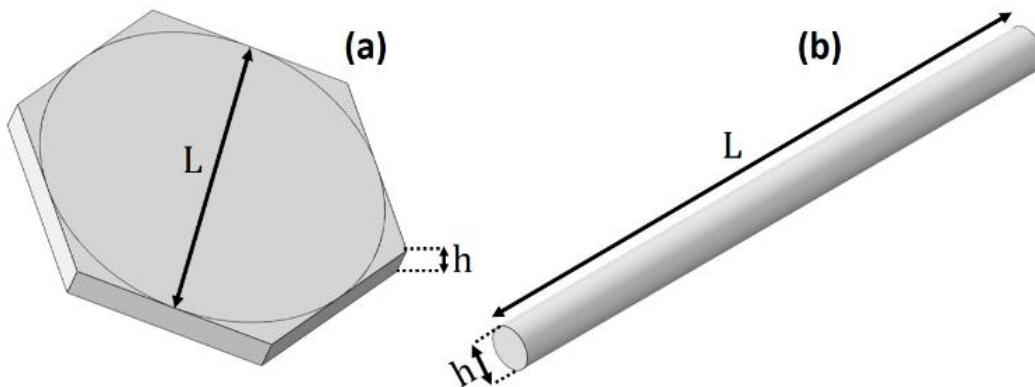


Figure 16. Inclusion dimensions used in aspect ratio (ρ) calculation for 3D RVE models. (a)

hexagonal platelet, (b) cylindrical inclusion.

The silanized nanohydroxyapatite (Si-nHA) particles used in this study have the cylindrical shape with $\rho = 4$ and different volume fractions such as 10%, 20%, 25%, and 30%. Therefore, to FE micromechanical assessment of these materials, 3D RVEs are modeled based on these characteristics, and the results are presented in Section 6.2. The length, width, and height of the 3D RVE are 400, 200, and 200 nm.

During the initial verification of developed 3D FE micromechanical models, other types of biomimetic materials are modeled. Three different aspect ratios ($\rho = 5, 15, 25$) for four inclusion volume fractions ($\varphi_i = 10, 20, 30, 40$) were explored for both hexagonal platelet and cylindrical particle models. Due to the distinct shape of inclusions considered, the corresponding 3D RVE sizes were different. The length, width, and height of hexagonal platelet 3D RVE are 15, 15, and 5 μm . The length, width, and height of cylindrical inclusion 3D RVE are 5, 5, and 15 μm . Note that these chosen dimensions for 3D RVEs are validated with experimental data in Section 6.1. Figure 17 illustrates generated 3D periodic RVEs with non-uniformly dispersed staggered hexagonal (i.e., flake-like) and aligned cylindrical inclusions for a 30% volume fraction. Light blue particles are inclusions intersecting the outer surfaces, and yellow particles are inclusions within RVE.

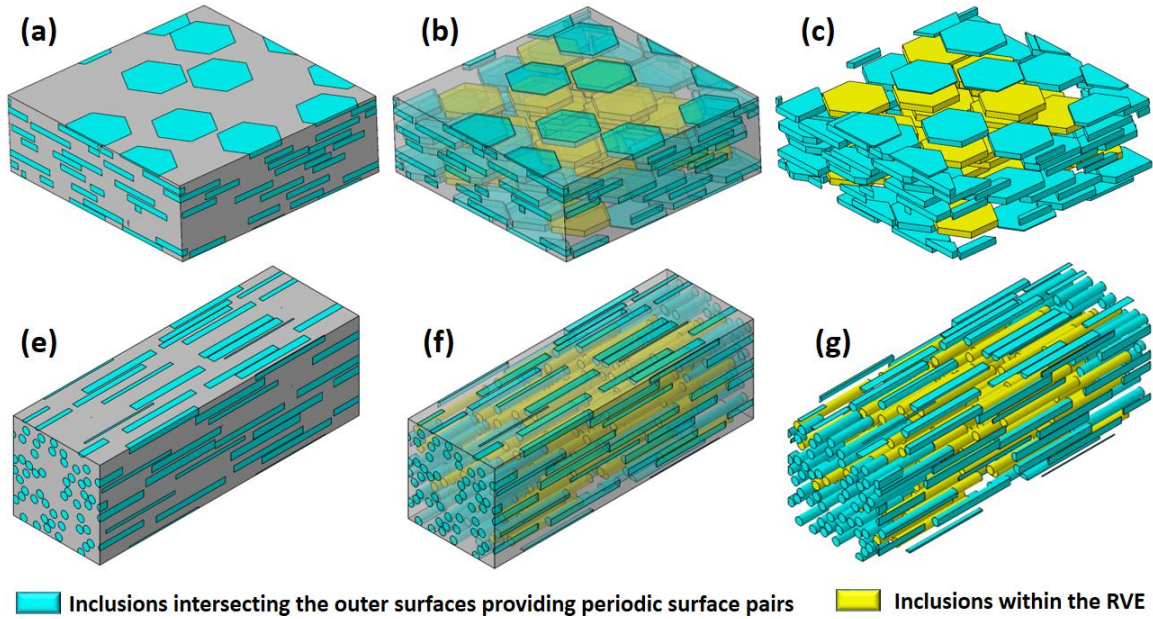


Figure 17. Created periodic 3D RVEs with randomly distributed (a-c) staggered hexagonal platelets and (e-g) aligned cylindrical inclusions with 30% volume fraction.

3.2. 3D Assessment of Generated Staggered Random Dispersions

The degree of nonuniformity of the generated staggered and aligned inclusions was assessed using 3D spatial analysis functions. Several approaches have been derived from 2D analyses to evaluate the 3D spatial distributions of the inclusions and to verify their degree of nonuniformity. The nearest neighbor analysis is the classical method that was used to show the regularity of distributions. In this study, 3D autocorrelation analysis was employed to assess the degree of nonuniformity of the generated staggered and aligned particles. 3D autocorrelation analysis describes the relative position of each inclusion in a region relative to not only the nearest inclusions but also, every other inclusion. Figure 18 and Figure 19 illustrate the 3D autocorrelation analyses in a typical volume fraction (e.g., 30%) for generated non-uniformly staggered hexagonal (i.e., flake-like) and aligned cylindrical inclusions respectively. The 3D autocorrelation diagram is

depicted by taking one inclusion as the reference and plotting the relative positions of all other inclusions within a spherical space. This space is composed of several layers, and within each layer, the density of inclusions is utilized to define density recovery profile (DRP) (see [77]-[78] for more details). Figures 18 (a) and 19 (a) show the 3D autocorrelation analysis DRPs for 3D RVEs with randomly dispersed inclusions and 30% volume fractions. The remaining plots in Figures 18 and 19 exhibit distance distributions and two direction distributions of the random inclusions relative to the reference inclusion (i.e., azimuthal angle, θ , and elevation angle, ϕ), which make up the spherical coordinate autocorrelation tri-histogram plots. The constant DRP values at an average magnitude within the spherical space for Figure 18 (a) and 19 (a) demonstrate that these 3D RVEs have consistent nonuniformly distributed inclusions. For the direction distribution analysis shown in Figure 18 (b) and 19 (b), the generated 3D RVEs have consistent inclusion densities in all radial directions for both the θ and ϕ angles, which is represented by circles with smooth edges. This further implies that the inclusions in these 3D RVEs have consistent nonuniform random distributions, and thus accurately depict the microstructure of the studied materials.

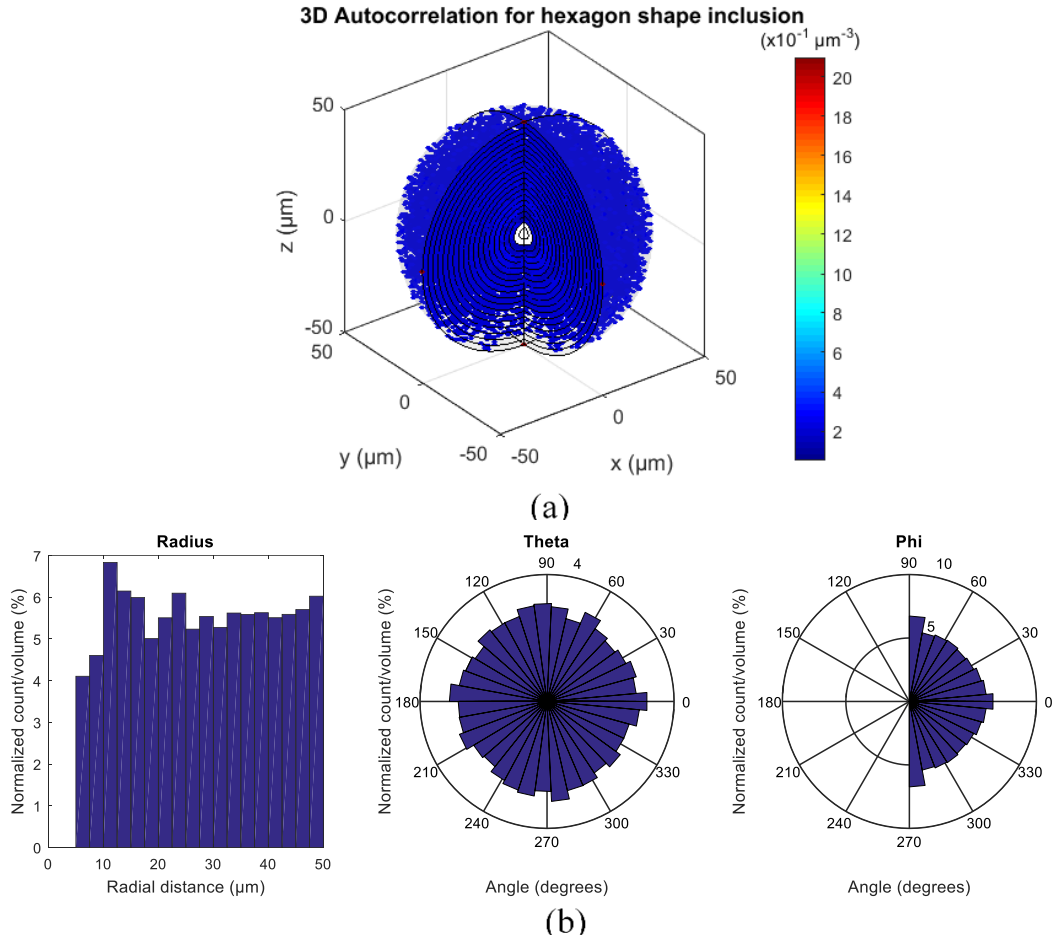


Figure 18. (a) 3D Autocorrelation analysis and density recovery profile (DRP) for 3D RVEs with hexagonal inclusions for 30% volume fraction. (b) autocorrelation tri-histogram plots.

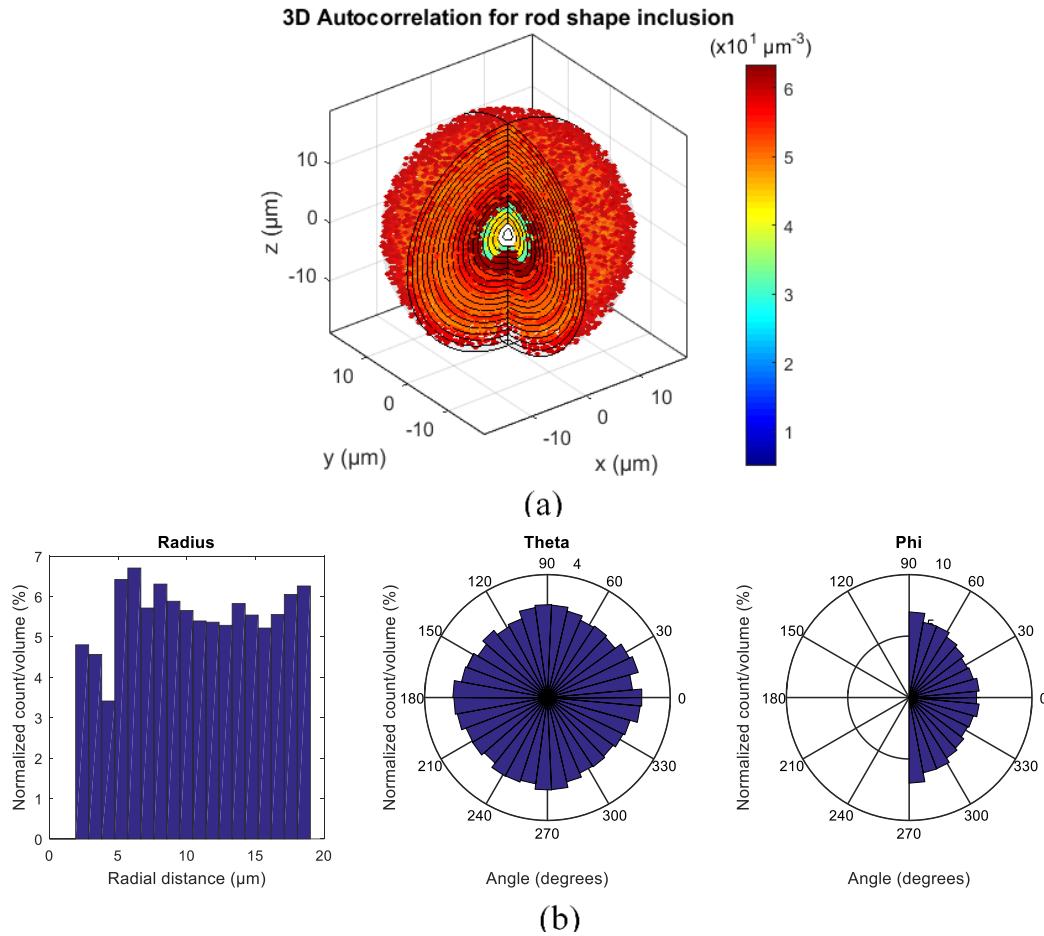


Figure 19. 3D Autocorrelation analysis and density recovery profile (DRP) for 3D RVEs with cylindrical inclusions for 30% volume fraction. (b) autocorrelation tri-histogram plots.

The main benefits of the developed SCHA when compared to previously reported algorithms include (i) applicability for multiple distinct biomimetic materials, (ii) rapid generation of 3D periodic staggered or aligned RVEs within minutes, and (iii) ability to generate 3D RVEs for high inclusion volume fractions (i.e., 40%).

3.3. Modeling in ABAQUS

The generated 3D RVEs, beginning with the creation of the RVE volumes, were subsequently implemented into ABAQUS using custom PYTHON algorithms for further preprocessing prior to analysis. In order to implement node-to-node constraint equations (CEs) for the proper application of PBCs, a scheme was developed to generate the required resembling element meshes on opposite surfaces of the 3D RVEs. The geometries of both 3D RVEs are complicated, thus utilizing hexahedral elements with the simple sweep or structure meshing options could not be conducted. Therefore, a copy mesh module in ABAQUS was extended using customized Python scripting for this purpose by utilizing dummy elements, followed by final volumetric meshing with 3D tetrahedral elements. Figures 20 (a-b) illustrate the flowchart of meshing procedure and typical example of analogous mesh patterns on corresponding periodic exterior surfaces of the 3D RVE. For instance, Figures 20 (b) exhibit the typical facing regions of the 3D RVE.

Several studies reported that generating matching mesh patterns for 3D RVEs with various commercial FE software was impracticable, thus complicated and time-consuming meshing and PBCs algorithms were implemented. Likewise, additional meshing software such as HYPERMESH was employed [62-66]. Note that extending the copy mesh module in ABAQUS with use of a dummy element technique, and subsequent use of constraint equations for application of PBCs for 3D RVEs was performed with ease in this study. This is a unique accomplishment in ABAQUS. As seen in Figures 20 (b), due to the complex and periodic microstructure, implementation of the developed meshing technique requires a diminutive mesh or seed size. However, this was not a limitation for the materials studied here.

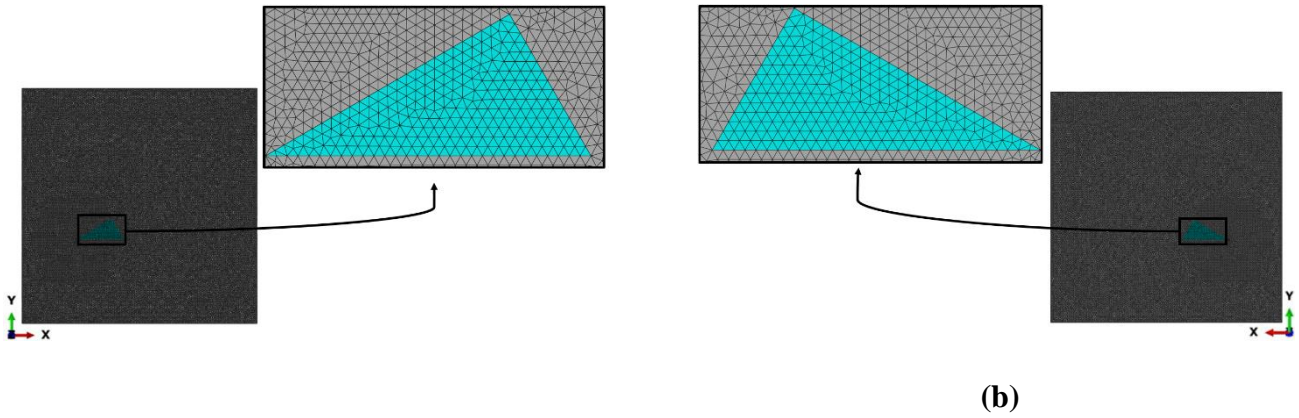
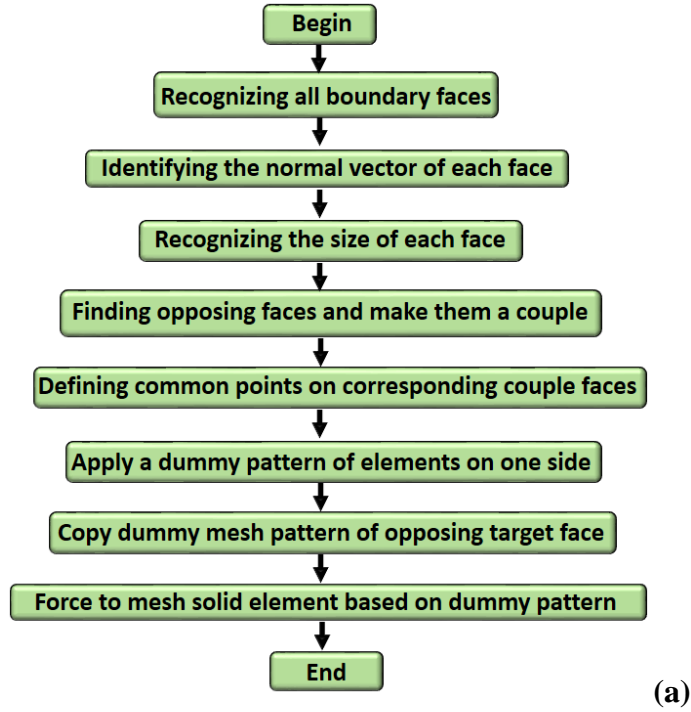


Figure 20. Identical 3D mesh pattern on corresponding opposing surfaces of the 3D RVE generated in ABAQUS by customized copy mesh module. (a) meshing procedure flowchart (b) typical regions on facing exterior periodic surfaces of the 3D RVE.

Isotropic linear elastic properties were designated for both inclusions and matrix. Their interface was modeled as perfectly bonded. Both models were run four different times with various materials

properties for different purposes which are indicated in Table 3. First, hexagonal inclusion 3D RVEs were run to compare results with experimental data from Mirkhalaf and Barthelat work [35] which was a chitosan/ micro-platelet alumina biomimetic composite. Also, cylindrical inclusions 3D RVEs were run to compare results with experimental data from Fu et al. work [79] which was a polypropylene/micro-carbon short-fiber composite. Afterward, both models were run for different inclusion volume fractions (i.e., 10, 20, 30, 40%) by using Mirkhalaf and Barthelat [35] material properties to compare the results of both models with 2D RVEs proposed with Mirkhalaf and Barthelat [35] and analytical models described in Section 2.5. Also to computed other orthotropic elastic constants. Finally, cylindrical inclusion 3D RVEs were run for generated nanocomposite in this project by utilizing two different elastic properties which were measured from experimental tests in this project, and they are described and presented in next sections.

Table 3. Different elastic properties used in both 3D RVEs for different purposes.

Purposes	Inclusion dimensions	Models	Material properties
Compare 3D RVE results with literature experimental data	Micro-scale	Hexagonal inclusion [35]	$E_i = 330 \text{ GPa}$
			$E_m = 1.88 \text{ GPa}$
		$\nu_i = 0.2$	
		$\nu_m = 0.4$	
Cylindrical inclusion [79]	$E_i = 238 \text{ GPa}$		
	$E_m = 1.30 \text{ GPa}$		
$\nu_i = 0.2$			
$\nu_m = 0.45$			

Compare 3D RVE results with 2D RVEs and analytical models	Micro-scale	Hexagonal inclusion [35]	$E_i = 330 \text{ GPa}$ $E_m = 1.88 \text{ GPa}$
		Cylindrical inclusion [79]	$\nu_i = 0.2$ $\nu_m = 0.4$
Compare 3D RVE results with experimental data of this study	Nano-scale	Cylindrical inclusion [80]	$E_i = 114 \text{ GPa}$ $E_m = \text{Table 6 and 7}$
			$\nu_i = 0.27$ $\nu_m = \text{Table 7 and 8}$

A summary of the assumptions made in developing computational models follows:

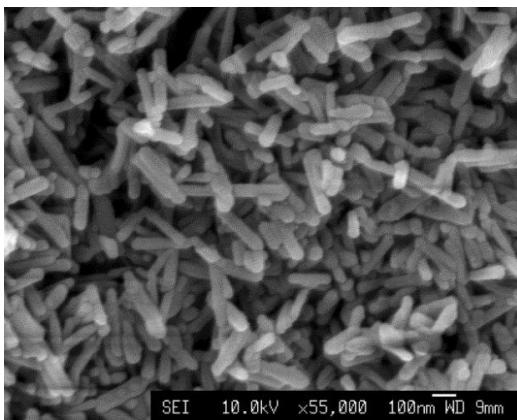
- Inclusions have identical geometry.
- Inclusions are non-uniformly dispersed.
- Inclusions are periodic and fully aligned.
- The interface between inclusions and matrix is perfectly bonded.
- The inclusion properties used have not been validated.
- The behavior of inclusions and matrix are isotropic linear elastic.

Chapter 4: Materials and Sample Fabrication

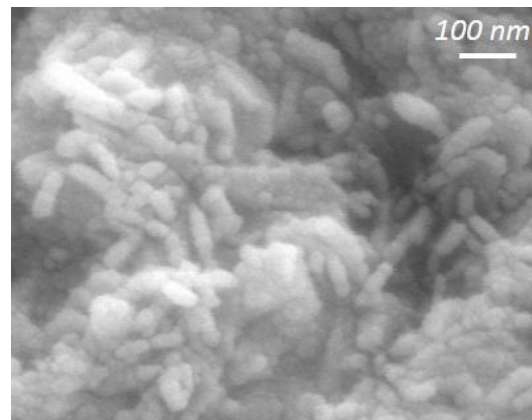
In this chapter, details of the constituent materials and fabrication processes for the studied nanocomposite materials are presented. Several important parameters in fabricating these materials including the quality of the inclusion/matrix interfacial bond, inclusion dispersions and alignments are assessed and indicated.

4.1. Silanization of Nano-hydroxyapatite

As mentioned earlier, one of the crucial parameters in determining the mechanical performance of a composite is the inclusion shape. In this project, for 3D-printing, cylindrical or rod shape nano-hydroxyapatite (nHA) inclusions were employed. Figure 21 (a) demonstrates the shape of these particles which are captured by other research groups [81] using SEM; while Figure 21 (b) shows the similar shape of nHA particles which is employed in this project and captured by SEM. Crystal percentage phase of these nHA particles was ~55 %, and the diameter and length of these nano-rods were ~30 nm and ~120 nm; these values were provided by the supplier.



(a)



(b)

Figure 21. The shape of hydroxyapatite nano-rods[81].

The silanization process was performed on nHA particles to improve interface bonding between nano-particles and biopolymeric resins which this bonding improvement reported in other studies [82]. Silanized nanohydroxyapatit (Si-nHA) could also create bone apposition at the surface of implants and improve bioactivity more than nHA [83-87].

Cylindrically shaped nHA particles with the density of 2.92 g/cm^3 and ~55% crystalline phase were purchased from MKNano. A solvent mixture of 90 vol% ethanol (EtOH) and 10 vol% deionized water (dH_2O) was mixed and prepared using stirring at 200-300 rpm. A 5.0 vol% of 3 methacryloxypropyltrimethoxysilane (MPTS) (Sigma Aldrich) was added to the solvent mixture. The pH of MPTS-solvent mixture was adjusted to 4 using 3.0 M acetic acid. The buffered MPTS-solvent mixture was stirred for 1 hr to hydrolyze (i.e., activate). Then, 10g nHA powders were added to the MPTS-solvent mixture and sonicated for 15 min. After sonication, the nHA/MPTS-solvent mixture was stirred for 24 h at room temperature. Afterward, to rinse ethanol and remove physically adsorbed silanes, the nHA/MPTS- solvent mixture was dialyzed using dialysis tubing in dH_2O for 1 hr. The Si-nHA powder was dried for 3 days at room temperature (see [82] for more details). In order to ensure about the silanization procedure, several Energy-dispersive X-ray spectroscopy (EDX) assessments were performed. Figures 22 (a-b) show the approximate weight percentages of *Si* on the nHA powder in various region of the powder.

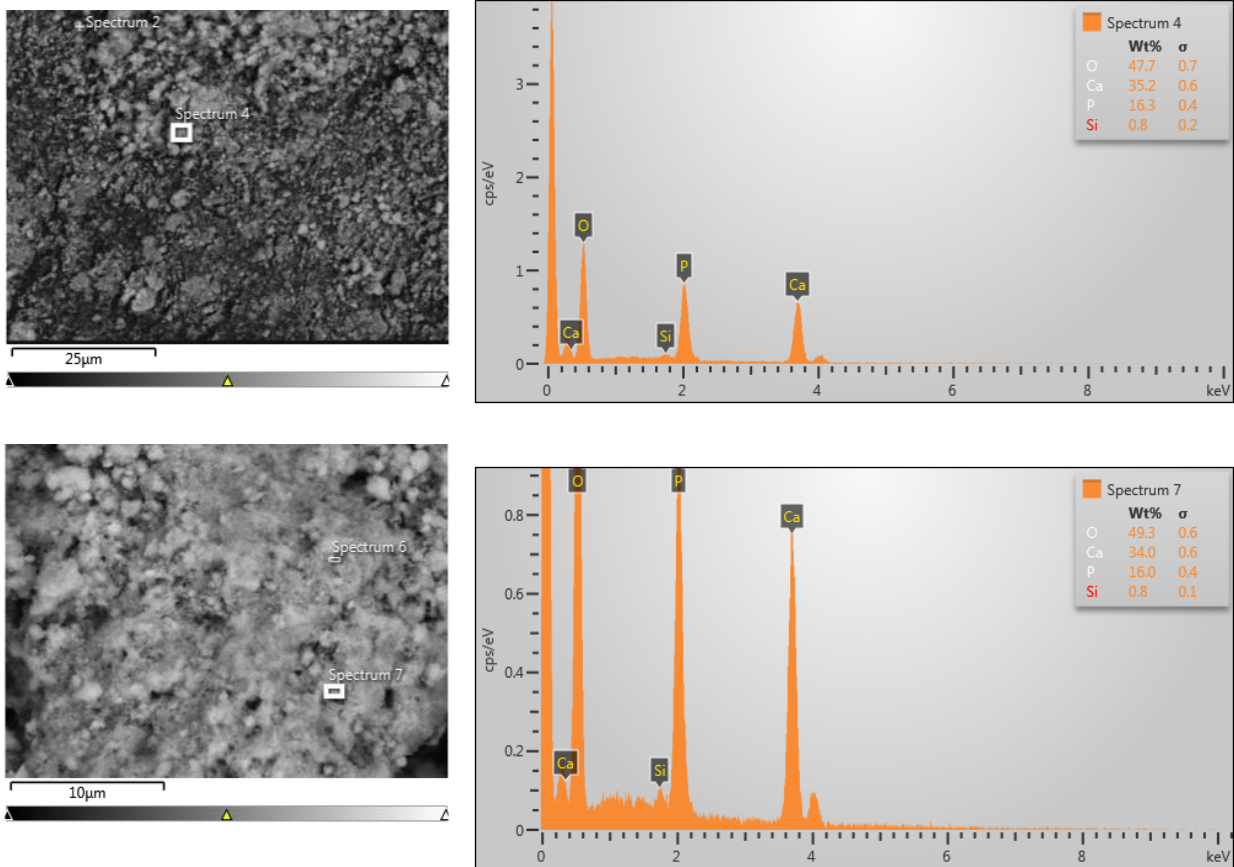


Figure 22. Energy-dispersive X-ray spectroscopy (EDX) results in various regions of Si-nHA powder.

4.2. Preparation of 3D-printable Nanocomposite Inks

Recently, the utilization of vegetable oil-based polymers (VOBPs) for generating synthetic biomaterials have received greater attention due to their universal accessibility, renewability, intrinsic biodegradability and biocompatibility, as well as low price [88-90]. In comparison with other biopolymers namely carbohydrates and proteins, VOBPs benefits from many impressive characteristics, including: (i) they are not in the form of polymers; however, they have monomer

chains which can be employed to synthesize different polymers such as polyolefin, polyurethane, polyether, and polyester. Hence, the VOBP formulations can be interestingly tuned via converting them to various monomers. (ii) The VOBPs are appropriate to synthesize hydrophobic polymers. They are also compliant for other bio-sources such as carbohydrates and proteins. (iii) The VOBPs are appropriate to generate monomers with such a formulation similar with petroleum-based monomers. Hence, petroleum-based biopolymers can be substituted via the VOBPs with analogous characteristics and properties [88-90].

Regarding biopolymers which can be utilized in bone-like materials, VOBPs can be an interesting candidate. Unlike other renewable biopolymers namely polysaccharides and proteins which have been broadly utilized, the VOBPs have been only used as the appropriate biomaterials for implantation. While by fully investigating the VOBPs, a broad range of invaluable biomaterials and biomimetic material systems can be generated for a variety of engineering applications [88-90].

One of the intriguing plant oil polymers which can be printed at the room temperature is soybean oil epoxidized acrylate (SOEA). This material can be polymerized using UV light by adding bis (2,4,6-trimethylbenzoyl)-phenylphosphineoxide (Ciba Irgacure 819) which is a photoinitiator (see Figure 23) [90].

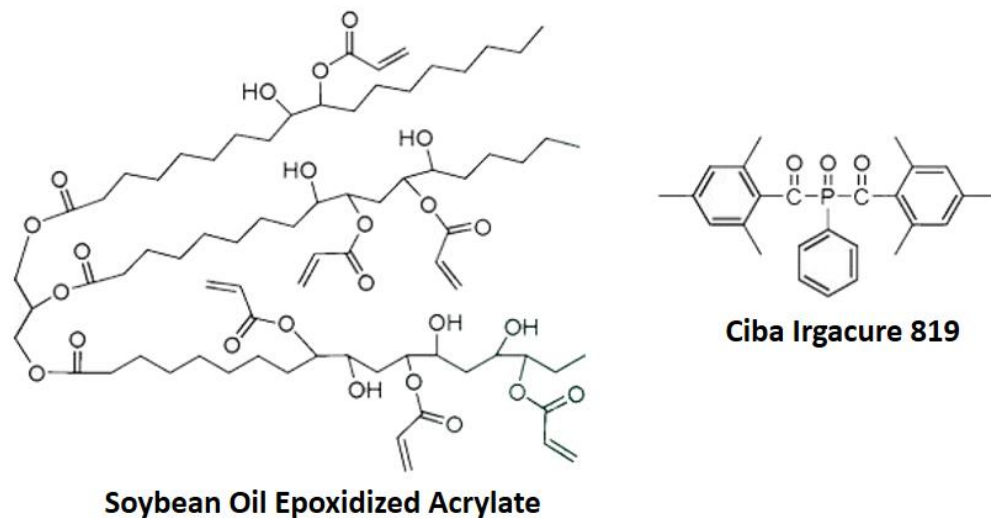


Figure 23. Schematic of soybean oil epoxidized acrylate and Ciba Irgacure 819 [86].

Miao et al.[90] employed the SOEA to generate several bio-polymeric scaffolds using 4D printing and to investigate its cytocompatibility. In order to fabricate bone-mimetic composites, various biocompatible polymers such as gelatine [91, 92], poly-lactic-co-glycolic acid (PLGA) [93], polyetheretherketone (PEEK) [92, 94] have been reinforced using nano-hydroxyapatite (nHA) particles. However, due to nHA scale, dispersion and agglomeration problems, the structure-property relation and generating a staggered structure by means of non-uniformly dispersed aligned nHA in these bone-like materials were not considered. To the best of our knowledge, fabricating a staggered structure using a plant oil polymer especially the SOEA with nHA for bone-mimetic composites has not yet been implemented.

One of the main obstacles to achieving different Si-nHA volume fractions is the high viscosity of plant oil based resins, especially SOEA. To overcome this problem and decrease the viscosity of the resin, Wozniak et al. [95, 96] employed additional monomers such as 2-hydroxyethyl acrylate (HEA) (Sigma Aldrich). Thus, we have proposed two monomers with different viscosity to prepare different Si-nHA volume fraction inks. The first ink composed of Si-nHA/ SOEA and the second

one is Si-nHA/ SOEA+HEA. For the first ink, 10 g Si-nHA was mixed with 30 ml EtOH using ultrasonic homogenizer for 3 min. Also, a solvent mixture of the SOEA and 10 ml EtOH was prepared with the aid of the same homogenizer for 2 min. Before final mixing Si-nHA/EtOH with SOEA/EtOH, the Si-nHA/EtOH mixture was homogenized again for 1 min then added to SOEA/EtOH and the final solvent homogenized for 1 min. Afterward, the container was covered with aluminum foil and located in the fume hood to pass the drying step, and evaporate off the EtOH. During EtOH evaporation and drying, the solvent mixture was homogenized each day for 2 min. For the second ink, again 10 g Si-nHA was mixed with 30 ml EtOH using ultrasonic homogenizer for 3 min. Also, a solvent mixture of 50 vol% SOEA and 50 vol % HEA was prepared and then homogenized with 10 ml EtOH for 2 min. All other steps were done similar to the first ink. These prepared inks could be polymerized using UV light by adding bis (2,4,6-trimethylbenzoyl)-phenylphosphineoxide (Ciba Irgacure 819) (Sigma Aldrich) which is a UV-driven photoinitiator. Therefore, after drying and EtOH evaporation, 1.26% Ciba Irgacure 819 was added to 1% acetone and then homogenized with both prepared inks for 2 min. Eventually, two inks (i.e., Si-nHA/SOEA and Si-nHA/SOEA+HEA) were prepared, and we attempted to make four different Si-nHA volume fractions (10%, 20%, 30%, and 40%). This procedure was developed based on previous studies in the literature [81-96] and also a large number of assessments performed in our research groups. Moreover, Figures 24 (a-b) indicate the weight percentages of *Si* when nanoparticles were mixed with the SOEA as an ink for 3D-printing.

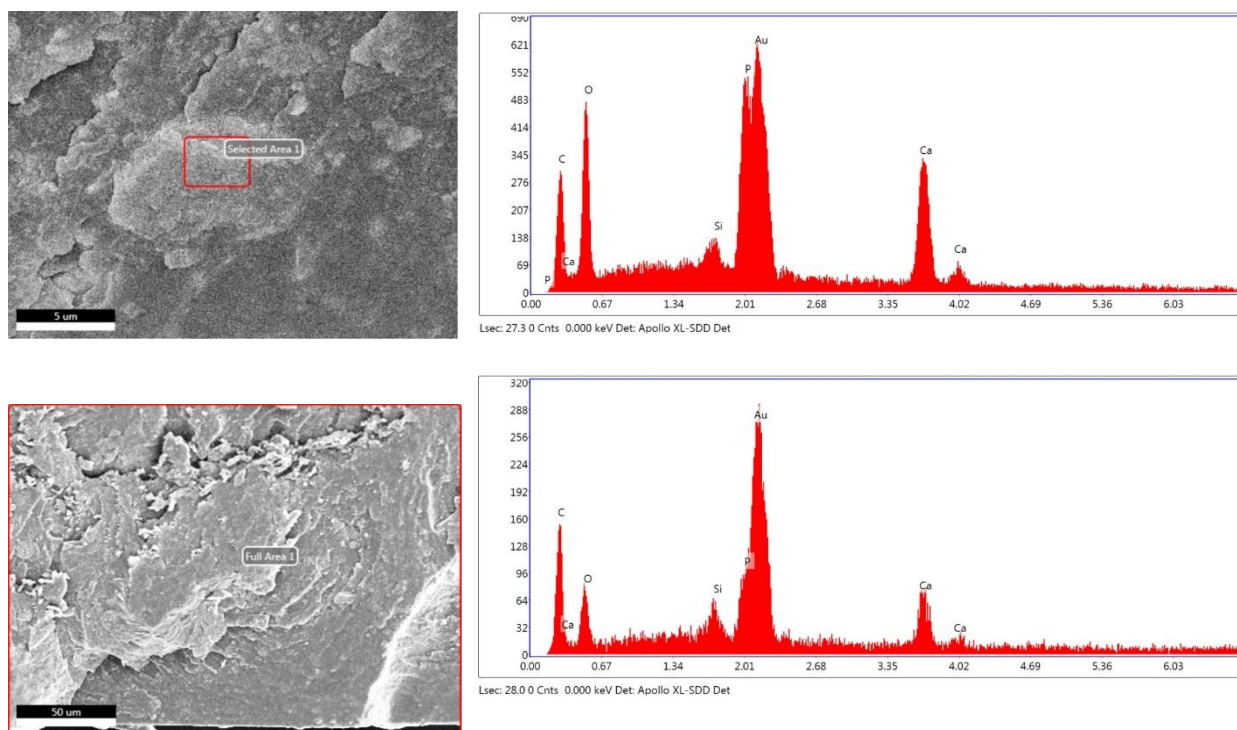


Figure 24. Energy-dispersive X-ray spectroscopy (EDX) results in various regions of Si-nHA/SOEA composition ink.

4.3. Direct Ink Writing (DIW)

In order to produce nanocomposite filaments, an extrusion based 3D-printing method termed direct ink writing (DIW) was used. To tailor mechanical performances of these nanocomposites, non-uniformly dispersed particles in a staggered or aligned structure are required. Therefore, the main goal of this part of experiments is to 3D-print filaments with the highest inclusion volume fraction, good inclusion dispersion and alignment. For this purpose, various parameters were investigated during the 3D-printing process. These parameters include the shape of the nozzle, the diameter of the nozzle tip, 3D-printing speed, and the distance between build plate and the nozzle tip. Indeed,

high shear stress rate in the nozzle tip plays a crucial role in nHA particles alignment. Therefore, two nozzle tip diameters (D_n) (0.26 mm and 0.41 mm) were chosen. Also, by considering the Si-nHA volume fraction, various 3D-printing speeds include 400, 600, 800, and 1000 mm/min were implemented. By decreasing the nozzle tip diameter and increasing 3D-printing speed, shear stress can be significantly boosted. However, for this configuration, optimizing the distance between nozzle tip and build plate is another pivotal parameter for particle alignment. This is executed by changing the distance between build plate and the nozzle tip manually. Figure 25 shows the 3D-printing configuration which contains a tube under piston pressure, taped conical nozzle, as well as UV light pen and its holder.

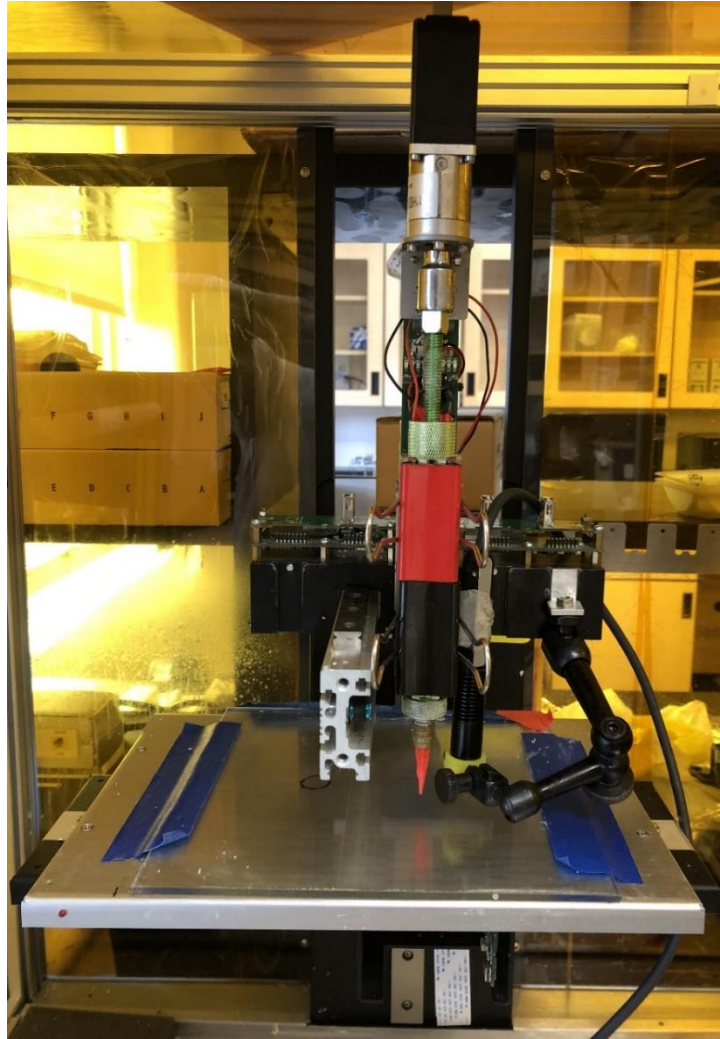


Figure 25. 3D-printing configuration include tube and piston system with taped conical nozzle and UV light pen.

We found that among the nozzles shown in Figure 26, the red conical shape nozzle with $D_n = 0.26$ and 0.41 mm were the best tools for 3D-printing our inks in terms of clogging issue. Note that to filter the UV light penetration in this plastic nozzle; it was completely covered using sticky tapes.



Figure 26. Different nozzle shapes with various materials such as plastic, plastic-metal, and metal.

The influences of all mentioned 3D-printing parameters including different nozzle shape, size, as well as, extrusion speed on the microstructure of nanocomposite filaments were reported in previous studies in the literature [8, 12, 13, 16, 101, 102]. Therefore, the effects of these parameters were assessed in this study using SEM imaging.

In this project, the SEM (Zeiss FESEM 1530) machine with EHT value of 10kV and two types of detector namely SE2 and InLens was employed in the Waterloo Advanced Technology Laboratory (WATLab). Figure 27 shows the SEM images for the cross-section of a 3D-printed filament with ~20% Si-nHA volume fraction. The Si-nHA particles without solving in EtOH were simply mixed with the SOEA using ultrasonic homogenizer. Clusters and the agglomeration of Si-nHA particles can be seen in this Figure easily. On the other hand, Figure 28 illustrates Si-nHA particles which were added to EtOH before mixing with the SOEA+ EtOH. Not only an excellent non-uniformly dispersion but also, a proper Si-nHA particle alignments and their circular cross-section can be seen in this Figure. In order to achieve particle alignment, by increasing volume fraction, 3D-

printing speed should be increased significantly. For instance, Figure 28 indicates ~20% Si-nHA filament which was 3D-printed using a 0.26 mm nozzle tip diameter (D_n) and 1000 mm/min speed.

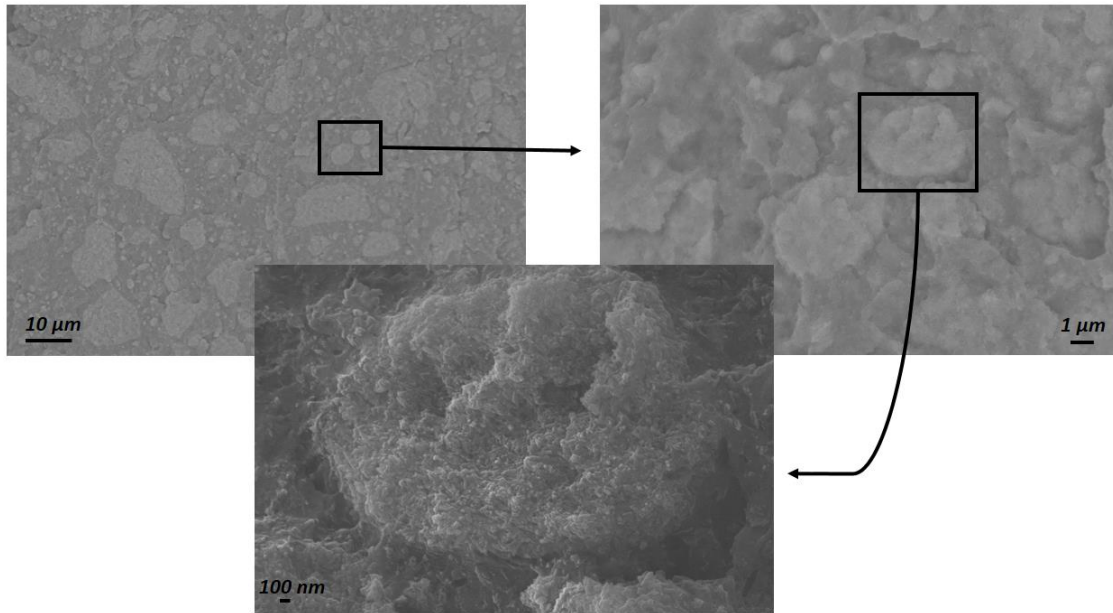


Figure 27. SEM images for the cross-section of a 3D-printed Si-nHA/SOEA filament (20% Si-nAH volume fraction), while Si-nHA particles did not solve in EtOH.

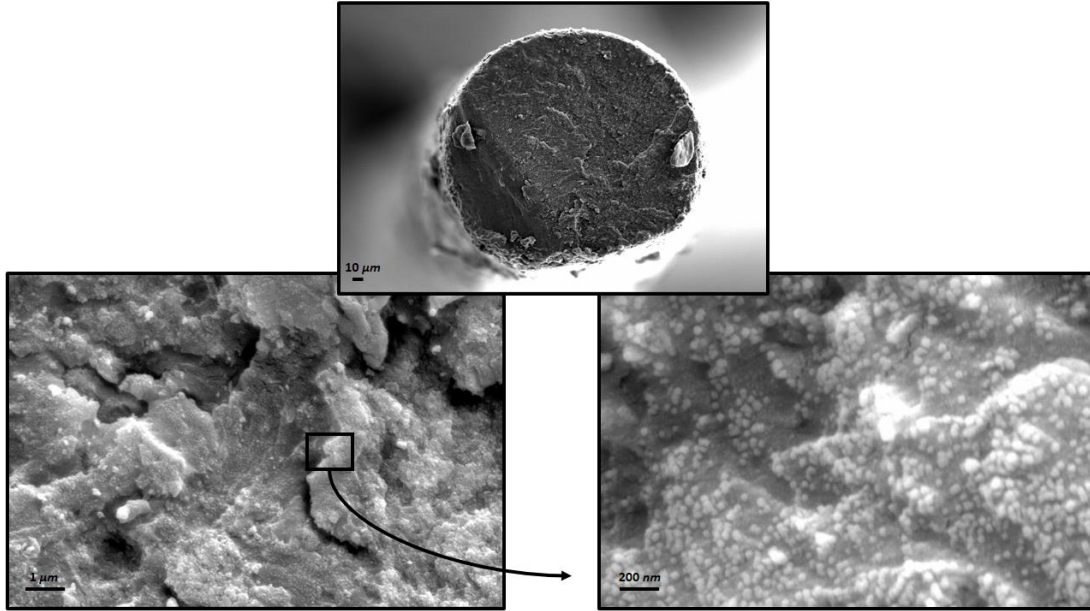


Figure 28. SEM images for the cross-section of a 3D-printed Si-nHA/SOEA filament (20% Si-nHA volume fraction), while Si-nHA particles solved in EtOH.

In summary, the main filaments in this study were 3D-printed at 1000 mm/min speed using conical shape nozzle with $D_n = 0.26$ and 0.41 mm. Note that the stand-off distance and chosen UV light dose were a function of Si-nHA volume fractions.

4.4. 3D-printed filament Characterizations

A number of thermogravimetric analyses (TGA) were done on the cured 3D-printed filament to determine the real volume fraction of each batch. Three samples of each batch and ink were analyzed via TGA to check the repeatability of samples and data. As a test procedure, each sample was equilibrated at 30 °C, and then the temperature was increased up to 800 °C with 10 °C heating rate. Figures 29 (a-b) demonstrate the thermal decomposition and weight loss (%) of each ink batch versus temperature (°C) obtained using TGA. As mentioned, the initial goal for the value of Si-nHA volume fractions were 10%, 20%, 30%, and 40%. However, for the Si-nHA/SOEA ink, we

achieved ~9.40%, ~19.28%, ~24.84%, and ~29.37%. Also, for Si-nHA/SOEA+HEA ink we obtained ~6.46%, ~17.57%, ~24.33%, and ~27.23%. As it can be seen, by increasing Si-nHA volume fraction the discrepancy between our initial assumption and reality tends to be increased for each nanocomposite ink. In Si-nHA/SOEA ink for 10% and 20% Si-nHA we have negligible differences between our initial goal and final real volume fraction; while, in Si-nHA/SOEA+HEA none of them are not remarkably close to our initial assumption. It can imply that by adding HEA the behavior of Si-nHA particles changed or they tend to be settled; thus, lower Si-nHA volume fractions were achieved in the cured 3D-printed filaments. Furthermore, by adding different volume fractions of Si-nHA to both matrices (i.e., SOEA and SOEA+HEA) the thermal decomposition point or mass loss (%) obviously tends to be shifted; however, this deference in Si-nHA/SOEA+HEA is greater than Si-nHA/SOEA ink. Ethanol during the preparation of these inks was dried and evaporated in the fume hood; however, a precise drying control was not done due to the fact that the objectives of this project were not assessing bio- and cytocompatibility nor damage behavior.

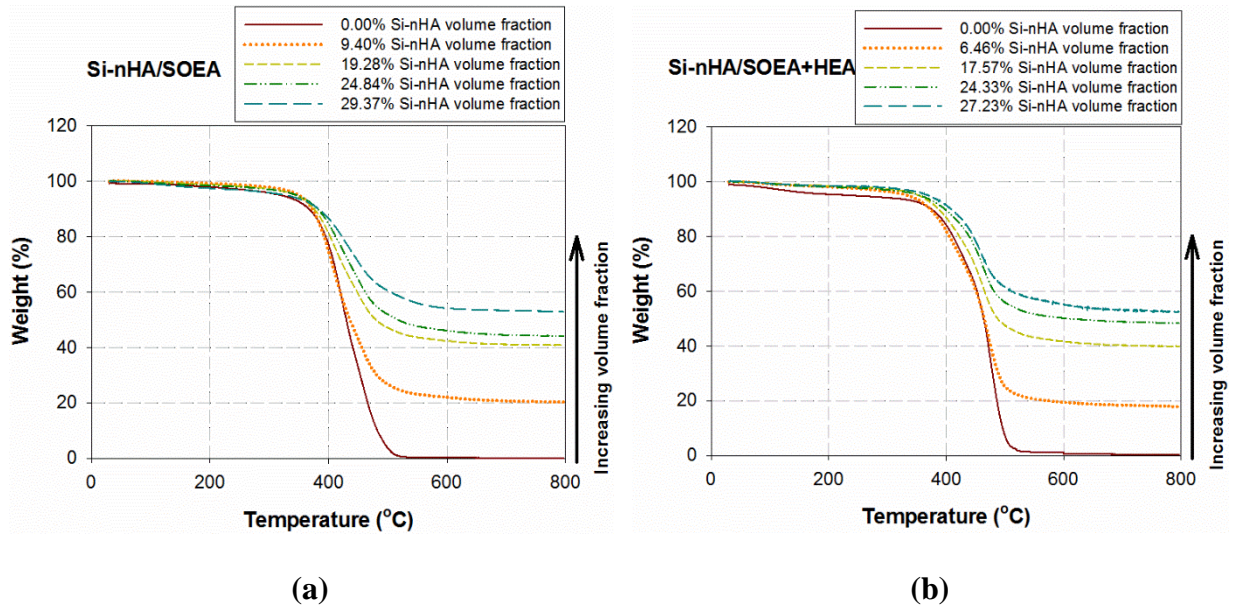
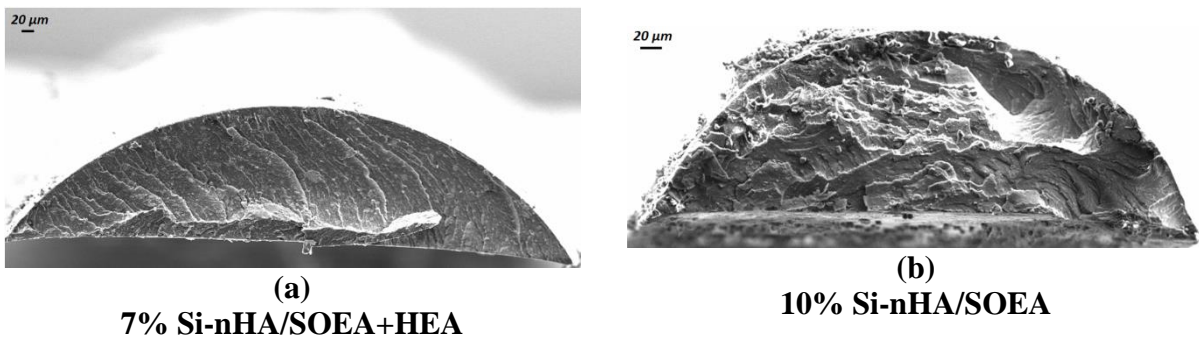
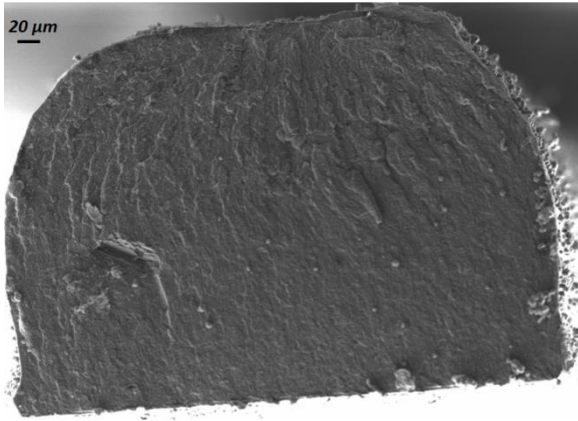


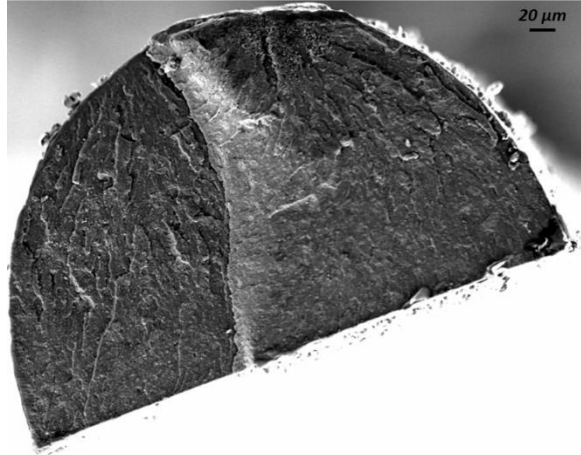
Figure 29. Thermogravimetric analyses (TGA) for both inks and different volume fractions. (a) Si-nHA/SOEA ink and (b) Si-nHA/SOEA+HEA ink.

As mentioned, by adding HEA to SOEA and Si-nHA to both matrices (i.e., SOEA and SOEA+HEA), the viscosity tends to be decreased and increased respectively. In order to assess the influences of different viscosity on the shape of 3D-printed nanocomposite filaments, nanoparticle dispersions, and alignments a number scanning electron microscope (SEM) images were captured. Figures 30 (a-h) demonstrate the filament cross-sections of Si-nHA/SOEA and Si-nHA/SOEA+HEA inks for different Si-nHA volume fractions.

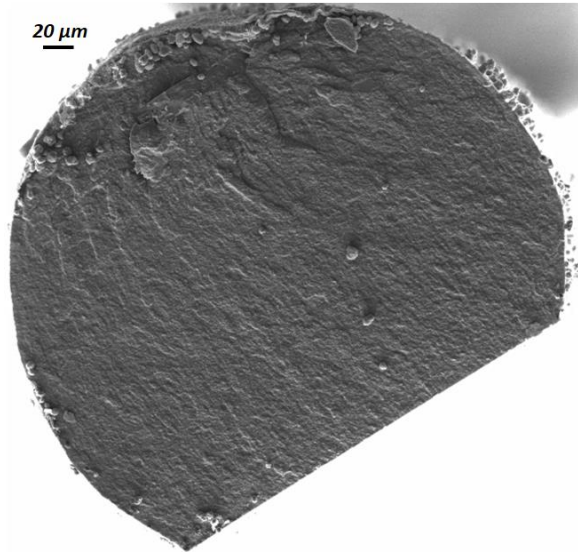




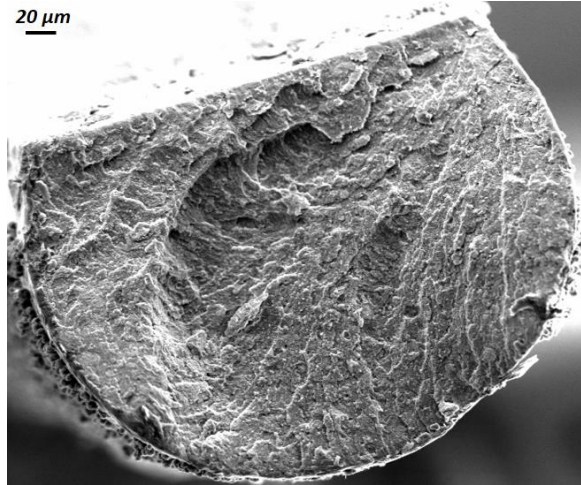
(c)
17% Si-nHA/SOEA+HEA



(d)
20% Si-nHA/SOEA



(e)
25% Si-nHA/SOEA+HEA



(f)
25% Si-nHA/SOEA

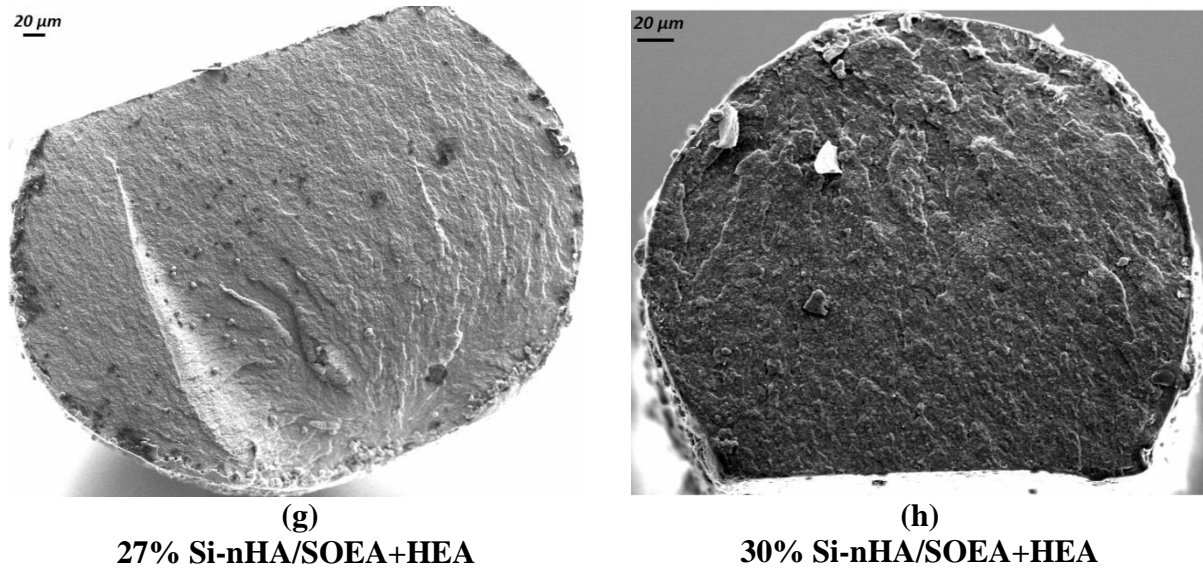


Figure 30. 3D-printed filaments cross-sections of Si-nHA/SOEA and Si-nHA/SOEA+HEA nanocomposite inks for various Si-nHA volume fractions.

As it can be seen, by increasing Si-nHA volume fraction the viscosity of nanocomposite ink tends to be increased; thus, 3D-printed nanocomposite filament has enough time to be cured without significant changes due to the ink flow behavior. Obviously, in 10% volume fraction for both inks a semi-circular cross-section can be seen because of flow behavior and low viscosity of the nanocomposite ink. Even in higher volume fraction of Si-nHA/SOEA+HEA ink this flow behavior is more than other Si-nHA/SOEA ink because HEA remarkably decrease the viscosity of ink. It can be noted that for both size of nozzle tip same results were observed. In effect, one side flat surface on nanocomposite filaments has an effective role and considerably useful for 2D DIC measurements.

Figure 31 shows three different regions of nanocomposite filament cross-section wherein SEM images were captured to assess the Si-nHA particle dispersions and alignments. Figure 32 illustrates the dispersions and alignment of 7% Si-nHA/SOEA+HEA in different regions presented

in Figure 31. As it can be seen in all three regions, less than 1 μm clusters with good dispersions have developed. However, in the zoomed view, the round shape of nanoparticles cross-section can be observed. In effect, there are microscopic distances among nanoparticles in many of these clusters which can imply that they are not fully agglomerated.

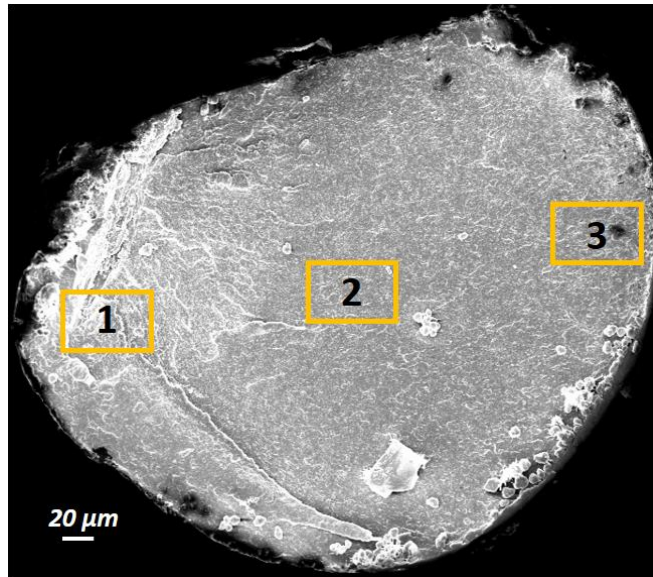


Figure 31. Three various regions on 3D-printed filament cross-section for SEM imaging.

7% Si-nHA/SOEA+HEA	
Region 1	

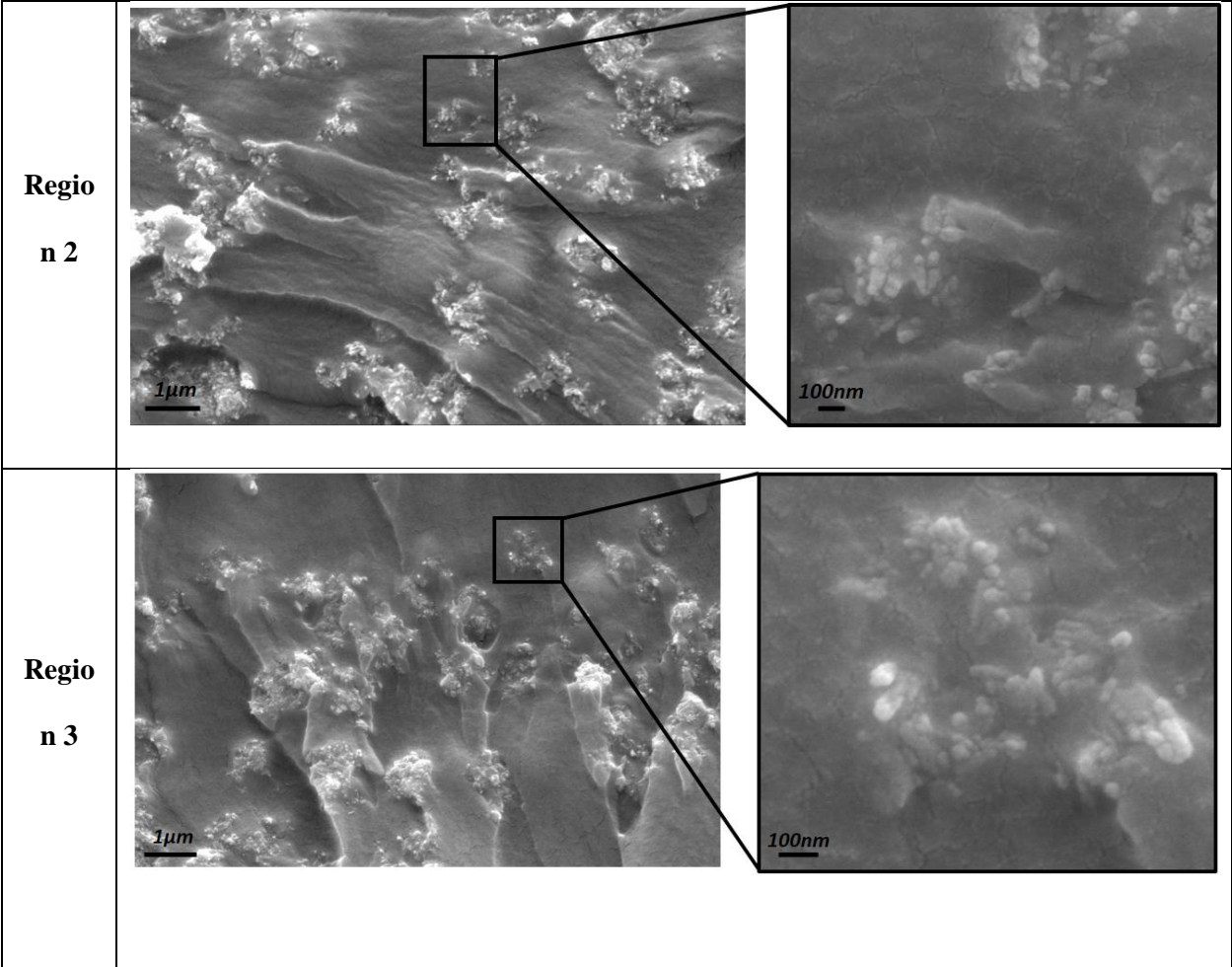


Figure 32. Si-nHA nanoparticle dispersions and alignments of two different magnifications for 3D-printed 7% Si-nHA/SOEA+HEA filament.

Figure 33 demonstrate dispersions and alignments of nanoparticles in 17% Si-nHA/SOEA+HEA. There is not any cluster and all nanoparticles, particularly in region 1 and 3, are perfectly aligned. These regions are close to the outer surfaces of filament; however, in region 1 which is in the middle of filament, relatively aligned and misaligned nanoparticles can be observed.

	17% Si-nHA/SOEA+HEA
--	----------------------------

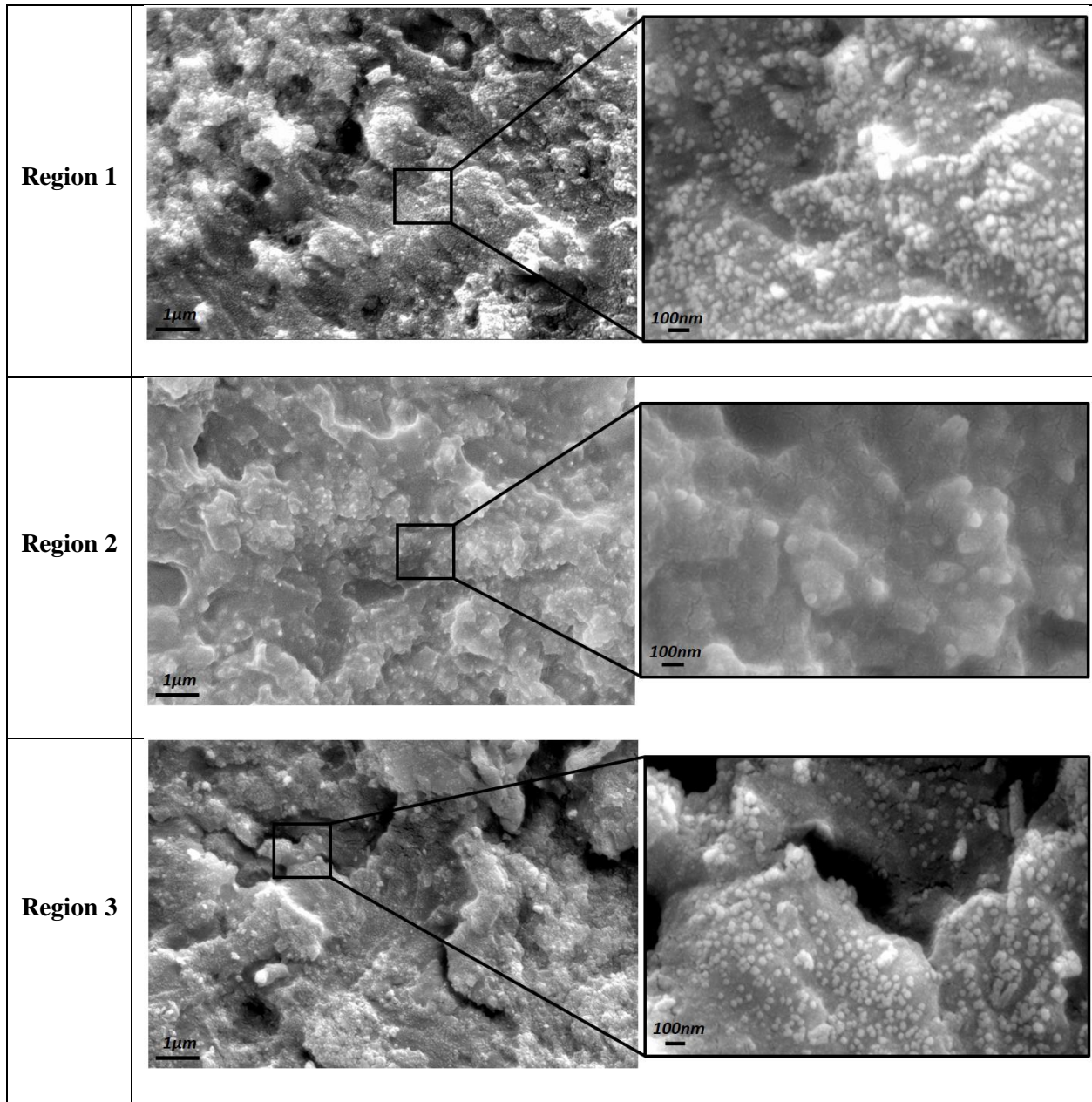


Figure 33. Si-nHA nanoparticle dispersions and alignments of two different magnifications for 3D-printed 17% Si-nHA/SOEA+HEA filament.

Figure 34 shows nanoparticle distributions and alignments for 25% Si-nHA/SOEA+HEA ink. As it can be seen by increasing volume fraction, nanoparticles are more compressed in comparison with lower volume fractions (i.e., Figures 32 and 33). Same as 17% Si-nHA/SOEA+HEA ink, in

regions near to outer surfaces (i.e., region 1 and 3) better alignments and distributions can be observed.

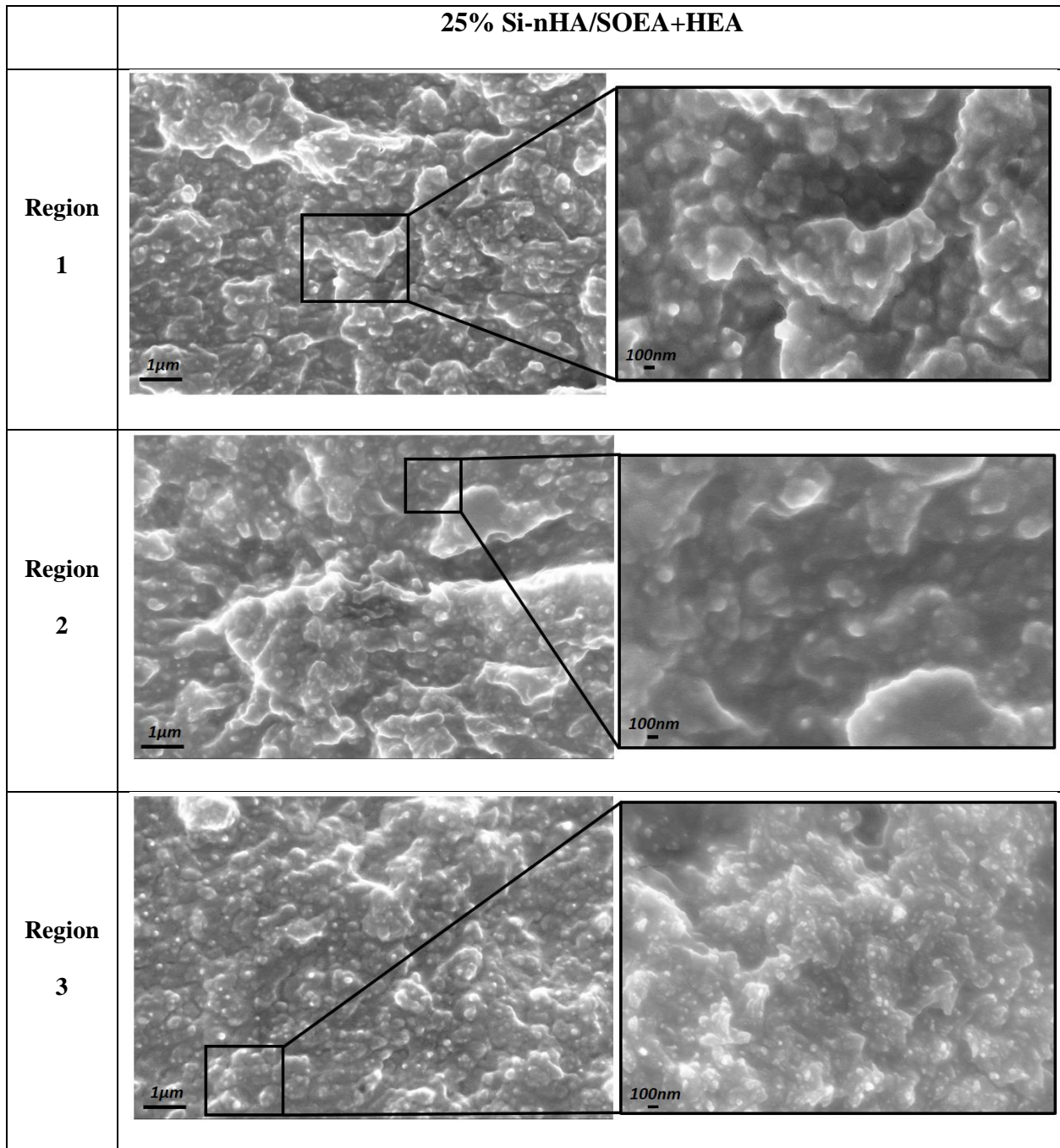
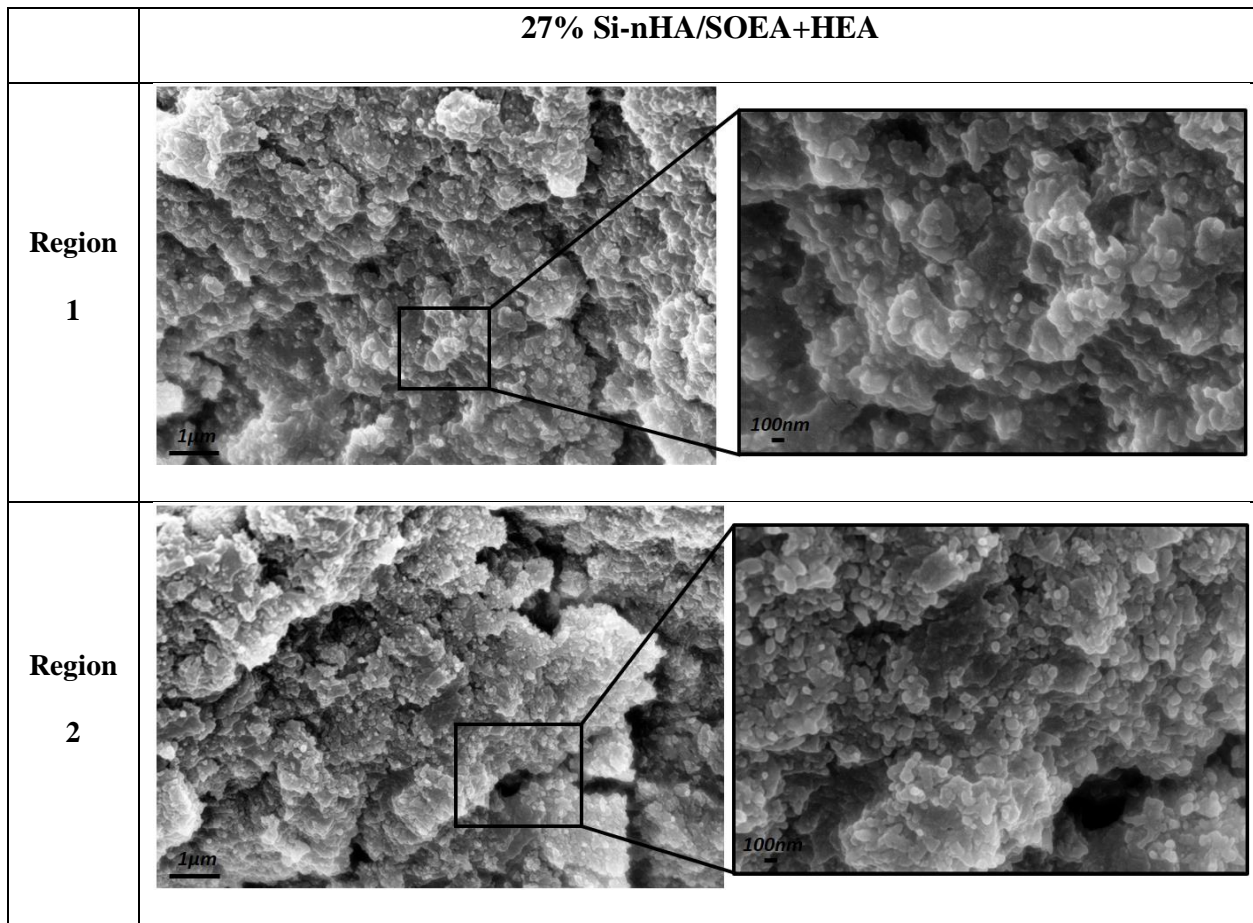


Figure 34. Si-nHA nanoparticle dispersions and alignments of two different magnifications for 3D-printed 25% Si-nHA/SOEA+HEA filament.

Figure 35 indicate good alignments and dispersions in 27% Si-nHA/SOEA+HEA ink. Similar to previous two inks, this ink also has better alignments and distributions in the outer surfaces of filament compared to the middle. It can be easily seen, by increasing nanoparticle volume fraction, nanoparticles are fully compressed especially in the middle of filament which can cause on increasing misalignments.



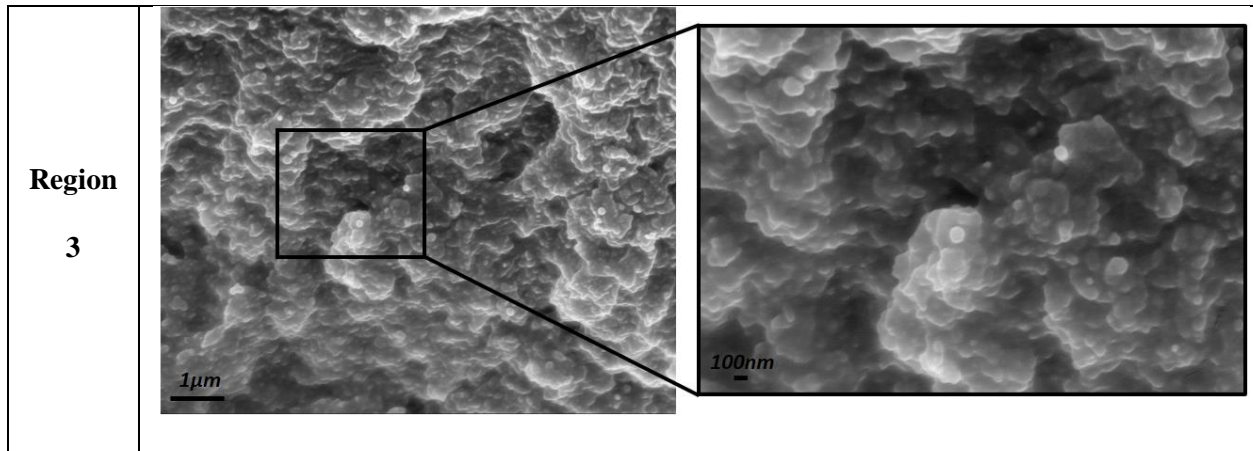


Figure 35. Si-nHA nanoparticle dispersions and alignments of two different magnifications for 3D-printed 27% Si-nHA/SOEA+HEA filament.

Figure 36 illustrates the dispersions and alignments of nanoparticles for 10% Si-nHA/SOEA ink. On the one hand, a large number of clusters with the size of less than 1 μm can be seen in the middle of filament (i.e., region 1) which are entirely agglomerated. On the other hand, in the sides of filament (i.e., region 1 and 3) there are several small clusters with microscopic distances among nanoparticles which are aligned and not agglomerated. It can be noted that similar morphologies were observed in 7% Si-nHA/SOEA+HEA with this difference that 7% Si-nHA/SOEA+HEA in benefits from better dispersions and alignments in the middle of filament.

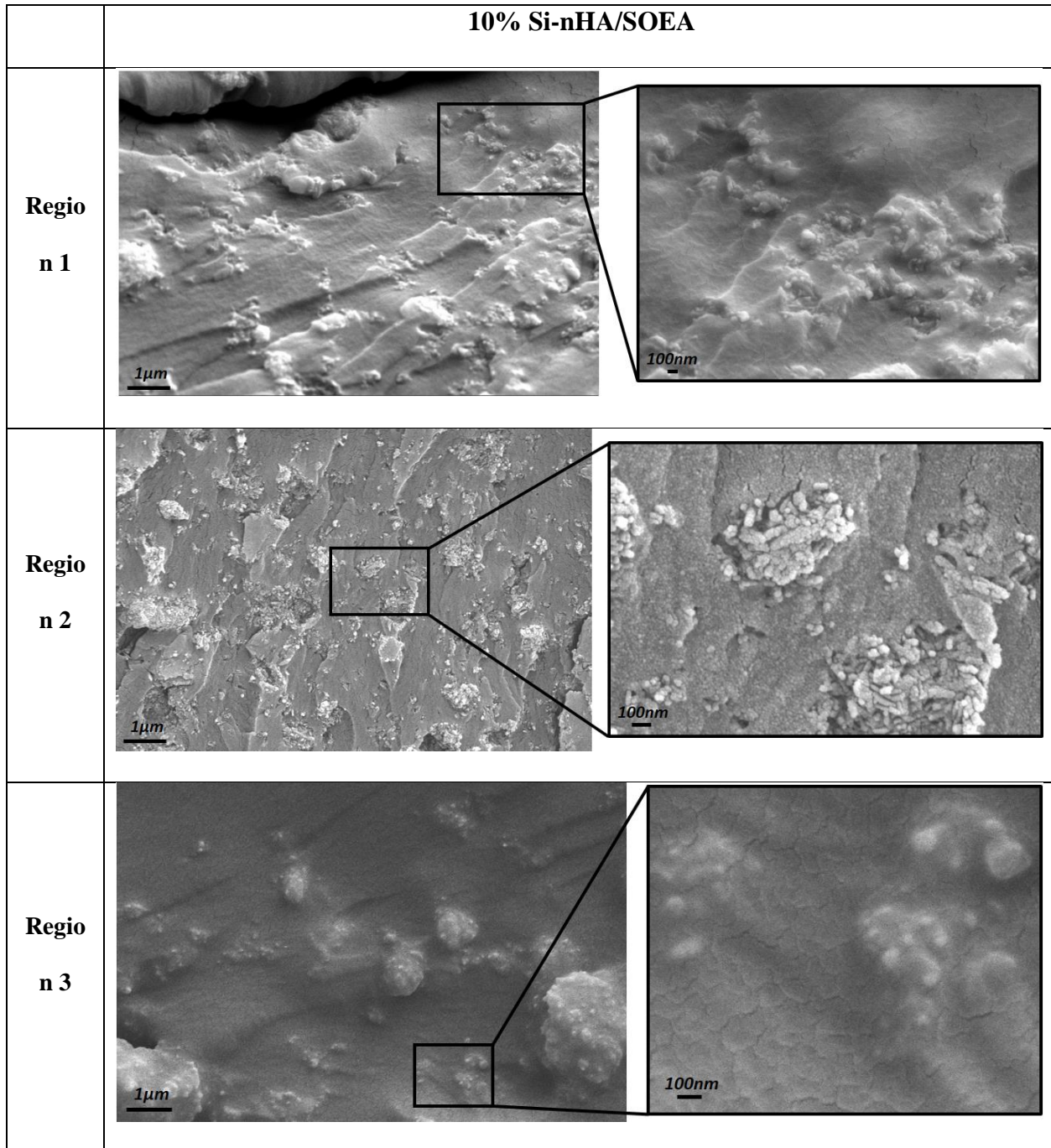
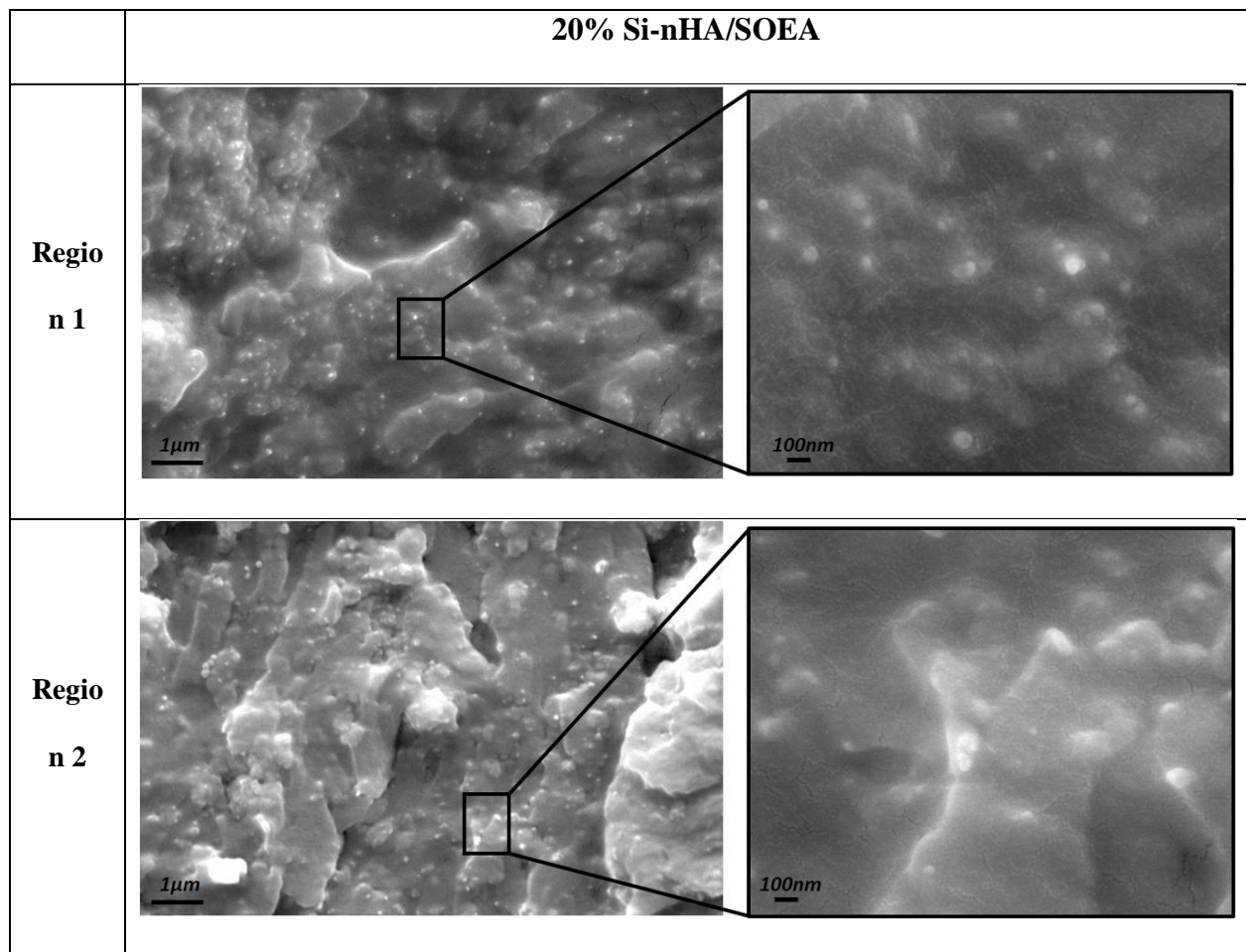


Figure 36. Si-nHA nanoparticle dispersions and alignments of two different magnifications for 3D-printed 10% Si-nHA/SOEA filament.

Figure 37 shows nanoparticle dispersions and alignments for 20% Si-nHA/SOEA ink. Again several small clusters can be seen in region 1; however, the nanoparticles are relatively aligned. In

the outer surfaces (i.e., region 1 and 3) better nanoparticle distributions and alignments can be observed. In the comparison of this ink with 17% Si-nHA/SOEA+HEA ink which has approximately same nanoparticle volume fraction, 17% Si-nHA/SOEA+HEA ink benefits from superior nanoparticle dispersions and alignments which can come back to its lower viscosity due to adding HEA.



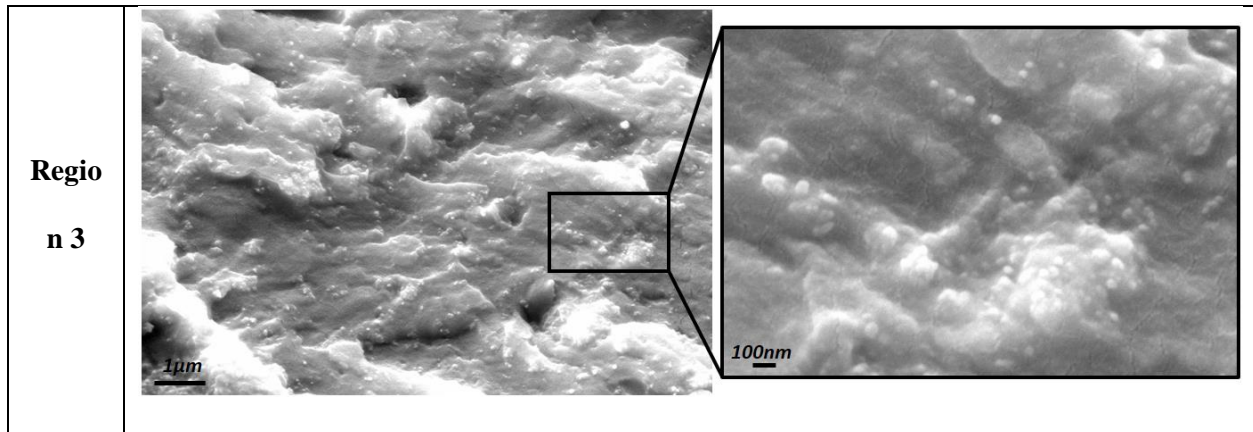
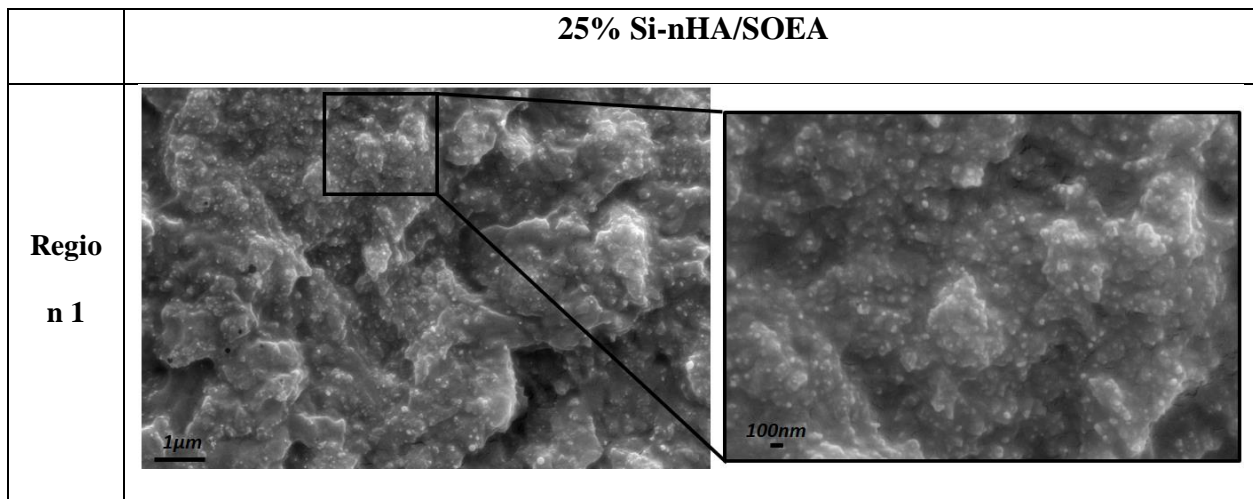


Figure 37. Si-nHA nanoparticle dispersions and alignments of two different magnifications for 3D-printed 20% Si-nHA/SOEA filament.

Figure 38 illustrates nanoparticle distributions and alignment for 25% Si-nHA/SOEA ink. On one hand, interesting nanoparticle alignments and dispersions can be seen in siding surfaces (i.e., region 1 and 3). On the other hand, misaligned and agglomerated nanoparticle can be observed in the middle of filament (i.e., region 2). The difference between this ink with 25% Si-nHA/SOEA+HEA ink is that in region 2 there were nanoparticle dispersions and alignment, but here, there are a number of misaligned and agglomerated nanoparticles with improper distributions. This is a result of high viscosity of the SOEA causing nanoparticles to inefficiently run within this ink.



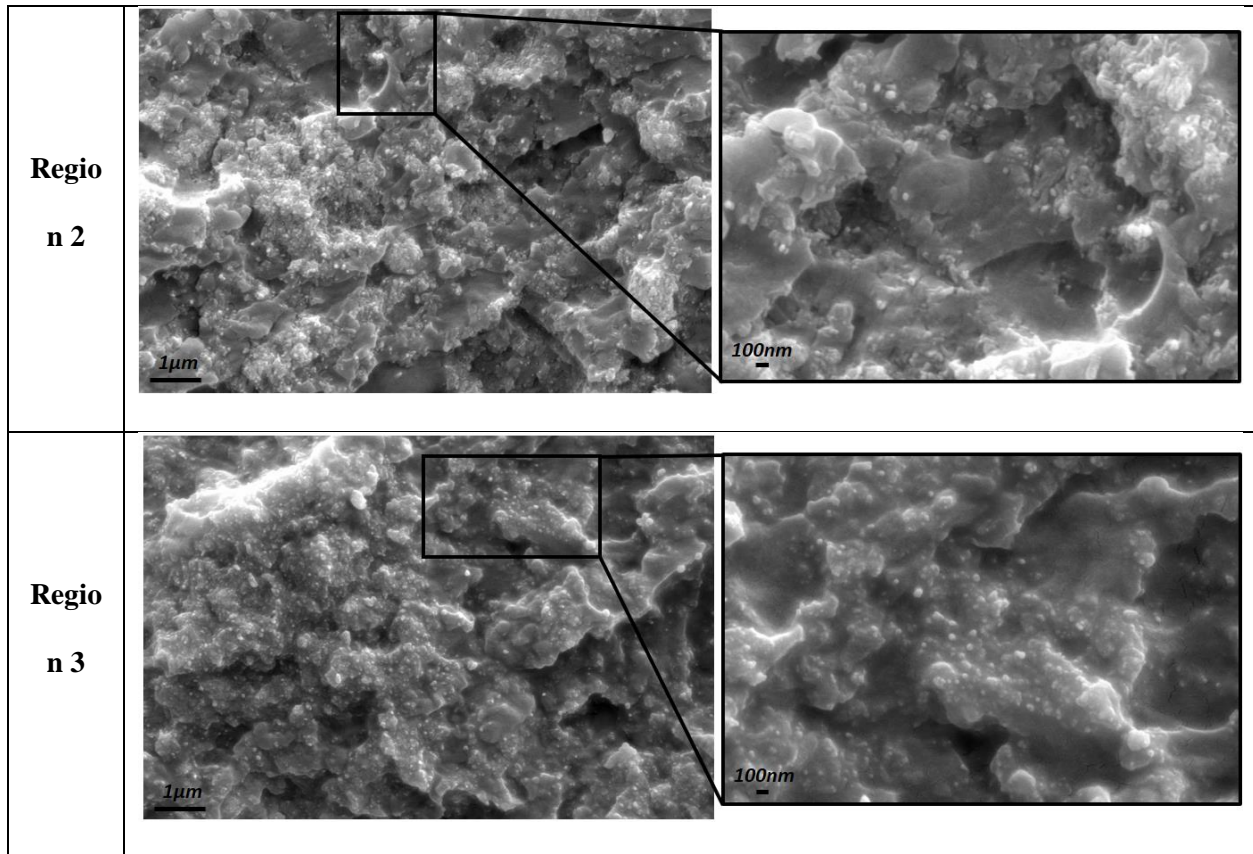


Figure 38. Si-nHA nanoparticle dispersions and alignments of two different magnifications for 3D-printed 25% Si-nHA/SOEA filament.

Figure 39 demonstrates compressed nanoparticles in the region 2 of 30% Si-nHA/SOEA ink. In contrast to regions 1 and 3, nanoparticles are misaligned and agglomerated in this region. Both inks (i.e., 30%Si-nHA/SOEA and 27% Si-nHA/SOEA+HEA) have same morphologies in the middle of filament with this deference that 27% Si-nHA/SOEA+HEA notably benefits from better dispersions and alignments as well as with smaller clusters.

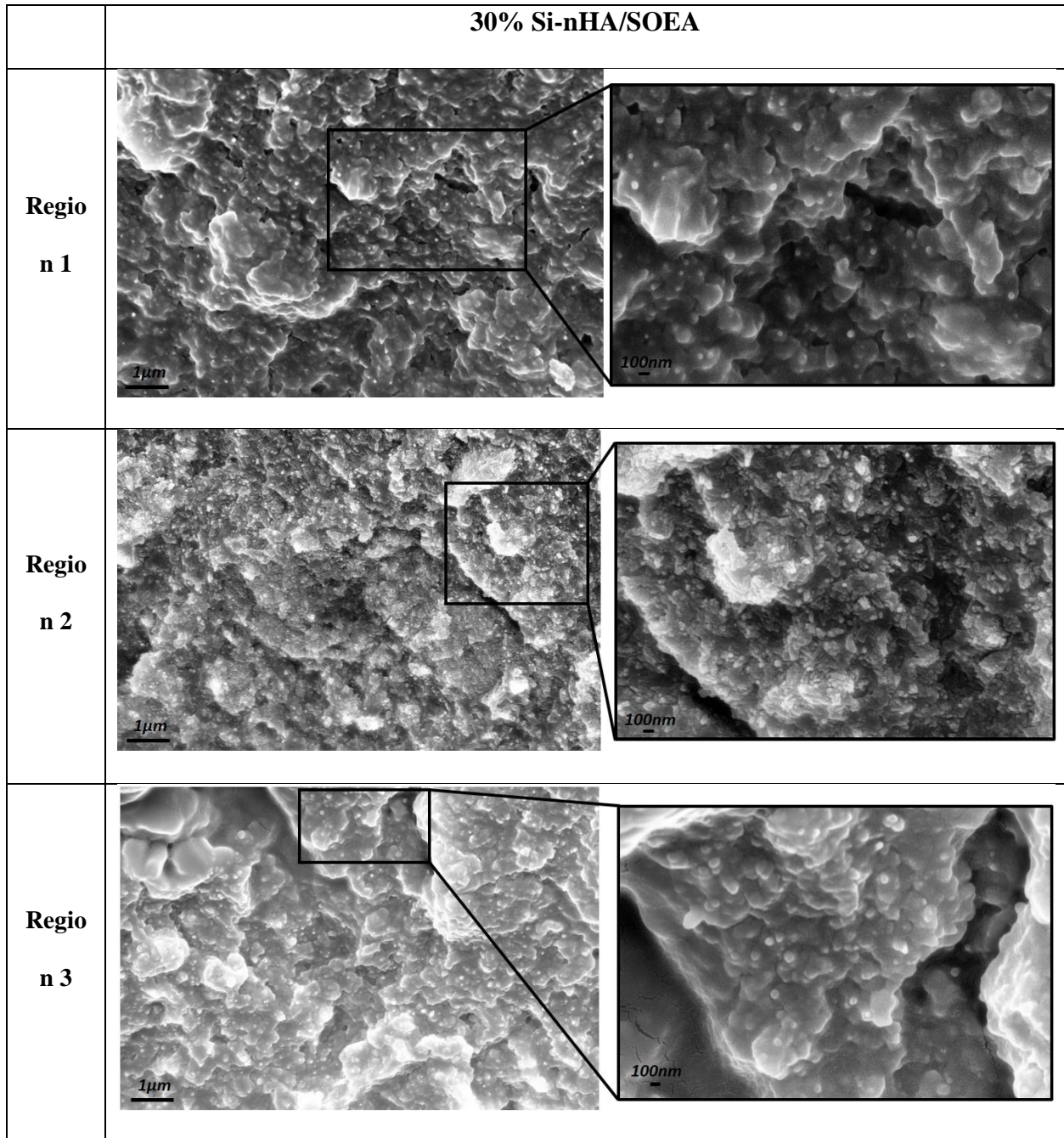


Figure 39. Si-nHA nanoparticle dispersions and alignments of two different magnifications for 3D-printed 30% Si-nHA/SOEA filament.

It is worth mentioning that generated microstructure using both nozzle tip sizes were identical. However, there should be some differences between material microstructures which are 3D-

printed with two nozzle tip sizes. These differences in these experiments were trivial and they could not be captured using SEM images and analyses.

Figure 40 shows the difference between size and contrast of Si-nHA and coated gold particles on the surface of filaments cross-sections. Consequently, in the captured SEM images, Si-nHA particles were easily observed and detected in 100 nm scale.

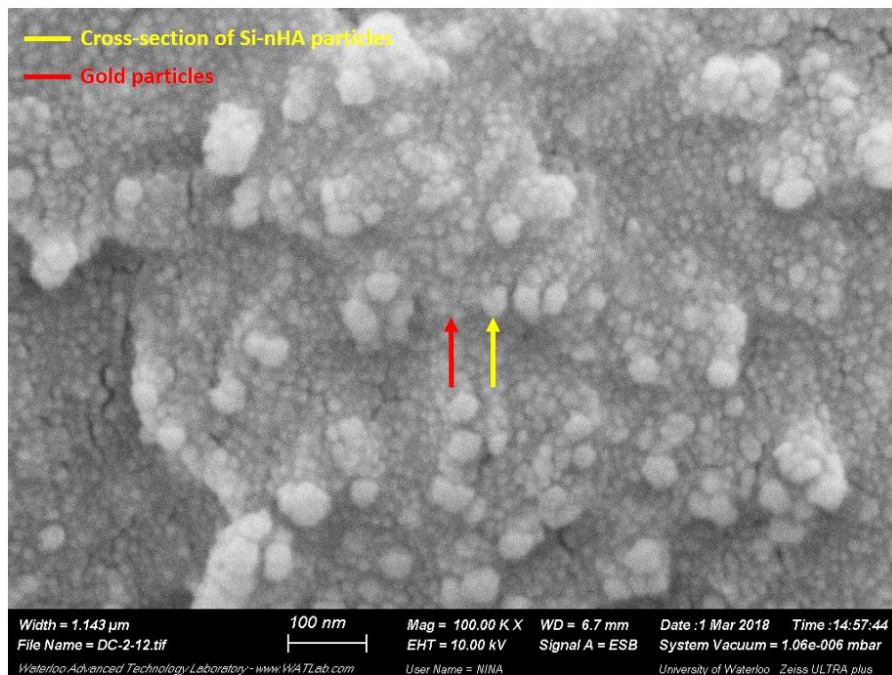


Figure 40. Si-nHA and coated gold particle sizes and contrast in SEM images.

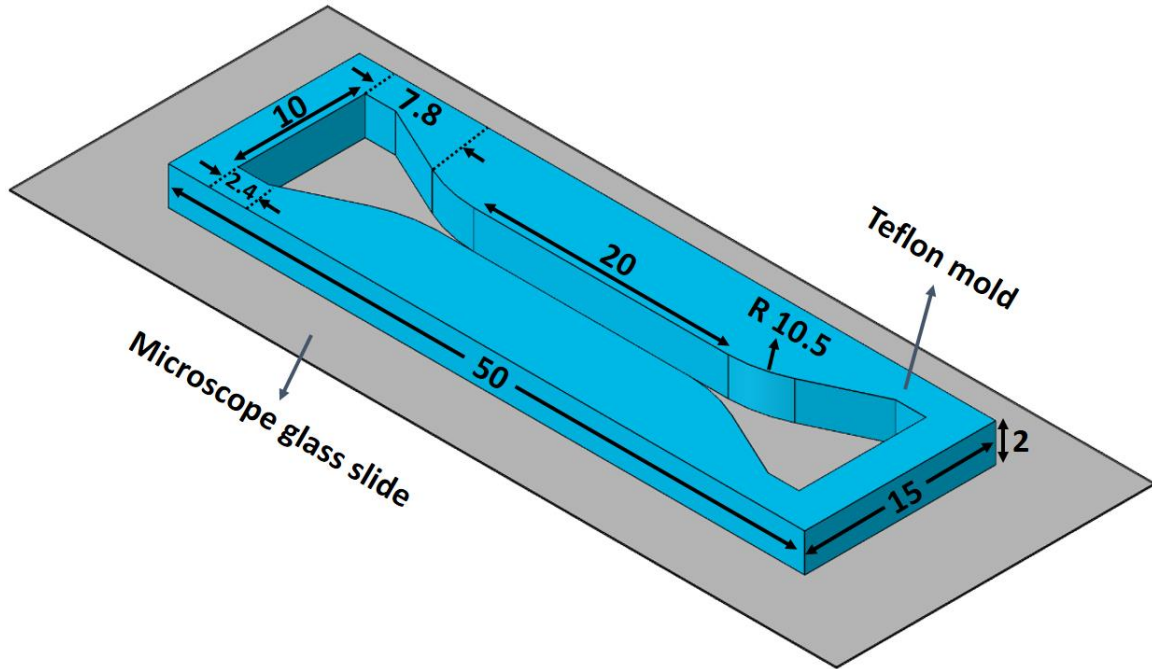
Chapter 5: Mechanical testing methods

In this chapter, the mechanical test specimen preparations for both biopolymers and 3D-printed nanocomposite filaments are explained. Afterwards, the tensile test and DIC procedures are described.

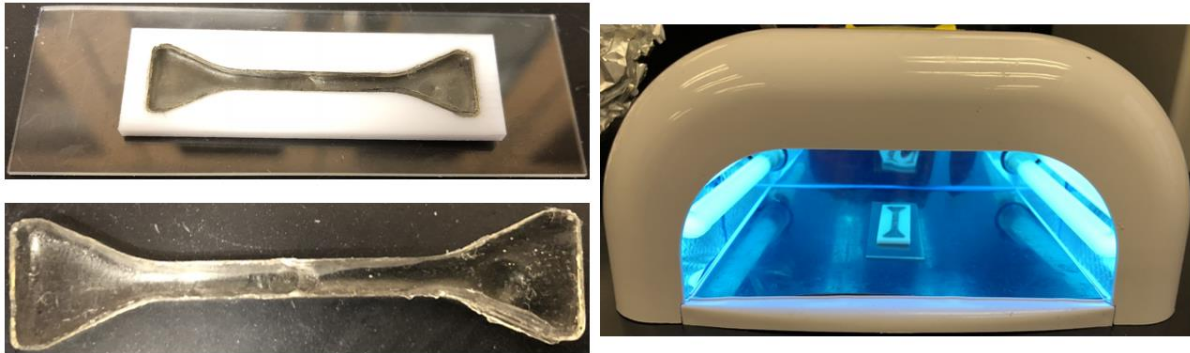
5.1. Specimen Preparation for Biopolymer Resin Mechanical Tests

Mechanical tests on SOEA and SOEA+HEA specimens were performed to define their mechanical properties for the FE micromechanical models, for comparing their respective mechanical properties, and to study the influence of UV light cure dose. A Teflon mold depicted in Figure 41 was used for fabrication of the test specimens in a UV light curing nail box.

For the purpose of preparing both biopolymers dog-bone specimens, first, 1.26% Ciba Irgacure 819 was added to 1% acetone and then homogenized with the SOEA using ultrasonic homogenizer for 2 min. Also, the same amount of Ciba Irgacure 819 and Acetone was homogenized for 2 min with 50% solvent of SOEA+HEA. After the drying and acetone evaporation process, to reduce the air bubbles, both monomer solvents (i.e., SOEA and SOEA+HEA) were kept in a water bath at ~40 °C for at least 1 hr. Afterward, a microscope glass slide was glued on the one side of the mold and then using a syringe both monomers were poured in the molds and cured in the UV light curing nail box (see Figure 41 (a-b))



(a)



(b)

Figure 41. Prepared biopolymeric dog-bone using Teflon mold with one-side microscope glass slide and UV light curing nail box.

In order to assess UV light cure dose, six different UV light cure doses include 1.8, 3.6, 7.2, 14.4, 28.8, and 57.6 J/cm² were implemented in the UV light curing nail box. To ensure about uniform UV light radiation, both sides of the specimen in the mold were equally radiated. The elastic properties of each set are reported in Section 6.2.

5.2. Filament Test Specimens Preparation

Conducting uniaxial tensile test on 3D-printed filaments is challenging due to the limitation of fixtures and testing machines in this small scale. First, a large number of trapezoidal parts similar to the head of the dog-bone specimen were 3D-printed using polylactic acid on a Lulzbot Mini 3D Printer. In order to fix filaments, these trapezoidal parts were designed with cylindrically shaped indent, as seen in Figure 42. Second, each filament was taped on a thin plastic sheet, and then the trapezoidal part was glued on each head of the filament using superglue. To make specimens rigid and stable, another trapezoidal part was glued to the other side of each filament head. This process was a little time consuming because the full curing time of superglue was 24 h. Figure 42 depicts the filament test configuration and preparation process.

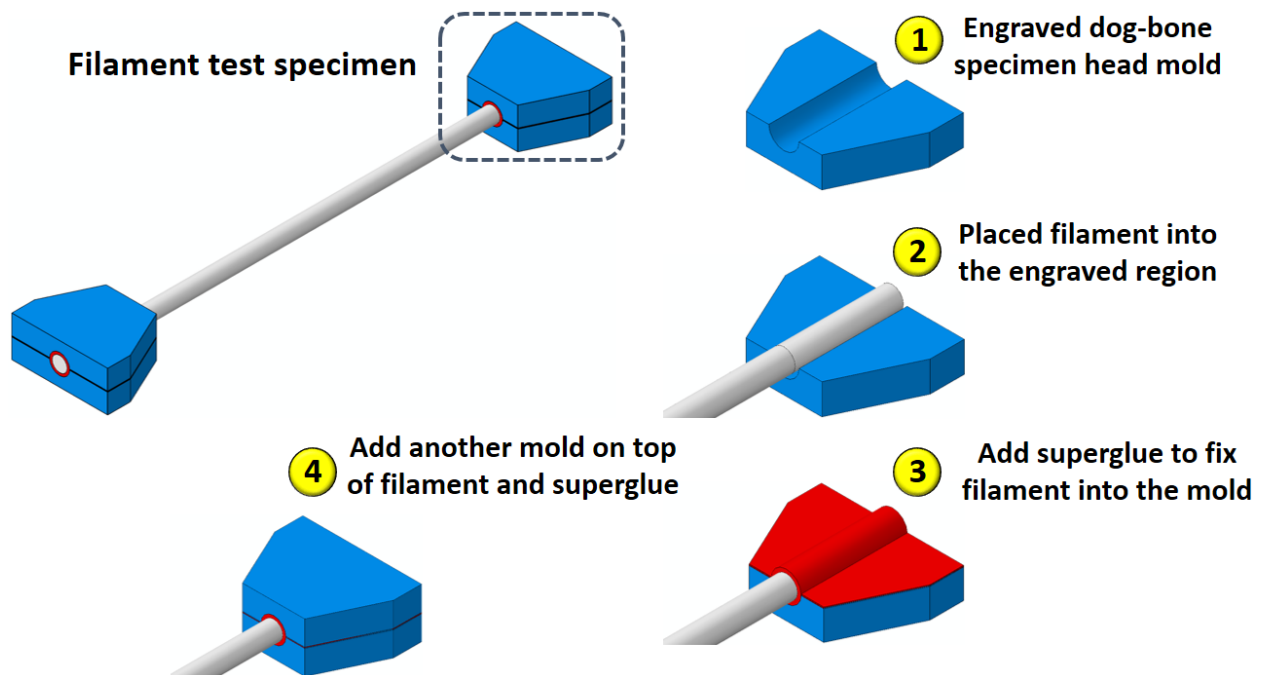


Figure 42. Nanocomposite filament test specimen configuration.

5.3. Micro-mechanical and Micro-DIC Measurements

Various mechanical tests on biopolymers dog-bone specimens and nanocomposite filaments were conducted using a small universal testing machine (Psylotech μ TS) integrated with an optical microscope (Olympus) to enable 2D digital image correlation (DIC) (see Figure 43). The commercial VIC-2D software package (Correlated Solutions Inc.) was used to measure engineering strains. The resolution 5X lens of Olympus microscope was ~ 0.000688 mm/pixel. DIC was run at the rate of 5 frames per second with the subset size of 29 pixels, the step size of 7, and the strain filter of 15 pixels. The strains were measured using three different extensometers in the rectangular region of interest which is illustrated in Figures 44 and 45.

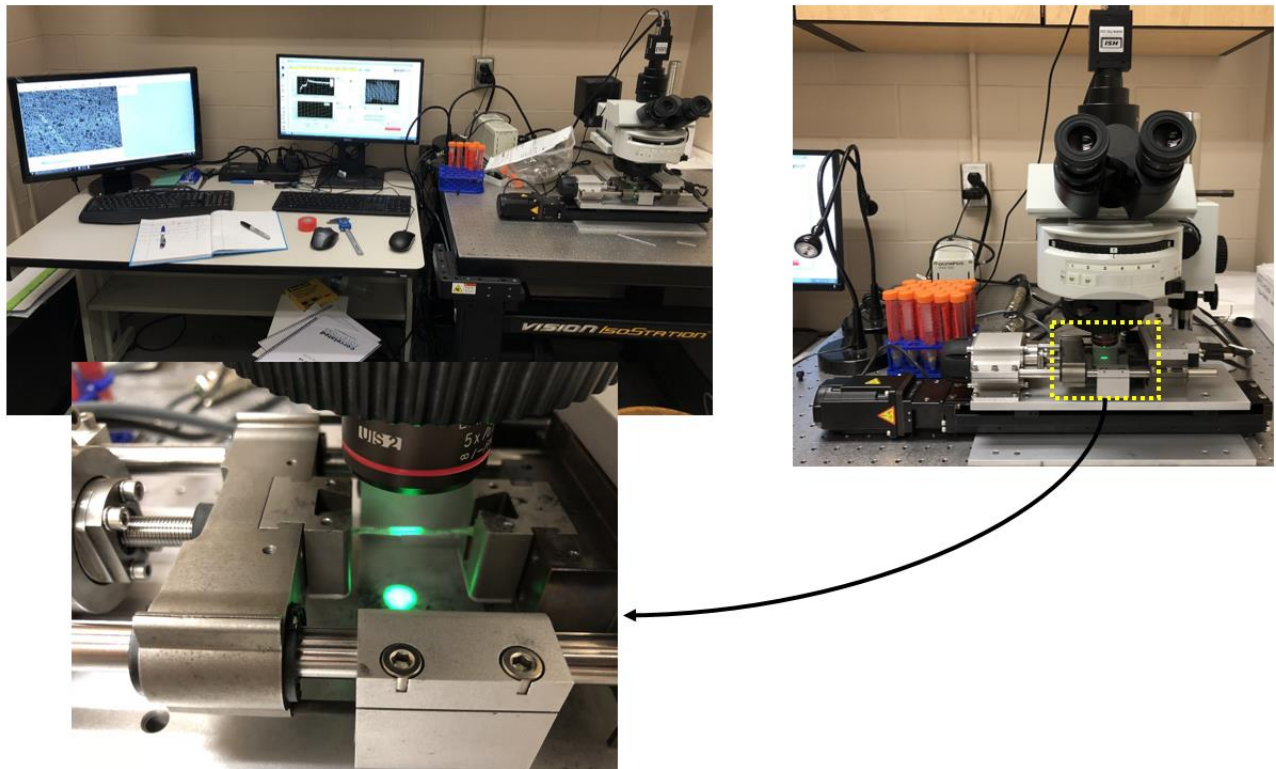


Figure 43. Small-scale universal and -2D DIC (microscope) test configuration.

At this scale, executing DIC can be challenging especially in terms of speckling. Since the 5X lens of the microscope was employed for DIC, the diameter of each speckle should be approximately 5 pixels. In order to have this small size of speckles, high-resolution printer toner powder was employed by means of an atomizer powder blower. The diameter of each particle of this powder is approximately 5-6 μm which very suitable for 2D DIC using 5X lens microscope. Figure 44 and 45, illustrate speckle patterns on biopolymer dog-bone and nanocomposite filament specimens respectively.

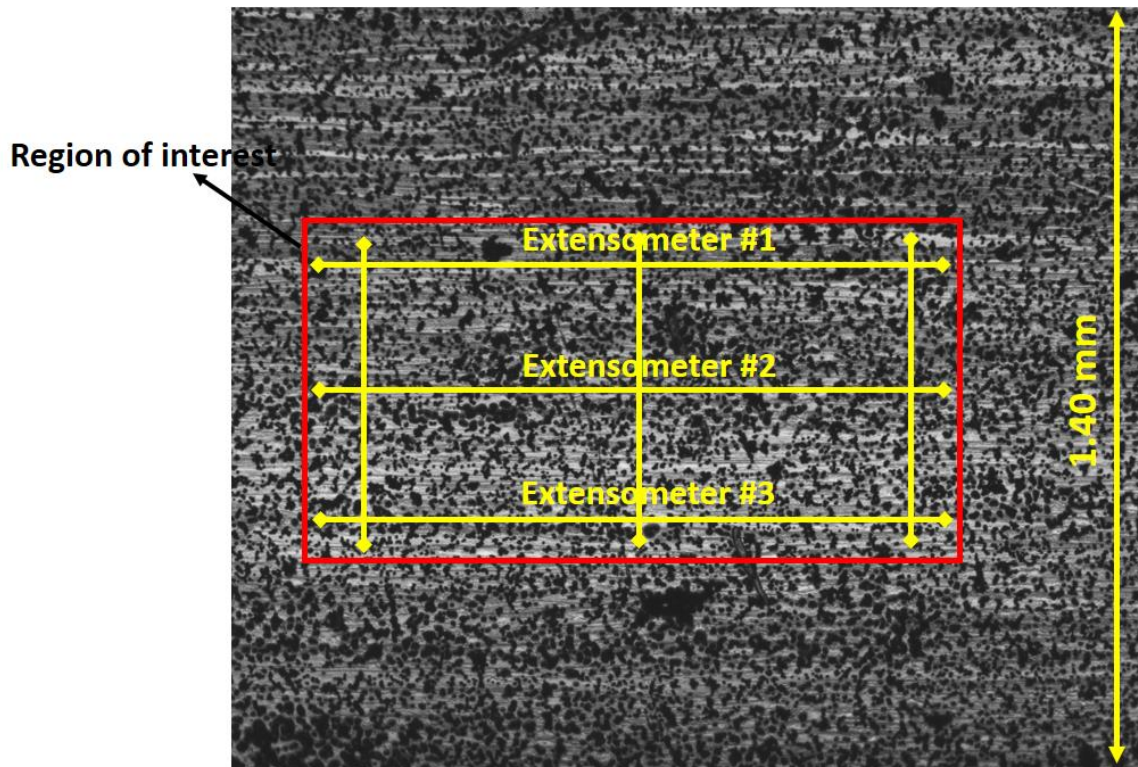


Figure 44. Speckle patterns on biopolymers doge-bone specimens.

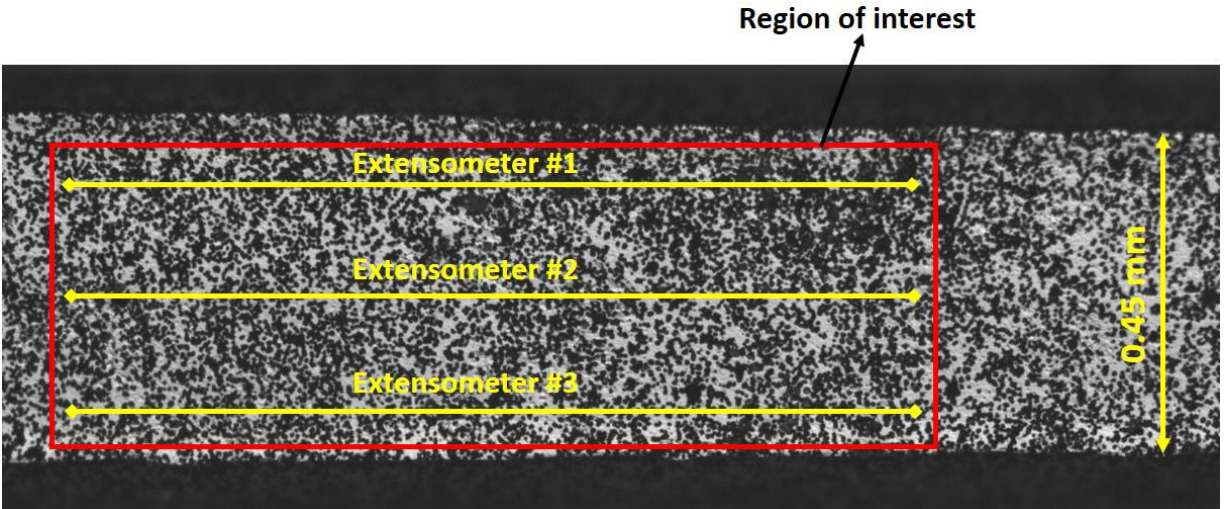


Figure 45. Speckle patterns on nanocomposite filament specimens.

Several tensile tests were performed using the dog-bone specimens to measure the isotropic elastic properties of both biopolymer resins (i.e., SOEA and SOEA+HEA). Engineering stress was calculated using forces measured by machine load cell divided by the initial cross-section of specimen, and also, engineering strain is measured by DIC. By the combination of these two and having the stress-strain curve, Young's modulus can be determined. Also, dividing vertical strains by horizontal strains the Poisson's ratio can be calculated (see Figure 44). In addition, a number of similar tests were conducted to assess the UV light cure dose.

Table 4 indicates all tested biopolymeric dog-bone and 3D-printed nanocomposite filament test specimens. As it can be seen, for each UV light cure dose three dog-bone samples were tested. Also, for SOEA and SOEA+HEA resins, five dog-bone specimens were tested. Regarding 3D-printed nanocomposite filaments, for each nanocomposite ink and Si-nHA volume fraction, five filaments were tested.

Table 4. All tested biopolymeric dog-bone specimens and nanocomposite filaments.

Type of specimen	Material	Test repetition
Doge-bone	SOEA (1.8 J/cm ² cure dose)	3
Doge-bone	SOEA (3.6 J/cm ² cure dose)	3
Doge-bone	SOEA (7.2 J/cm ² cure dose)	3
Doge-bone	SOEA (14.4 J/cm ² cure dose)	3
Doge-bone	SOEA (28.8 J/cm ² cure dose)	3
Doge-bone	SOEA (57.6 J/cm ² cure dose)	3
Doge-bone	SOEA*	5
Doge-bone	SOEA+HEA*	5
Filament	~7%Si-nHA/SOEA+HEA	5
Filament	~17%Si-nHA/SOEA+HEA	5
Filament	~25%Si-nHA/SOEA+HEA	5
Filament	~27%Si-nHA/SOEA+HEA	5
Filament	~10%Si-nHA/SOEA	5
Filament	~20%Si-nHA/SOEA	5
Filament	~25%Si-nHA/SOEA	5
Filament	~30%Si-nHA/SOEA	5

According to polymer testing standards, polymers must be pre-conditioned by applying low amplitude loading/unloading cycles [97]. As it can be seen in Figure 46, for an 80 second period, the biopolymeric dog-bone specimen was under very small cyclic tension from 40 to 60 μm , and then the main tension displacement was applied in the rate of 1 mm/min.

* Cured at 57.6 J/cm² UV light dose.

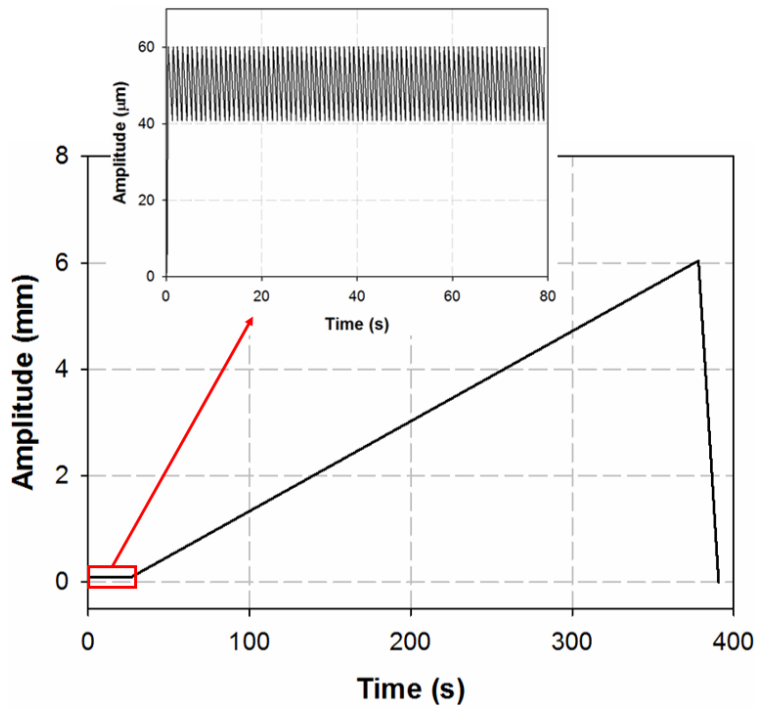


Figure 46. Loading profile of biopolymeric dog-bone specimen tests.

In regard to filament tests, all specimen were pre-loaded up to 10 N and then after that, the main tension displacement was applied at the rate of 1 mm/min (see Figure 47).

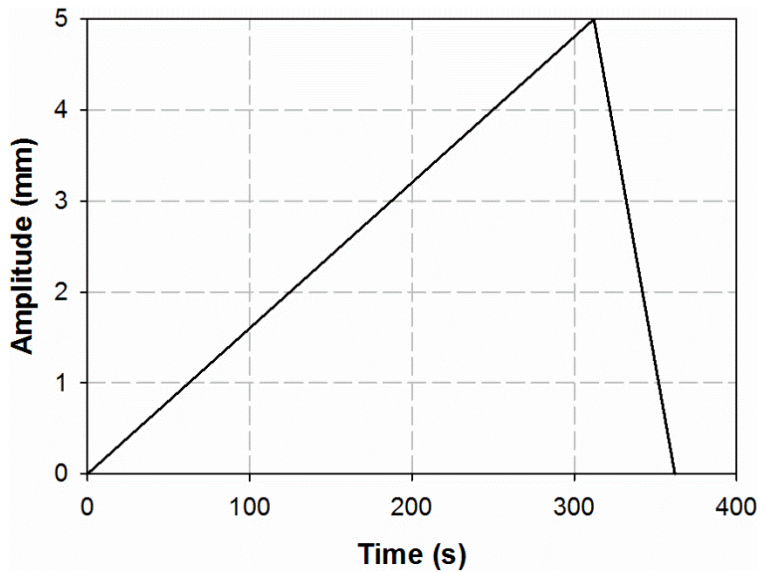


Figure 47. Loading profile of 3D-printed nanocomposite filament specimen tests.

Tensile test results of biopolymeric dog-bone specimens and nanocomposite filaments can provide a limit number of mechanical characteristics; while as mentioned in chapter 2 these types of materials have several engineering constants. In addition, implementing other types of tests such as in-and out-of-plane shear tests can be challenging and expensive particular in this scale. Therefore, in order to compute other mechanical properties of these materials, a computational tool is required which was described in Chapter 3.

Chapter 6: Results

The numerical results computed using the developed 3D RVE FE models and constituent properties outlined in Section 3.3 are subsequently presented. First, normalized volume averaged elastic moduli, E/E_m calculated using homogenization theory are compared with predictions using the analytical models presented in Section 2.5, as well as experimental data from this project and the literature for two different material systems. Then, the capabilities of assessing in- and out-of-plane orthotropic elastic properties for the developed 3D RVEs are also presented. Experimental results for the biopolymeric dog-bone specimens and 3D-printed nanocomposite filaments are also indicated and compared with 3D RVE predictions in Section 6.2.

6.1. Computational Model Verification

In order to highlight the deformation of the generated 3D RVEs and accurate use of periodic boundary conditions for both normal and shear loading conditions, typical normal and shear stress contours for RVEs with $\varphi_i = 30\%$, $\rho = 15$, $E_i = 330$, $E_m = 1.88$, $\nu_i = 0.2$, and $\nu_m = 0.4$ are shown in Figure 48 (a-b) and Figure 49 (a-b). The applied strain for all normal and pure shear loading cases was 0.5%. The stress contours reveal the variability of stress at the inclusion/matrix interfaces within the 3D RVE resulting from the staggered non-uniform inclusion dispersion. Furthermore, the characteristic shear lag behavior for both models under an applied normal strain can be observed via the shear stress contours in the matrix (see Figure 48 (a) and 49 (a)). In this case, the shear lag response is not as pronounced as one would observe for lower volume fractions due to the influence of surrounding inclusions and their constraining effect on the matrix, which highlights the importance of considering the inclusion geometry and non-uniform inclusion

dispersion in a prediction model. Similarly, as expected the peak normal stress in the fibers of the cylindrical RVE model under an applied normal strain occurs at the fiber center and reduces towards the fiber ends. The variability in stress magnitudes between adjacent fibers is also a result of the constraining effect between the fibers and their nonuniform dispersion.

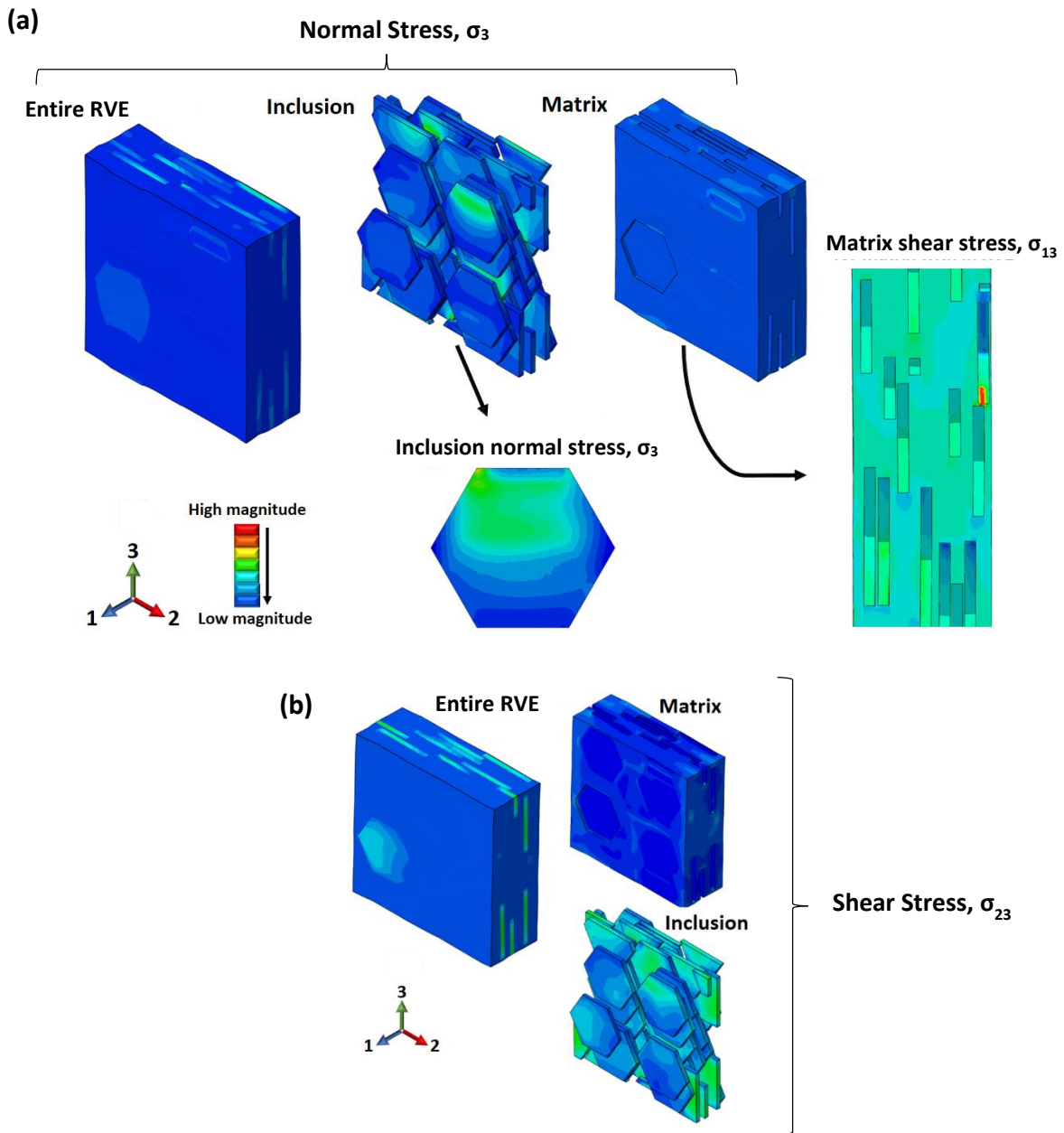


Figure 48. Stress contours for hexagonal inclusion RVE model with (a) uniaxial applied load along 3-direction, (b) pure shear applied in 23-plane.

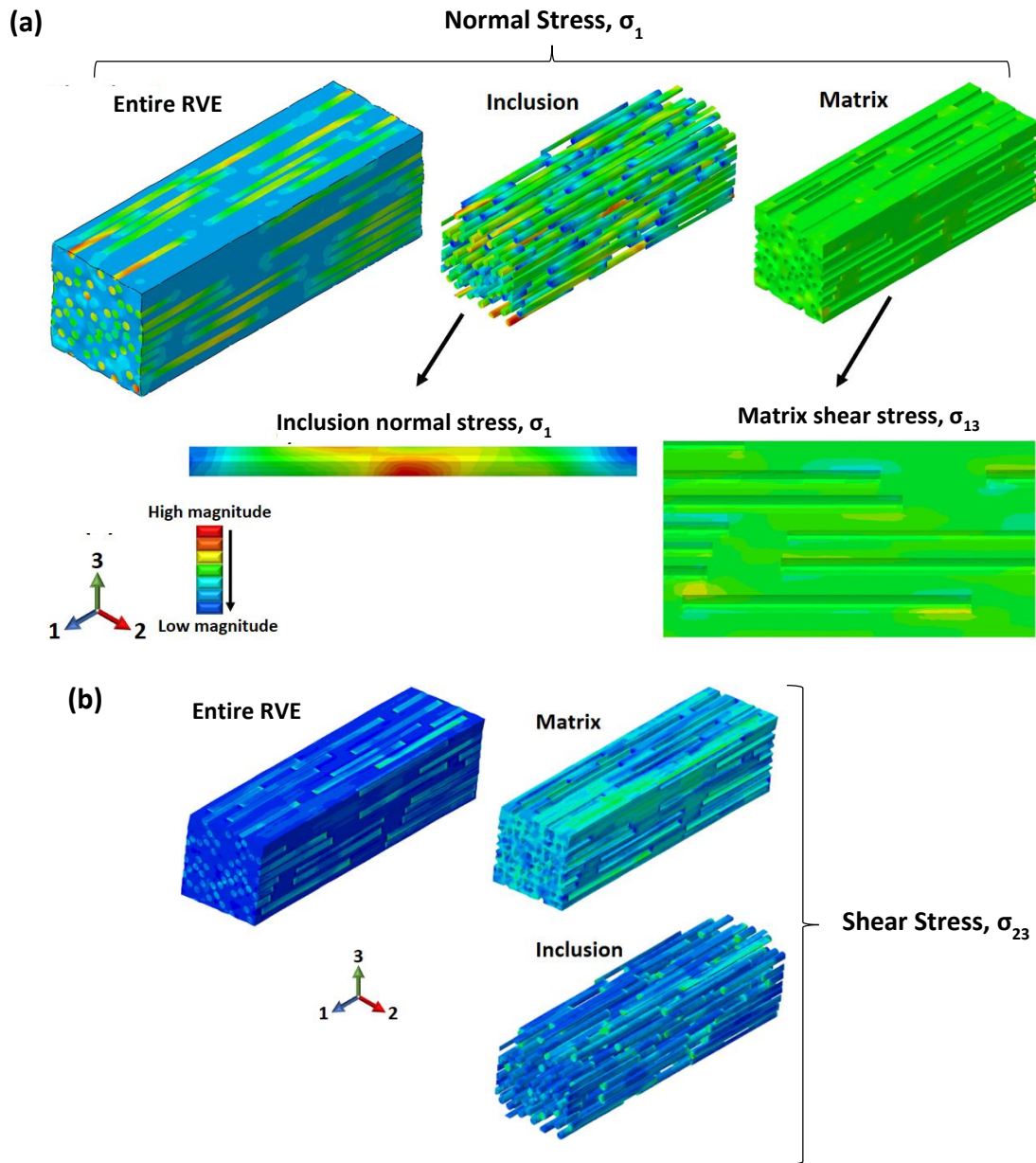


Figure 49. Stress contours for cylindrical inclusion RVE model with (a) uniaxial applied load along 1-direction, (b) pure shear applied in 23-plane.

Table 5 indicates a comparison among computed normalized moduli E_2/E_m , E_1 , and G_{12} values for five hexagonal platelet models ($E_i = 330$, $E_m = 1.88$, $\nu_i = 0.2$, and $\nu_m = 0.4$) with randomly generated non-uniform particle dispersion morphologies, along with results from the analytical

models presented in Section 2.5, as well as, experimental data of a nacre-mimetic material generated using alumina micro-platelets and chitosan by Mirkhalaf and Barthelat [35]. All have 10% inclusion volume fraction. Similarly, Table 6 presents another comparison among calculated normalized modulus, E_1/E_m , values for five cylindrical inclusion models with randomly generated non-uniform particle distribution morphologies, along with results from the presented analytical models in Section 2.5, and experimental data for a short carbon fiber/polypropylene composite having 10% fiber volume fraction studied by Fu et al. [79]. It should be noted that the constituent material properties and inclusion aspect ratios used here for the cylindrical inclusion RVE models were taken from Ref. [79] and were presented in Table 3. As it is evident from Tables 5 and 6, the average deviation of 3D RVE results with experimental data is approximately 5% for both models and each morphology, demonstrating an excellent agreement. The minor deviations may be due to assuming perfectly aligned inclusions in the 3D RVE models, while the real material could have several inclusion misalignments. Note that a number of 3D RVEs with different dimensions were considered to determine a suitable size. Based on the very good agreement with experimental data in Table 5 and 6, the selected volume for the hexagonal and cylindrical inclusion models were 1125 and $375 \mu\text{m}^3$, and used for all subsequent predictions.

The higher deviation of analytical models from both experimental and 3D RVE results can be seen for both material systems. However, among these analytical models, the modified shear lag model has a good agreement for hexagonal platelet inclusion (Table 5) with both experimental and 3D RVE results. Other studies also used different versions of the shear lag model to predict the mechanical responses of platelet inclusion biomimetic composites [50-53]. Regarding cylindrical inclusions, Mori-Tanaka model has a good agreement with both experimental and 3D RVE results

compared to other analytical models (Table 6). More details of reasons for these deviations will be discussed in the following paragraph.

Table 5. Comparison between normalized moduli (E_2/E_m), E_1 , and G_{12} from 3D RVEs (5 trials), analytical models, and experimental data of a nacre-mimetic material (i.e., alumina/chitosan) with a volume fraction (ϕ_i) of 10%. Error is calculated against the experimental data.

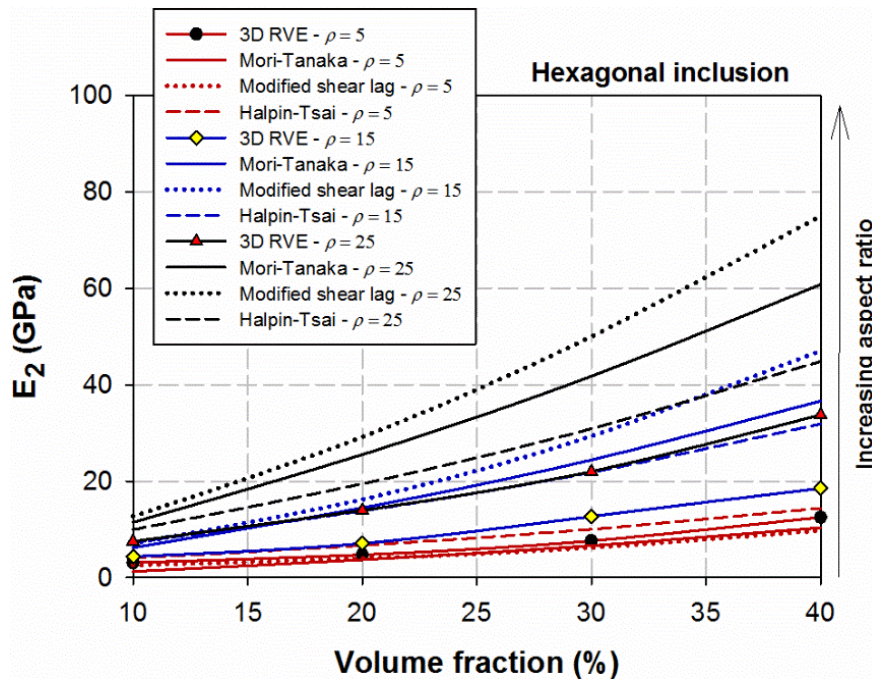
	3D RVE Trial 1	3D RVE Trial 2	3D RVE Trial 3	3D RVE Trial 4	3D RVE Trial 5	3D RVE Avg.	Mori- Tanaka	Mod. shear- lag	H-T	Exp [3 5]
E_2/E_m	3.72	3.75	3.70	3.69	3.73	3.72	3.30	3.76	3.88	3.56
Error (%)	4.61	5.48	3.96	3.65	4.95	4.53	7.37	5.78	8.98	-
E_1 (GPa)	3.33	3.10	3.51	3.35	3.41	3.34	-	-	-	-
G_{12} (GPa)	0.80	0.85	0.77	0.88	0.75	0.81	-	-	-	-

Table 6. Comparison between normalized moduli (E_1/E_m) from 3D RVEs (5 trials), analytical models and experimental data from a short carbon fiber/polypropylene composite having a volume fraction (φ_i) of 10%.

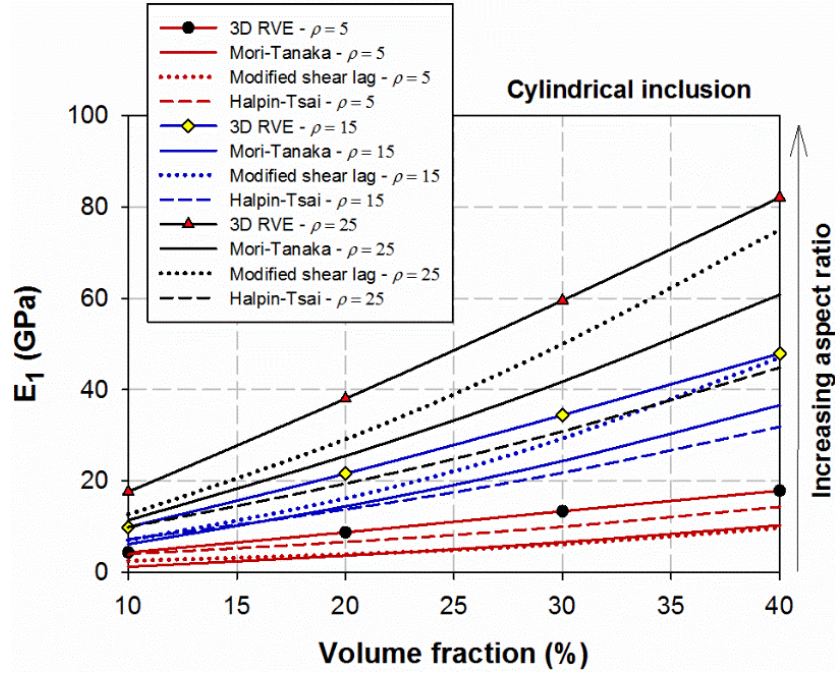
	3D RVE Trial 1	3D RVE Trial 2	3D RVE Trial 3	3D RVE Trial 4	3D RVE Trial 5	3D RVE Avg.	Mori- Tanaka	Mod. shear -lag	H-T	Exp [79]
E_1/E_m	9.11	8.92	9.00	9.01	9.15	9.04	9.33	9.41	6.82	8.58
Error (%)	6.08	3.92	4.85	4.95	6.63	5.28	8.66	9.60	20.54	-

Figures 50 (a-b) compare the predictions for E_2 from hexagonal inclusion 3D RVE model and E_1 for cylindrical inclusion 3D RVE model with the aforementioned analytical models. For the Mori-Tanaka model, the inclusion shape was approximated as ellipsoidal with a perfectly aligned distribution assumption. As seen in these Figure ures, for lower aspect ratios, the analytical model predictions are close to those of the 3D RVEs for both inclusion shapes. However, with increasing volume fraction and aspect ratio, the discrepancy between 3D RVE and analytical models tends to increase. According to previous studies [43, 44], inaccurate predictions for higher aspect ratios and volume fractions for shear lag and Halpin-Tsai models are expected since they do not accurately account for the inclusion shape, their dispersions and three-dimensional effects, including inclusion overlap, which are characteristic of realistic microstructures. Modified shear lag models [50-53], which are often used for biomimetic composites, have similar limitations and

thus cannot be used to predict all elastic constants. The reason for notable discrepancies between the Mori-Tanaka model and the 3D RVEs, particularly for higher volume fractions, stems from assuming ellipsoidal shape inclusions instead of cylindrical and hexagonal shapes as well as assuming non-realistic inclusion dispersions. Previous studies have reported inaccuracies with the Mori-Tanaka model for higher aspect ratios [98, 99]. By accurately representing inclusion shape/size and their realistic non-uniform dispersion in three dimensions, such as with the 3D RVE models reported herein, the local stress field variability and cylindrical inclusion interactions can be considered, which allows for prediction of all orthotropic elastic constants.



(a)



(b)

Figure 50. Comparisons of Young's modulus versus volume fraction for different aspect ratios among established analytical models (i.e., Mori-Tanaka, modified shear lag, and Halpin-Tsai) and 3D RVE results (a) E_2 for hexagonal platelet and (b) E_1 for cylindrical inclusions model.

Figure 51 shows the predicted variation of normalized Young's modulus with inclusion volume fraction along the fiber direction (E_1) for a composite with aligned cylindrical inclusions and along the in-plane direction (E_2) for a composite with hexagonal platelet inclusions. The results from a 2D RVE model reported by Mirkhalaf and Barthelat [35], where the hexagonal inclusion shape is simplified as a rectangle. Note that the constituent properties (i.e., $E_i = 330$ GPa, $\nu_i = 0.2$, $E_m = 1.88$ GPa, and $\nu_m = 0.4$) and inclusion ρ aspect ratio (i.e., $\rho = 15$) for all three of the models are the same. Although the predicted results for the hexagonal platelet 3D RVE model are comparable with the 2D RVE model predictions, there is a notable discrepancy with the results from the cylindrical inclusion 3D RVE.

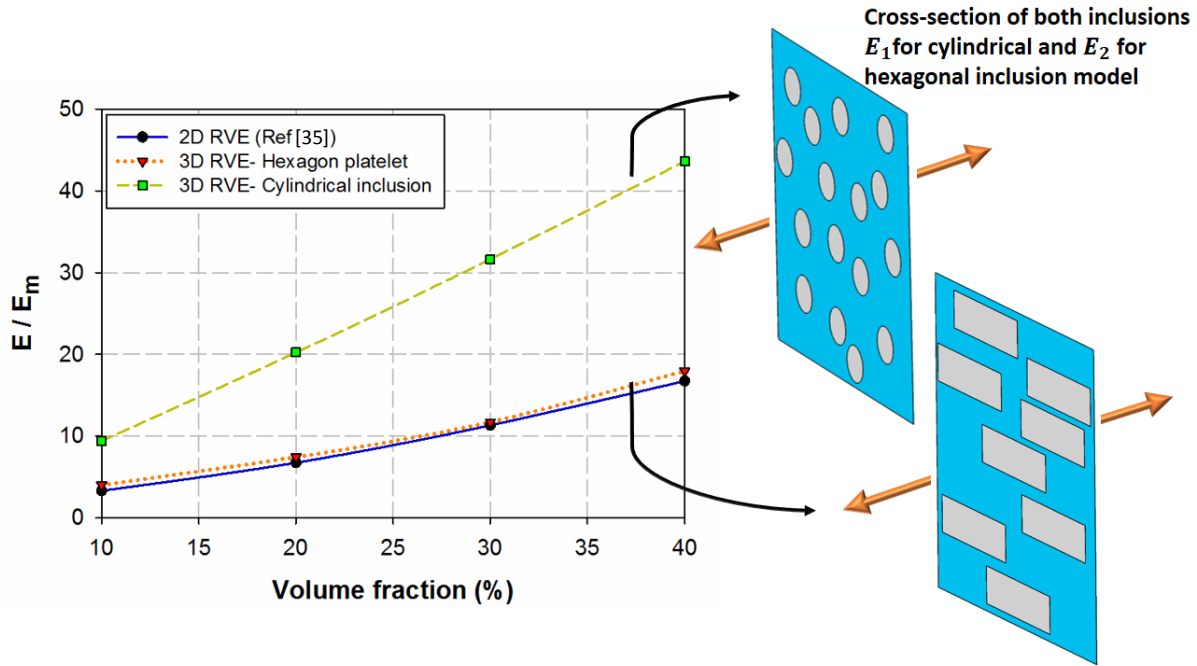
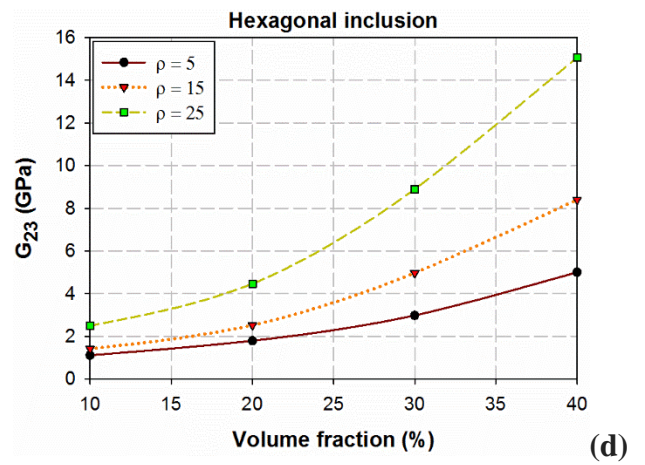
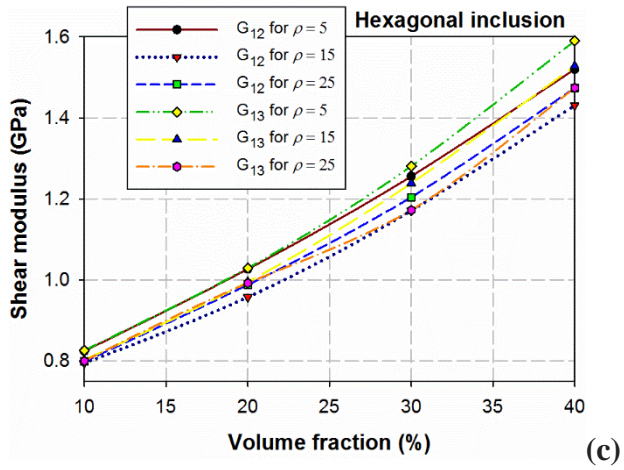
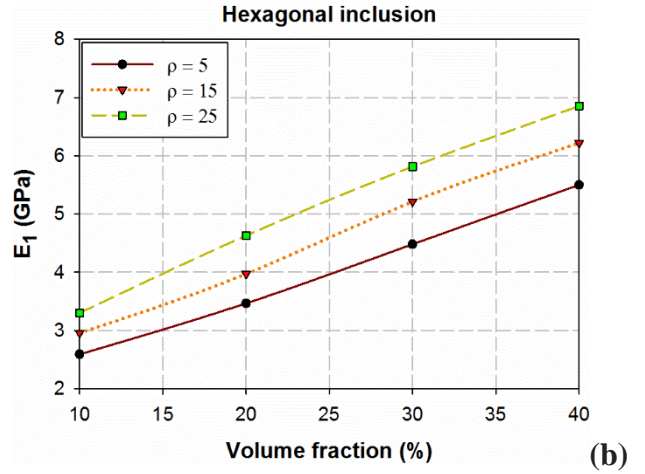
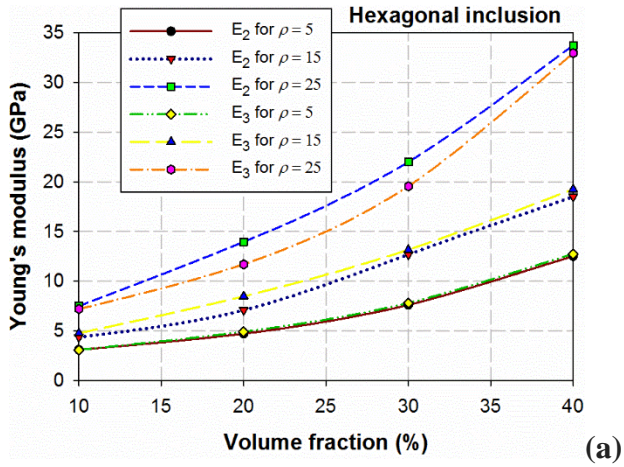
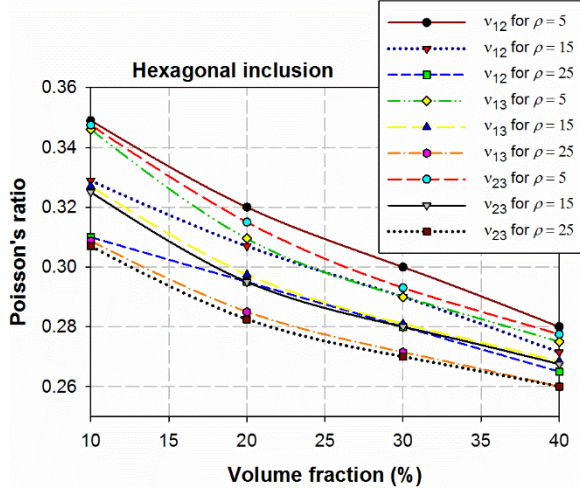


Figure 51. Comparison of normalized Young's modulus (E / E_m , where E_m is the Young's modulus of the matrix) versus volume fraction between 2D RVE and both 3D RVE models (i.e., hexagon platelet in-plane (E_2 or E_3) and cylindrical inclusion in the longitudinal direction (E_1)).

To demonstrate the capabilities of the developed 3D RVE models for predicting all in- and out-of-plane elastic constants, a series of simulations were performed using the constituent properties reported by Mirkhalaf and Barthelat [35] (see Table 3). Figures 52 (a-e) illustrate the predicted elastic constants versus volume fraction (φ_i) with various aspect ratios ($\rho = 5, 15, 25$) for the hexagonal platelet 3D RVE model. Note that all directions and planes for this model were defined based on the coordinate system indicated in Figure 48. Figure 52 (a) demonstrates the non-linear relationship between E_2 and φ_i and between E_3 and φ_i . By increasing φ_i from 10% to 40%, the discrepancy between each aspect ratio (ρ) tends to be increased. For the hexagonal platelet model, a direct relationship exists between L and E_2 or E_3 based on isostrain equations; thus, by enlarging L for a constant volume fraction, E_2 and E_3 should increase. Transverse isotropic properties can be

implied by the approximately identical values of E_2 and E_3 for a given volume fraction, which is expected since the platelet inclusions are staggered and non-uniformly dispersed. Figure 52 (b) shows the expected linear relationship of E_1 with volume fraction for all aspect ratios (ρ). According to micromechanical analytical models, such as the Rule of Mixtures, in a variety of composites, E_1 has a direct and linear relation with volume fraction [43]. In addition, in the platelet model, by increasing volume fraction or aspect ratio, cross-sectional overlaps among platelets are created; therefore, E_1 increased linearly. The approximately linear relationship between G_{12} and volume fraction (φ_i) and between G_{13} and volume fraction (φ_i) are shown in Figure 52 (c). By increasing ρ , the nonlinear trend of these out-of-plane shear moduli, tend to increase through φ_i . The nonlinear trend of in-plane shear modulus G_{23} versus φ_i is represented in Figure 52 (d). The discrepancy between each ρ tends to increase with φ_i due to the complex shape of the hexagonal inclusions. Also, by increasing L and the area of hexagons, the effect of increased cross-sectional overlaps among platelets in shear modulus can be seen in this Figure. Furthermore, the nonlinear relationship of ν_{12} , ν_{13} , and ν_{23} which are in- and out-of-plane Poisson's ratios versus φ_i are presented via Figure 52 (e). The similarity between ν_{12} and ν_{13} for different volume fractions and aspect ratios further confirms that the predicted properties are consistent with a transversely isotropic material. It is evident in this Figure that the nonlinearity of in-plane Poisson's ratio (ν_{23}) versus φ_i is slightly greater than out-of-plane Poisson's ratios, which may be attributed to the hexagonal shape of the particles. It can be noted that the size of micro-platelets (i.e., aspect ratio (ρ)) in these types of microstructures can play a pivotal role in mechanical performances for various biomimetic material systems and applications [50-53].



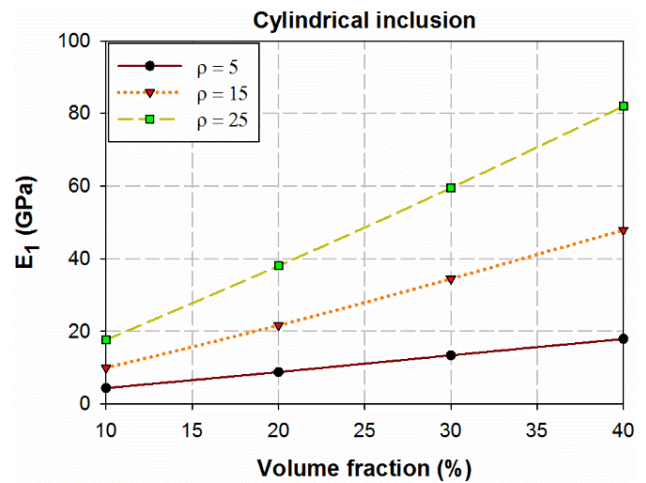
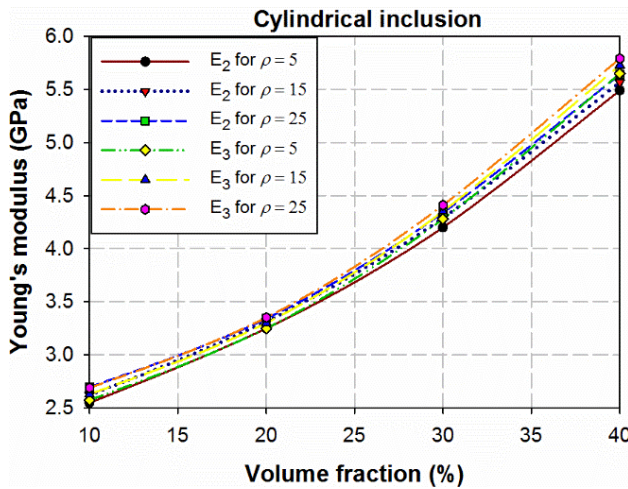


(e)

Figure 52. Computed orthotropic elastic constants for hexagonal platelet model versus volume fraction (φ_i) for various aspect ratios. (a) E_2 , E_3 , (b) E_1 , (c) G_{12} , G_{13} , (d) G_{23} , and (g) ν_{12} , ν_{13} , and ν_{23} .

Similar results for the cylindrical inclusion 3D RVE model are presented in Figure 53 (a-e). Directions and planes for this model were defined with the coordinate system in Figure 49. The similar non-linear relationship between E_2 and E_3 versus φ_i is shown by Figure 56 (a). Unlike the hexagonal platelet model, by increasing φ_i from 10% to 40%, the discrepancies between aspect ratios (ρ) are relatively minor. The reason for these differences are likely due to the shape of the inclusion. By increasing the length of the cylinders (L), the inclusion enlarges only in the longitudinal direction. Therefore, the transverse moduli, E_2 and E_3 , are not greatly affected. However, by increasing L in the hexagon platelet model, the particle is enlarged in both transverse directions. This affects E_2 and E_3 . Similar to the hexagonal platelet model, this model also demonstrates transverse isotropy, as one would expect due to the aligned cylindrical inclusions. The linear behavior of E_1 is displayed via Figure 53 (b), which is consistent with other aligned

discontinuous cylindrical inclusion composites [79, 99]. For the cylindrical inclusion model, the relationship of G_{12} , G_{13} , and G_{23} with volume fraction shown in Figure 53 (c) demonstrates greater nonlinearity when compared to the hexagonal platelet model. The reason for this greater nonlinearity may be that for higher volume fractions, the degree of non-uniformity of the cylindrical inclusion tends to be greater when compared with the platelets. Therefore, the discontinuity of cross-sectional overlaps among cylindrical inclusion tends to be decreased leading to the higher magnitudes for G_{12} , G_{13} , and G_{23} . However, discrepancies among different aspect ratios (ρ) are negligible for shear modulus due to the shape of cylinder. Due to a direct relation between Poisson's ratio and the volume fraction of stiff inclusions, Figure 53 (d) shows a linear behavior of ν_{12} and ν_{13} which gradually decrease with increasing volume fraction (φ_i). Also, because of the transverse isotropic nature of this model, the trend of ν_{12} and ν_{13} is approximately identical. The decreasing nonlinear behavior of ν_{23} versus φ_i is represented in Figure 53 (e). ν_{23} is greater in magnitude compared to the in-plane Poisson's ratios, and this is consistent with other aligned fiber-reinforced composites [79, 99].



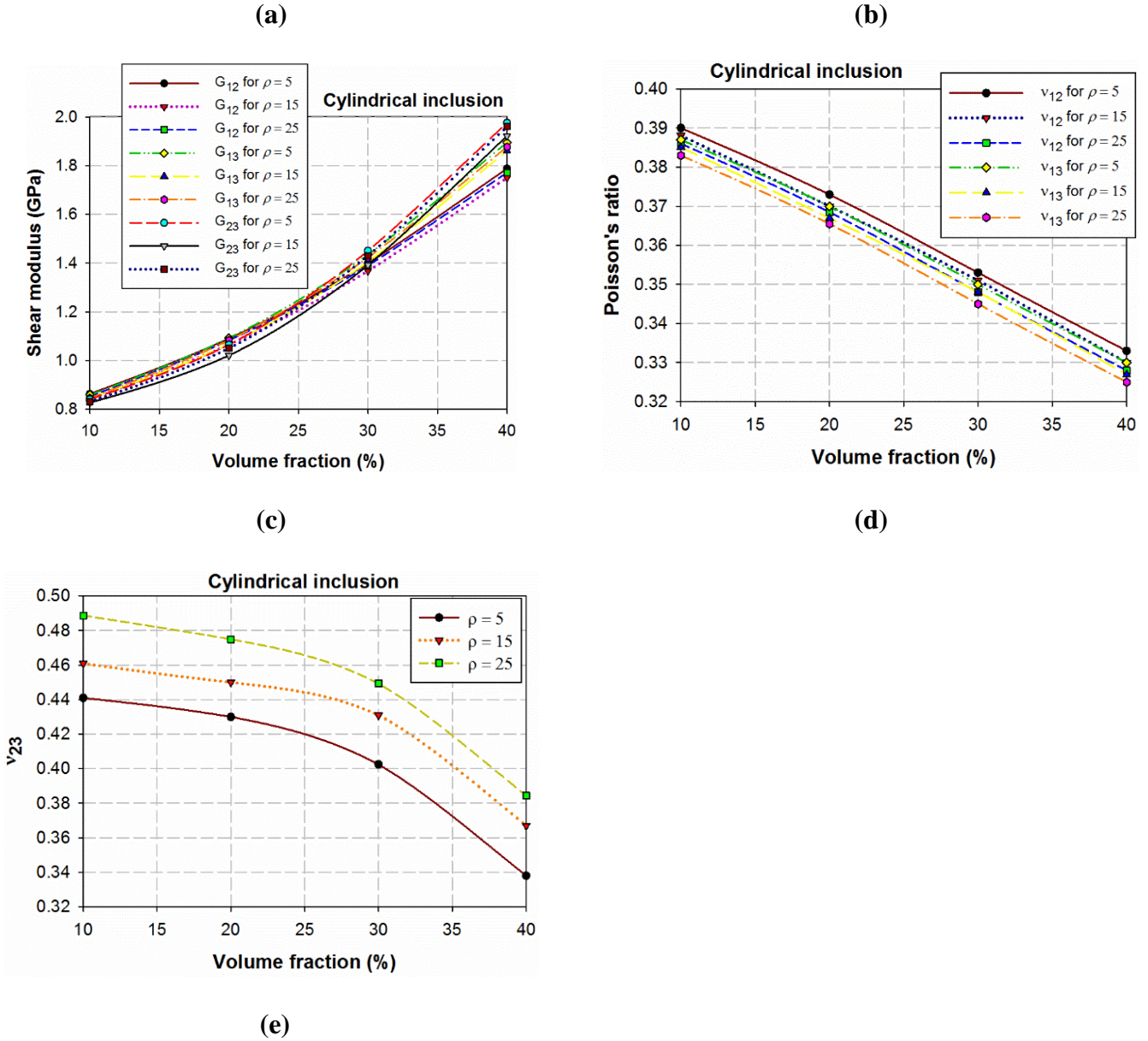
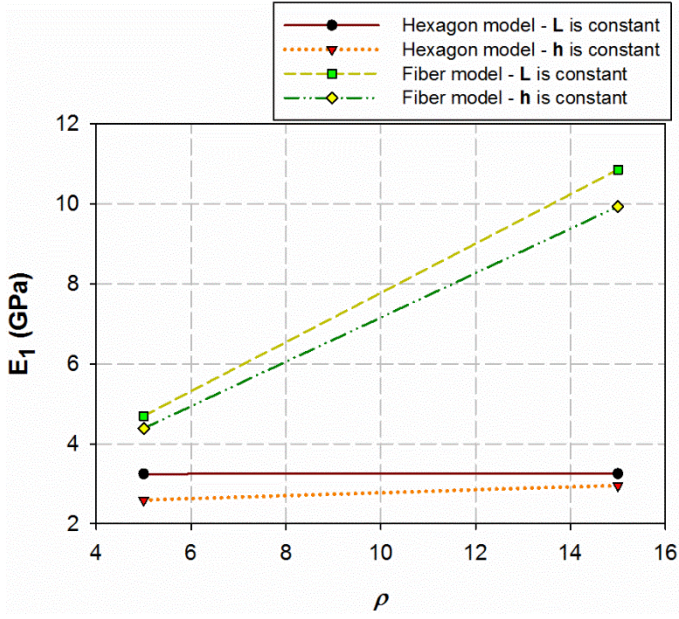


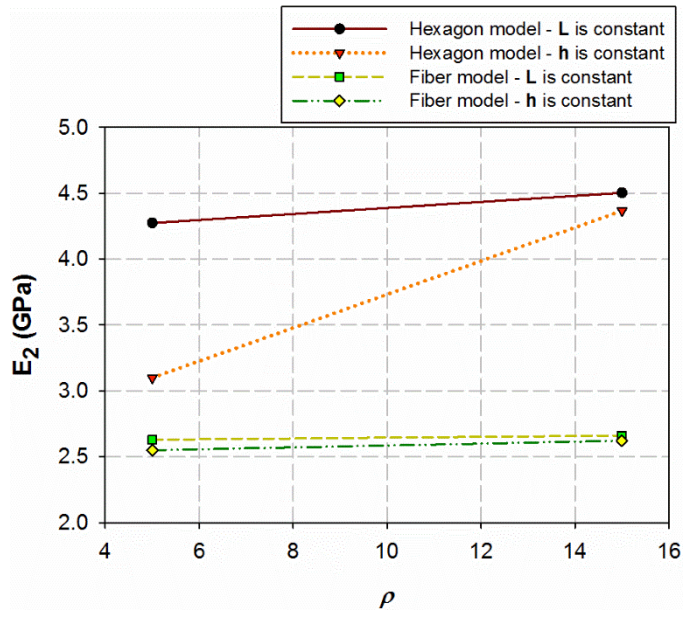
Figure 53. Computed orthotropic elastic constants for cylindrical inclusion model versus volume fraction (ϕ_i) for various aspect ratios (a) E_2, E_3 , (b) E_1 , (c) G_{12}, G_{13}, G_{23} , (d) v_{12}, v_{13} , and v_{23} .

In order to highlight the need and applicability of robust three-dimensional computational micromechanical models for designing biomimetic materials, an investigation into the effect of changing L and h individually on elastic properties was considered. As mentioned in Section 3.3, the definition of aspect ratio for both inclusions is $\rho = L/h$. Figure 54 (a-i) demonstrates

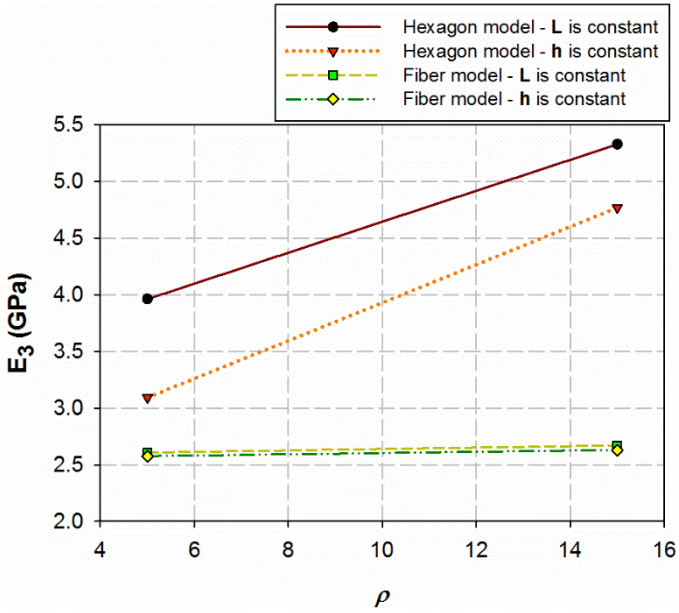
orthotropic elastic coefficients versus aspect ratio with 10% inclusion volume fraction for two cases of hexagonal platelet and cylindrical inclusion 3D RVEs. In one case the aspect ratio (ρ) was enlarged only by increasing L (i.e., h was constant), while in the other case the value of ρ was increased via increasing h (i.e., L was constant). As can be seen in Figure 54 (a), the discrepancy between the L -constant and h -constant cases for hexagon tablets with regards to E_1 calculation is negligible. On the other hand, the sensitivity of the cylindrical inclusion model can be understood for E_1 , where modulus increases with increasing fiber length or diameter. In contrast, E_2 and E_3 for the cylindrical inclusion model (Figure 54 (b) and (c)) are not notably influenced by changing aspect ratio; however, the hexagonal model is remarkably sensitive for both L and h cases. Figure 54 (d) shows notable discrepancy between L and h case for in-plane shear modulus for both hexagon and fiber models. A significant discrepancy of G_{13} and G_{23} between L and h case for hexagonal particles can be seen in Figure 54 (e) and (f). These Figures also illustrate insignificant discrepancy of G_{13} and G_{23} for cylindrical inclusion RVEs. Moreover, hexagonal platelet model ν_{12} and ν_{13} predictions are noticeably sensitive to changes in aspect ratio, whereas the fiber model predictions are less sensitive (see Figure 54 (g) and (h)). Figure 54 (i) shows that neither hexagon nor fiber model predictions are sensitive when calculating ν_{23} in each L and h cases.



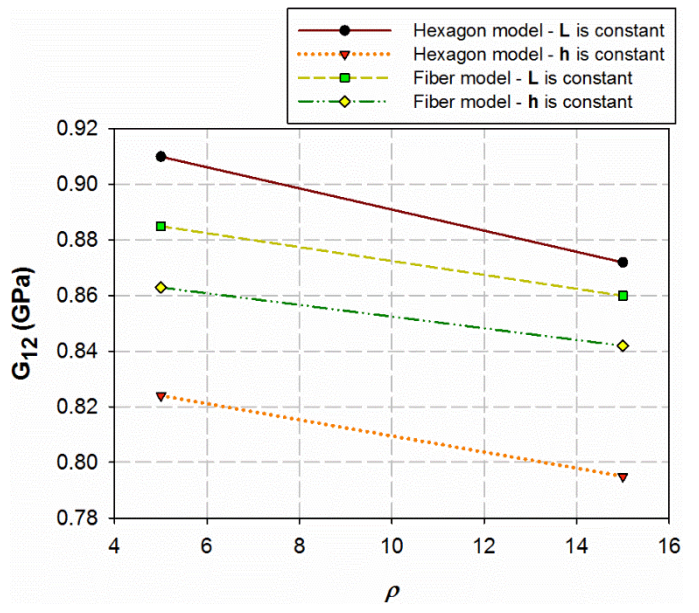
(a)



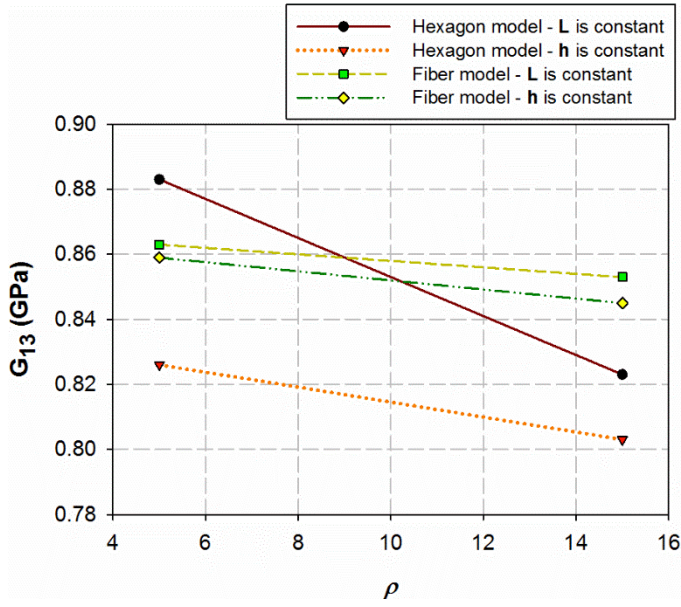
(b)



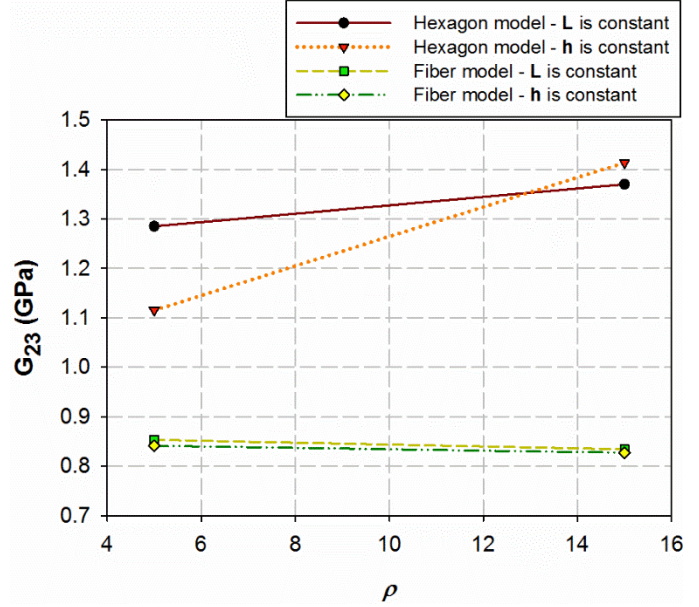
(c)



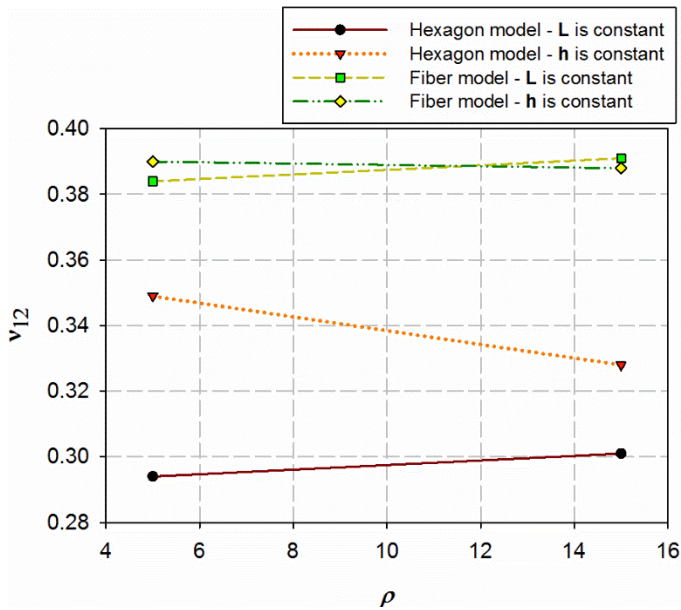
(d)



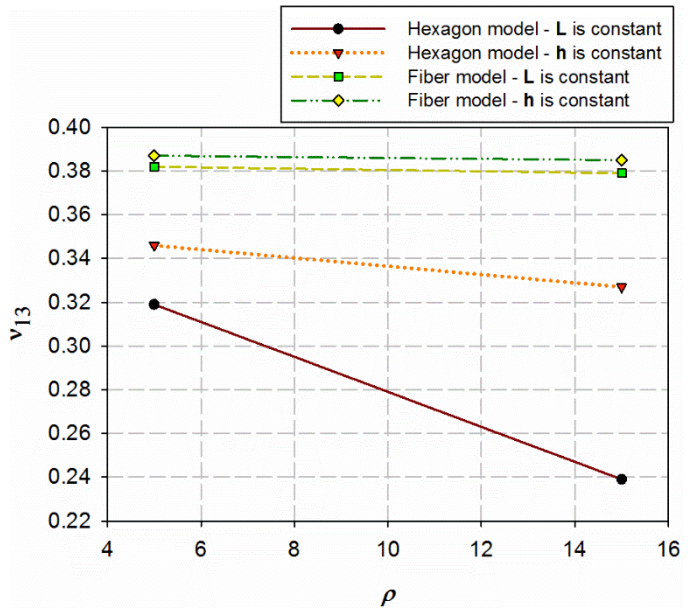
(e)



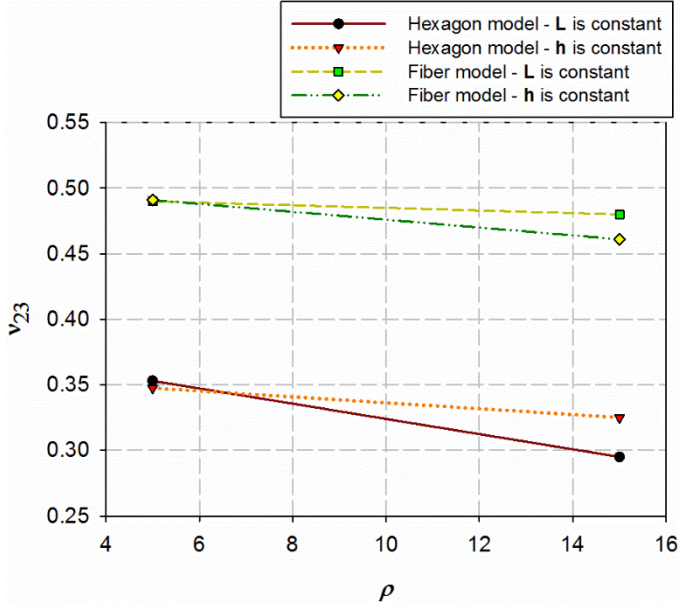
(f)



(g)



(h)



(i)

Figure 54. Computed orthotropic elastic constants for cylindrical and hexagonal inclusion models versus two aspect ratios ($\rho = 5$ and 15) for 10% volume fraction by altering dimensions of inclusion in two different cases (i.e., changing by only increasing L or h). **(a)** E_1 , **(b)** E_2 , **(c)**, **(d)** G_{12} , **(e)** G_{13} , **(f)** G_{23} , **(g)** ν_{12} , **(h)** ν_{13} and ν_{23} .

6.2. Experimental Results and Model Predictions

In this section, the mechanical test and UV light dose results of both biopolymers (i.e., SOEA and SOEA+HEA) are demonstrated. Moreover, the mechanical test results of 3D-printed nanocomposite filaments for both inks (i.e., Si-nHA/SOEA and Si-nHA/SOEA+HEA) are indicated and compared with 3D RVE predictions. The number of repeated tests which were conducted for each batch of material is also indicated in Table 4. It can be noted that all test specimens failed in the gauge section.

6.2.1. Biopolymers testing results

In order to assess the influences of UV light dose on the tensile strength of our biopolymers and to ensure that they are fully cured, several UV light dose tests were conducted on the SOEA. Figure 55 shows the tensile strength of SOEA versus different UV light doses. As it can be seen, the tensile strength of SOEA doge-bone specimens converged at approximately 28.8 J/cm². This implies that the SOEA doge-bone specimens were fully cured at this stage. However, we used the SOEA and SOEA+HEA dog-bone specimens which were cured at around 57.6 J/cm² for our main mechanical tests presented in the following.

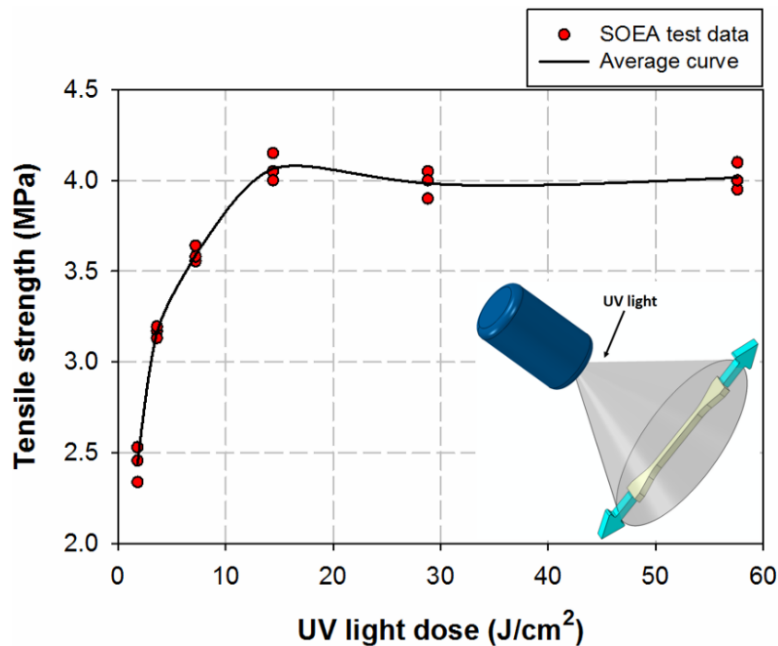


Figure 55. The effects of UV light dose on the tensile strength of both biopolymers (i.e., SOEA and SOEA+HEA).

As mentioned in Section 5.3 and indicated in Figure 44, three different vertical and horizontal extensometers are defined in Vic 2D to measure engineering strain in both directions of the dog-bone specimen. Figures 56 (a-b) illustrate engineering stress versus engineering strain curves for

three extensometers in both biopolymers (i.e., SOEA+HEA and SOEA). As it can be seen, the results of all extensometers are very similar. Also, SOEA+HEA is significantly weaker, less stiff and less extensible than SOEA.

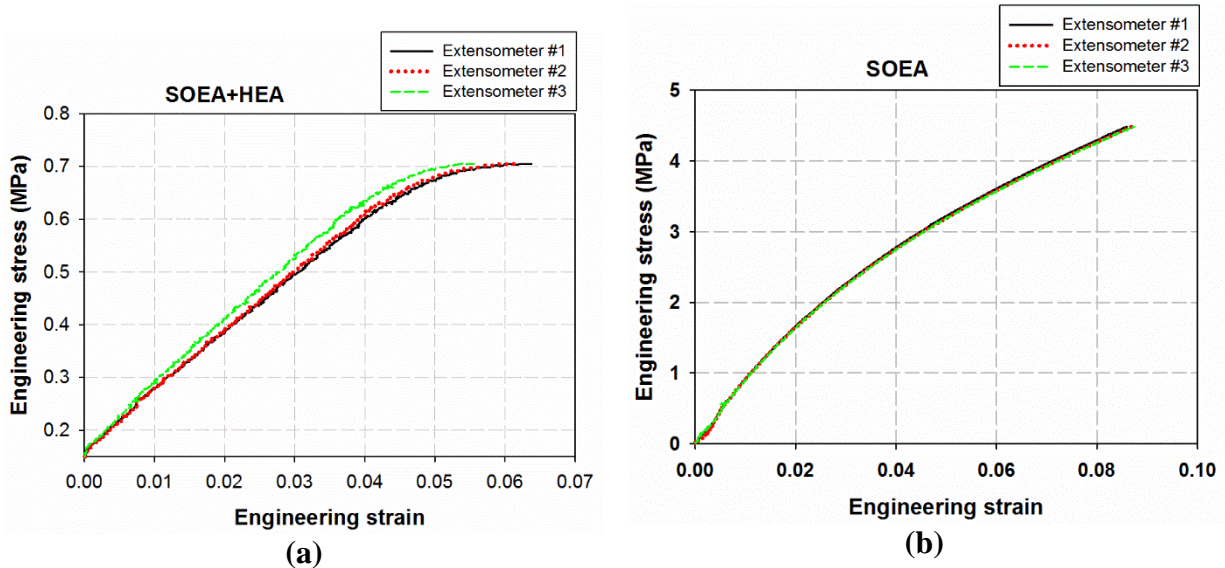


Figure 56. Stress-strain curves for both biopolymeric dog-bone specimens (i.e., SOEA+HEA and SOEA).

The obtained Young’s modulus, Poisson’s ratio, and tensile strength for SOEA+HEA and SOEA for five different tested dog-bone specimens are sequentially indicated in Table 7 and 8.

Table 7. Young’s modulus, Poisson’s ratio, and tensile strength of SOEA+HEA for five different tested dog-bone specimens.

Tests	SOEA+HEA #1	SOEA +HEA #2	SOEA +HEA #3	SOEA +HEA #4	SOEA +HEA #5	Average	Standard deviation (%)
E (MPa)	10.92	11.26	11.01	11.11	10.97	11.05	0.13
N	0.44	0.42	0.48	0.47	0.45	0.45	0.02
Tensile strength (MPa)	0.70	0.85	1.34	1.05	1.34	1.05	0.28

Table 8. Young's modulus, Poisson's ratio, and tensile strength of SOEA for five different tested dog-bone specimens.

Tests	SOEA #1	SOEA #2	SOEA #3	SOEA #4	SOEA #5	Average	Standard deviation
E (MPa)	77.74	85.71	71.62	74.06	99.80	81.78	11.39
N	0.45	0.43	0.44	0.47	0.46	0.45	0.01
Tensile strength (MPa)	3.81	4.48	3.52	3.80	3.89	3.90	0.35

The average values of Young's modulus and Poisson's ratio for both biopolymers were utilized in the FE micromechanical models presented in chapter 3. As it can be seen in these tables and Figure 57, by adding HEA to SOEA the Poisson's ratio is relatively constant; however, the strength and stiffness of SOEA are remarkably decreased. Whereas HEA had an effective role in nanocomposite ink rheology and nanoparticle alignments and dispersions in the previous section.

6.2.2. Nanocomposite filament testing results

As mentioned in Section 5.3 and indicated in Figure 45, three different extensometers are defined in Vic 2D to measure engineering strain in the longitudinal direction of nanocomposite filaments. Figure 58 (a-d) exhibit engineering stress versus engineering strain curves of 3D-printed Si-nHA/SOEA+HEA nanocomposite with different Si-nHA volume fractions (i.e., 7, 17, 25 and 27 %) for three different extensometers. As it can be seen, the results of all extensometers are almost identical. Due to pre-loading filaments, a small amount of stress was applied, and plots are not started from the origin. A quasi-brittle behavior is evident for all Si-nHA volume fractions. Moreover, by increasing Si-nHA volume fractions, the strength of corresponding nanocomposite tends to be enhanced. However, this enhancement is not linear; it means the difference between 7%Si-nHA/SOEA+HEA and 17%Si-nHA/SOEA+HEA is considerably high; while this difference

is trivial between 17%Si-nHA/SOEA+HEA and 25%Si-nHA/SOEA+HEA. Surprisingly, the difference between 25%Si-nHA/SOEA+HEA and 27%Si-nHA/SOEA+HEA is notably high. The observations in Figures (32-35) and these results can depict the pivotal role of nanoparticle orientations, dispersions, and alignments on the strength of nanocomposites.

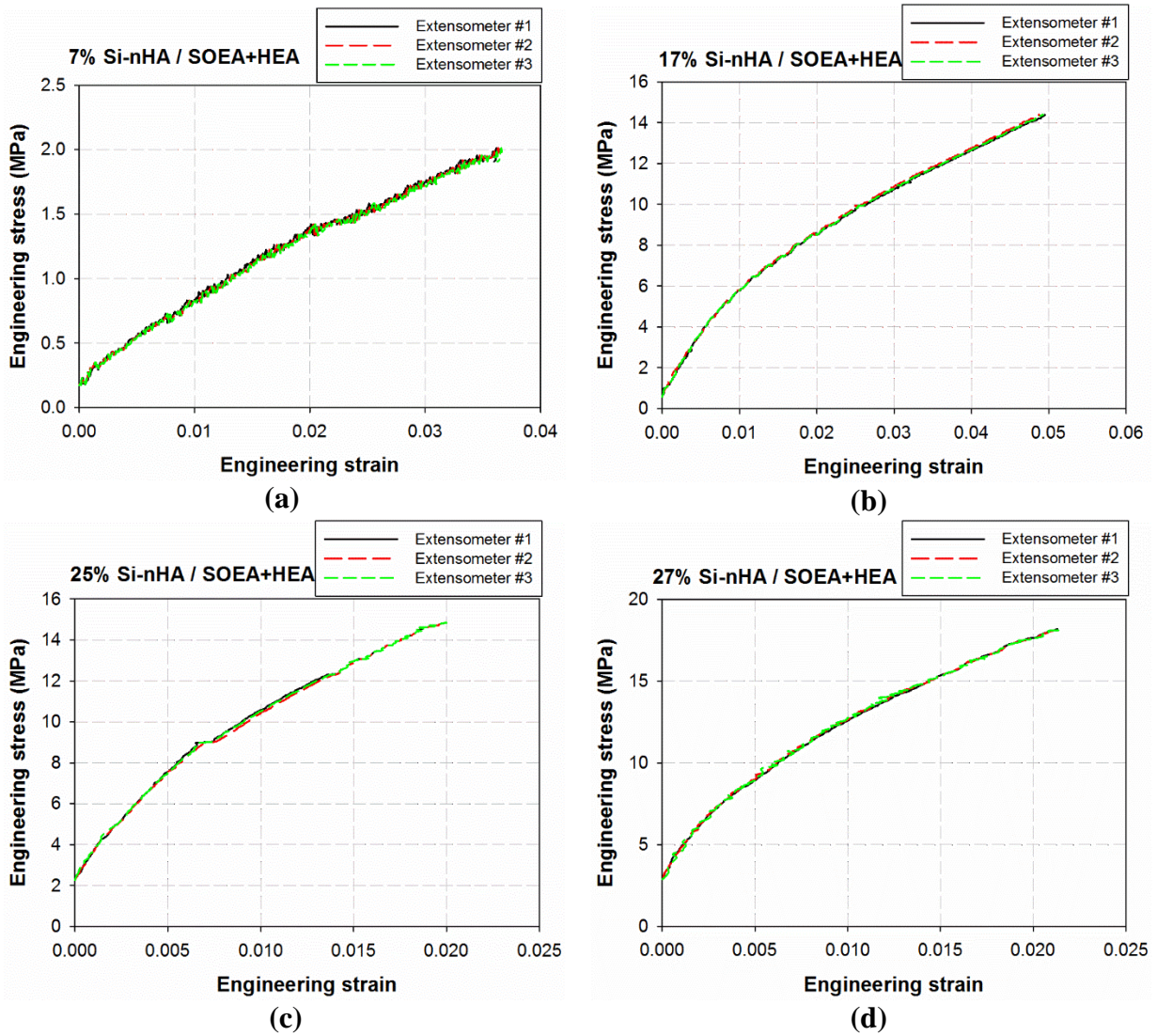
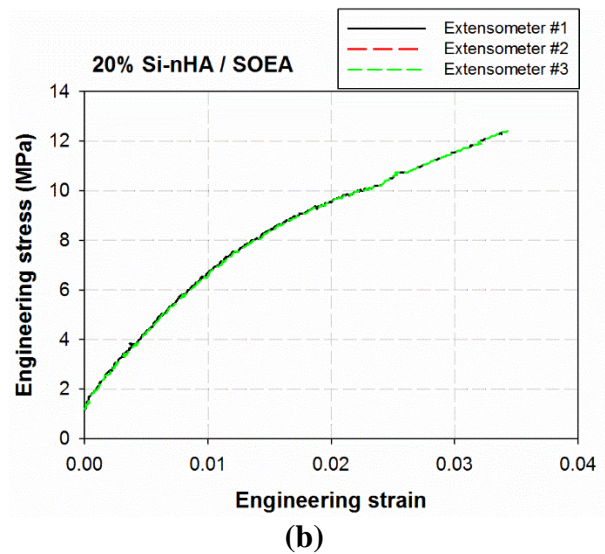
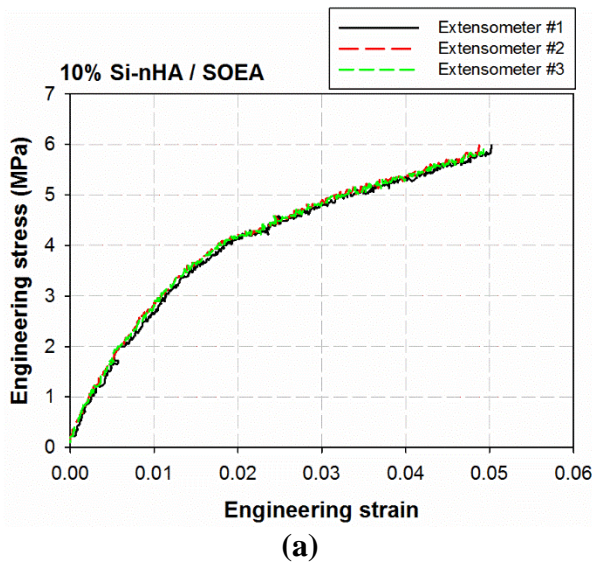


Figure 57. Stress-strain curves for 3D-printed Si-nHA/SOEA+HEA nanocomposite filaments with different Si-nHA volume fractions.

Figure 58 (a-d) illustrate engineering stress versus engineering strain curves of 3D-printed Si-nHA/SOEA nanocomposite with different Si-nHA volume fractions (i.e., 10, 20, 25 and 30 %) for three different extensometers. As it can be seen, the results of all extensometers are completely fitted. Similar to Si-nHA/SOEA+HEA a quasi-brittle behavior is evident for all Si-nHA volume fractions in this ink. In addition, by increasing Si-nHA volume fractions, the strength of corresponding nanocomposite tends to be boosted. Similar to Si-nHA/SOEA+HEA ink, a remarkable difference can be seen between the strength of 10%Si-nHA/SOEA and 20% Si-nHA/SOEA ink. Unlike Si-nHA/SOEA+HEA ink, in this ink, by increasing Si-nHA volume fraction from 20% to 25%, a significant enhancement is evident for the nanocomposite strength. However, this enhancement has not occurred between 25%Si-nHA/SOEA and 30%Si-nHA/SOEA ink. Based on the results demonstrated in Figures (36-39) and these mechanical test results, the crucial effects of ink rheology and the viscosity of matrices on the nanoparticle dispersion and alignments are evident.



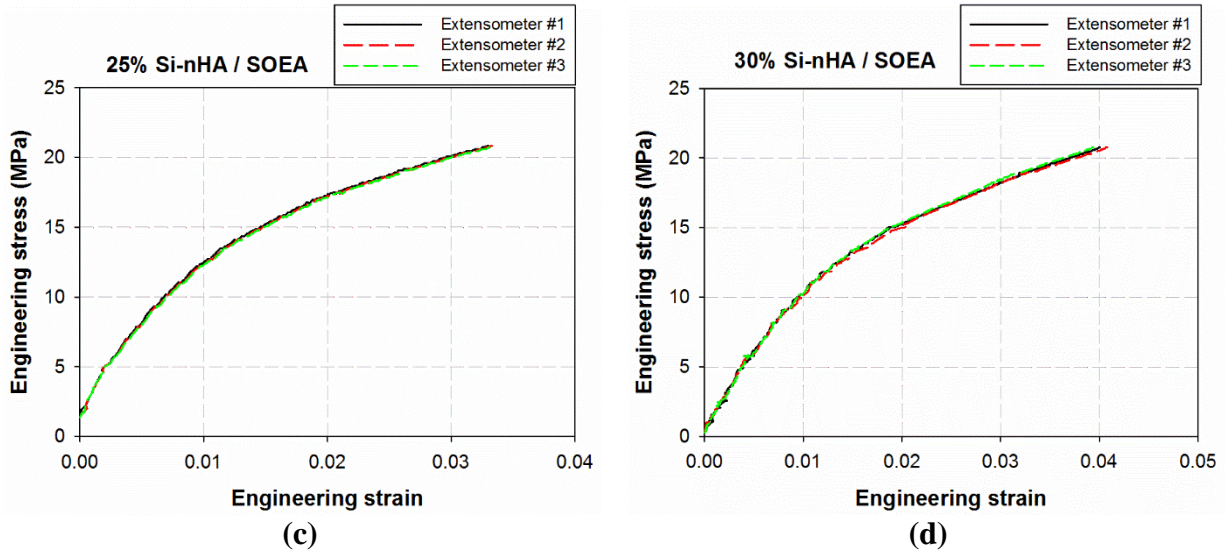


Figure 58. Stress-strain curves for 3D-printed Si-nHA/SOEA nanocomposite filaments with different Si-nHA volume fractions.

Tables 9-12 indicate the Young's modulus and tensile strength of 3D-printed Si-nHA/SOEA+HEA five different filaments for various Si-nHA volume fractions (i.e., 7, 17, 25, 27%) with two different nozzle sizes and Tables 13-16 represent the Young's modulus and tensile strength of Si-nHA/SOEA five different filaments for various Si-nHA volume fractions (i.e., 10, 20, 25, 30%) with two different nozzle sizes. These two nanocomposite inks were 3D-printed using two different nozzle tip sizes (i.e., $D_n = 0.26$ and 0.41). As it can be seen, for all Si-nHA volume fractions in both inks the average Young's modulus value of larger nozzle tip size (i.e., $D_n = 0.41$) are lower than smaller size (i.e., $D_n = 0.26$). However, as expected based on SEM images, in some cases the Young's modulus of nanocomposite filaments which were 3D-printed via $D_n = 0.41$ is greater than $D_n = 0.26$. Furthermore, the tensile strength of filaments which are 3D-printed using both nozzle tips are relatively close to each other.

Table 9. Young's modulus and tensile strength of 3D-printed 7%Si-nHA/SOEA+HEA five different filaments with two different nozzle sizes.

7%Si-nHA/SOEA+HEA	#1	#2	#3	#4	#5	Average	Standard deviation
E (MPa) – Dn =0.26	138.7	180	167.04	125	170	156.14	23.20
E (MPa) – Dn =0.41	130	90	140	120	100	116	20.73
Tensile strength (MPa)- Dn =0.26	3.12	4.12	2.75	3.58	4.54	3.62	0.72
Tensile strength (MPa)- Dn =0.41	2.01	2.22	4.36	4.02	3.53	3.23	1.06

Table 10. Young's modulus and tensile strength of 3D-printed 17%Si-nHA/SOEA+HEA five different filaments with two different nozzle sizes.

17%Si-nHA/SOEA+HEA	#1	#2	#3	#4	#5	Average	Standard deviation
E (MPa) – Dn =0.26	365	400	425	370	380	388	24.64
E (MPa) – Dn =0.41	350	395	415	364	350	374.8	29.02
Tensile strength (MPa)- Dn =0.26	15.38	15.09	13.83	14.38	12.14	14.16	1.28
Tensile strength (MPa)- Dn =0.41	12.54	13.70	14.80	15.44	12.49	13.80	1.32

Table 11. Young's modulus and tensile of 3D-printed 25%Si-nHA/SOEA+HEA five different filaments with two different nozzle sizes.

25%Si-nHA/SOEA+HEA	#1	#2	#3	#4	#5	Average	Standard deviation
E (MPa) – Dn =0.26	530	545	560	515	520	534	18.50
E (MPa) – Dn =0.41	510	495	545	525	530	521	19.17
Tensile strength (MPa)- Dn =0.26	24.26	14.41	22.49	18.90	16.51	19.32	4.08
Tensile strength (MPa)- Dn =0.41	15.33	22.41	23.21	17.17	16.39	18.90	3.63

Table 12. Young's modulus and tensile strength of 3D-printed 27%Si-nHA/SOEA+HEA five different filaments with two different nozzle sizes.

27%Si-nHA/SOEA+HEA	#1	#2	#3	#4	#5	Average	Standard deviation
E (MPa) – Dn =0.26	580	560	545	595	550	566	21.03
E (MPa) – Dn =0.41	575	555	585	525	545	557	23.87
Tensile strength (MPa)- Dn =0.26	20.02	19.43	21.64	18.22	22.78	20.42	1.80
Tensile strength (MPa)- Dn =0.41	21.13	22.15	20.41	17.31	18.71	19.94	1.93

Table 13. Young's modulus and tensile strength of 3D-printed 10%Si-nHA/SOEA five different filaments with two different nozzle sizes.

10%Si-nHA/SOEA	#1	#2	#3	#4	#5	Average	Standard deviation
E (MPa) – Dn =0.26	1400	1050	1205	1110	860	1125	198.80
E (MPa) – Dn =0.41	868	1200	915	660	880	904.60	193.09
Tensile strength (MPa)- Dn =0.26	9.68	8.94	9.42	8.64	9.13	9.16	0.40
Tensile strength (MPa)- Dn =0.41	9.30	9.51	8.53	8.87	9.23	9.09	0.38

Table 14. Young's modulus and tensile strength of 3D-printed 20%Si-nHA/SOEA five different filaments with two different nozzle sizes.

20%Si-nHA/SOEA	#1	#2	#3	#4	#5	Average	Standard deviation
E (MPa) – Dn =0.26	2255	2230	2053	1900	1800	2047	199.62
E (MPa) – Dn =0.41	2050	1700	1880	1750	2150	1906	192.17
Tensile strength (MPa)- Dn =0.26	14.20	12.40	14.84	13.78	15.22	14.09	1.09
Tensile strength (MPa)- Dn =0.41	14.76	13.18	12.23	14.53	13.54	13.65	1.03

Table 15. Young's modulus and tensile strength of 3D-printed 25%Si-nHA/SOEA five different filaments with two different nozzle sizes.

25%Si-nHA/SOEA	#1	#2	#3	#4	#5	Average	Standard deviation
E (MPa) – Dn =0.26	2440	2883	2431	2541	2714	2601.8	194.10
E (MPa) – Dn =0.41	2600	2433	2800	2450	2300	2516.6	190.79
Tensile strength (MPa)- Dn =0.26	18.53	17.34	19.17	20.83	21.88	19.55	1.81
Tensile strength (MPa)- Dn =0.41	17.04	20.14	18.79	19.92	19.12	19.00	1.22

Table 16. Young's modulus and tensile strength of 3D-printed 30%Si-nHA/SOEA five different filaments with two different nozzle sizes.

30%Si-nHA/SOEA	#1	#2	#3	#4	#5	Average	Standard deviation
E (MPa) – Dn =0.26	3494	3810	3511	3341	3736	3578.4	191.37
E (MPa) – Dn =0.41	3441	3765	3400	3680	3300	3517.2	196.61
Tensile strength (MPa)- Dn =0.26	35.87	27.87	15.17	18.80	16.68	22.88	8.77
Tensile strength (MPa)- Dn =0.41	18.31	15.99	20.53	22.86	28.29	21.20	4.71

Figure 59 demonstrates engineering stress versus engineering strain of all tested materials in this project to compare the mechanical performances of both nanocomposite inks for all Si-nHA volume fractions. As it can be seen, there is the large difference between strength and toughness of SOEA and SOEA+HEA. In effect, these two mentioned mechanical properties of SOEA is greater than SOEA+HEA. By adding 7%Si-nHA to SOEA+HEA, these two mechanical properties of 7%Si-nHA/SOEA+HEA are still relatively lower than SOEA which this behavior is not surprising according to the SEM images illustrated in Figures 24 and 28. The most impressive batch in all these experiments is 17%Si-nHA/SOEA+HEA due to a couple of reasons include (i) the toughness, strength of SOEA+HEA are significantly boosted. (ii) both these two mechanical properties for this batch is higher or at least equal to 20%Si-nHA/SOEA ink, while Young's modulus of SOEA+HEA is approximately 11 MPa and this value for SOEA is around 81. Interestingly, the lower Si-nHA volume fraction, the higher mechanical performances. Based on

the SEM images shown in Figure (32-35) this batch benefits from the best nanoparticle dispersions and alignments in all three selected regions illustrated in Figure 31.

By increasing nanoparticle volume fraction, ink rheology and thus shear stress rate in nozzle tip tend to be altered. The influences of these changes can be easily seen in Figures (32-35) particularly in the middle of filament. Therefore, in Figure 59 for higher nanoparticle volume fractions (i.e., 25, 27, and 30%), the Si-nHA/SOEA ink has better performance in comparison with Si-nHA/SOEA+HEA. Based on these results and SEM images shown in Figures (32-35), it seems the morphology of nanoparticle compactions in siding surfaces are similar for these mentioned batches of both inks; while, the differences of misalignments and clusters were evident in the middle of filaments.

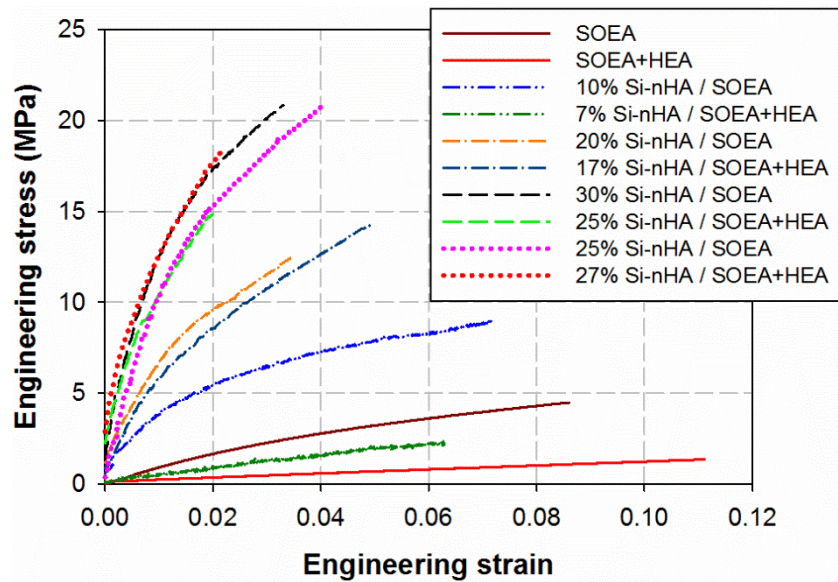


Figure 59. Stress-strain comparisons among both biopolymeric matrices and 3D-printed nanocomposite inks in different Si-nHA volume fractions.

In Figure 60 all engineering stresses shown in Figure 59 are normalized by the ultimate tensile strength of matrices which is used in each batch of nanocomposite inks. As it can be seen, by increasing Si-nHA volume fraction in SOEA ink, the strength of material tends to be relatively enhanced; however, toughness remarkably decreased. In contrast with SOEA ink, by increasing Si-nHA volume fraction in SOEA+HEA ink the strength of material significantly improved. Likewise, the toughness of SOEA+HEA particularly in 17%Si-nHA/SOEA+HEA is remarkably increased. Based on this normalized stress-strain plots shown in Figure 60, by increasing Si-nHA volume fraction, the enhancement of strength and toughness in SOEA+HEA are notably greater than SOEA.

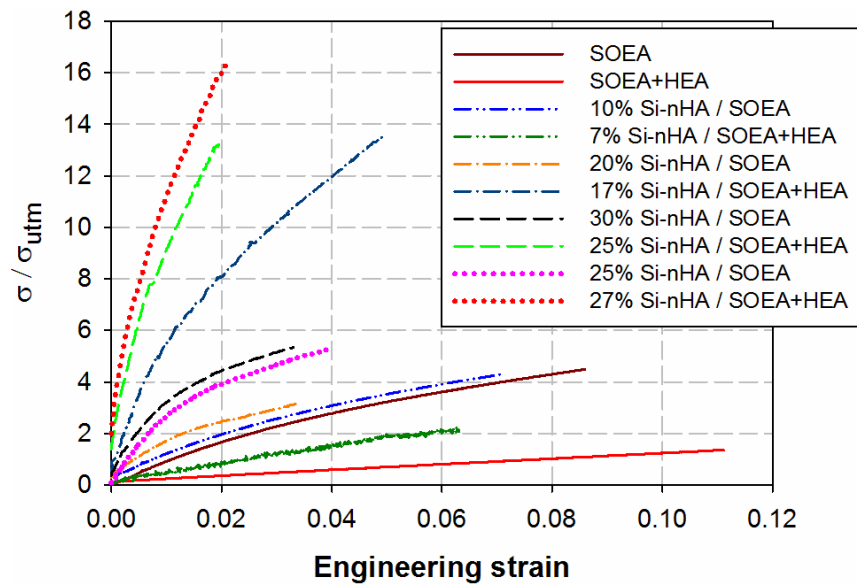
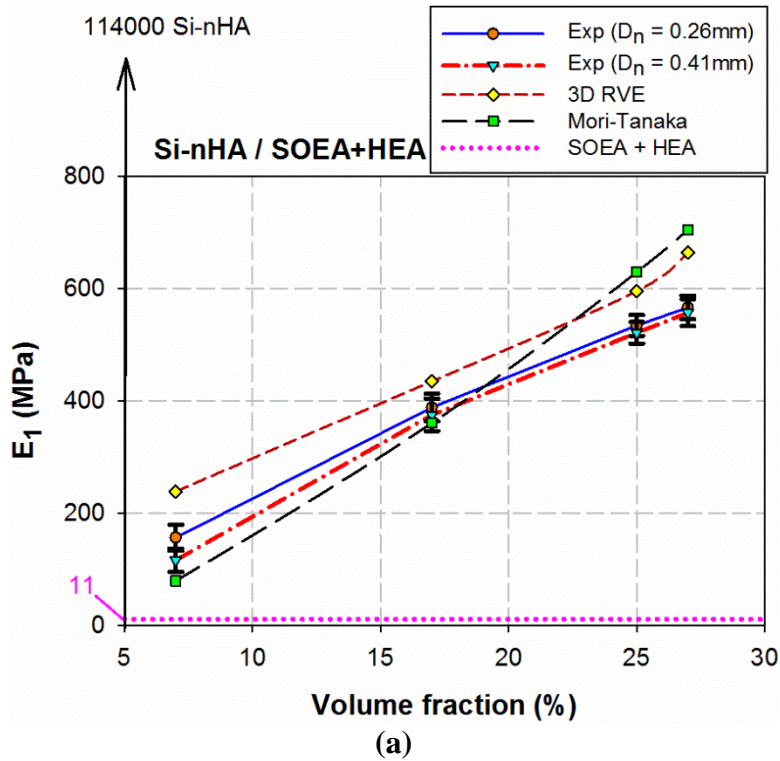
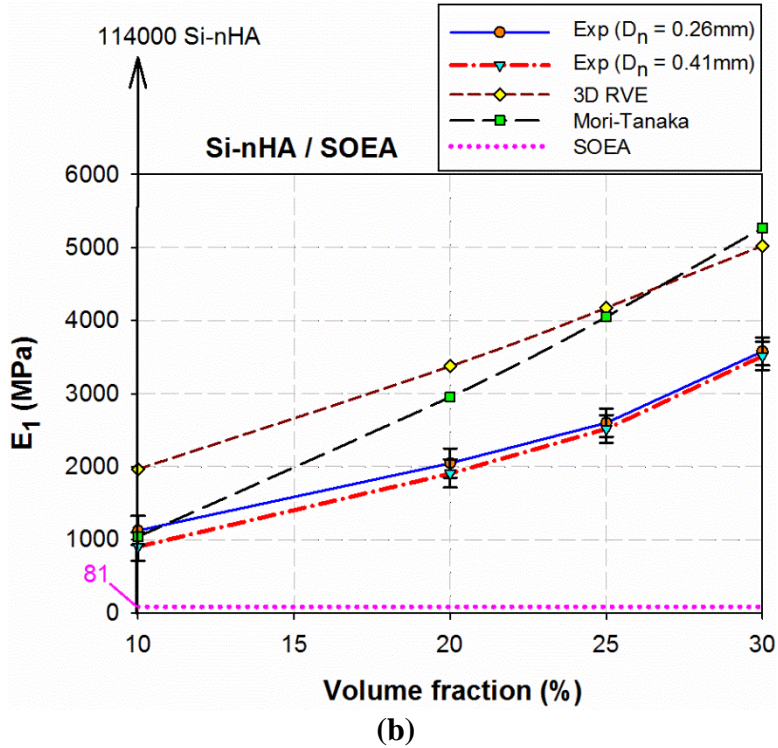


Figure 60. Normalized stress-strain comparisons among both biopolymeric matrices and 3D-printed nanocomposite inks for different Si-nHA volume fractions.

6.2.3. Comparisons of numerical, analytical, and experimental results for 3D-printed nanocomposites

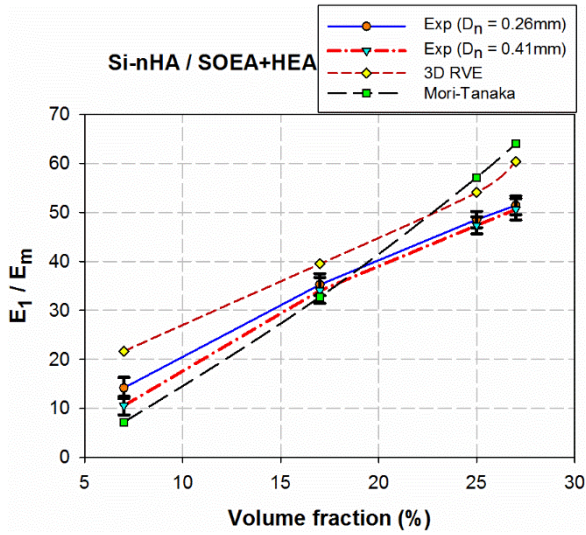
Figure 61 (a) indicates E_1 versus various Si-nHA volume fractions extracted from experimental, numerical, and analytical results include (i) 3D-printed Si-nHA/SOEA+HEA filament using two different sizes of nozzle tip; (ii) 3D RVEs and (iii) Mori-Tanaka. As it can be seen, E_1 value of matrix (i.e., SOEA+HEA) is approximately 11 MPa and this value for nHA inclusion is around 114000 MPa. Considering this wide range and the nano-scale of inclusion, 3D RVE results and experimental data are close and their trend is the same. Mori-Tanka model also has a good correlation particularly in lower volume fractions; however, it has a different trend in higher volume fraction compared with experimental and 3D RVE results.



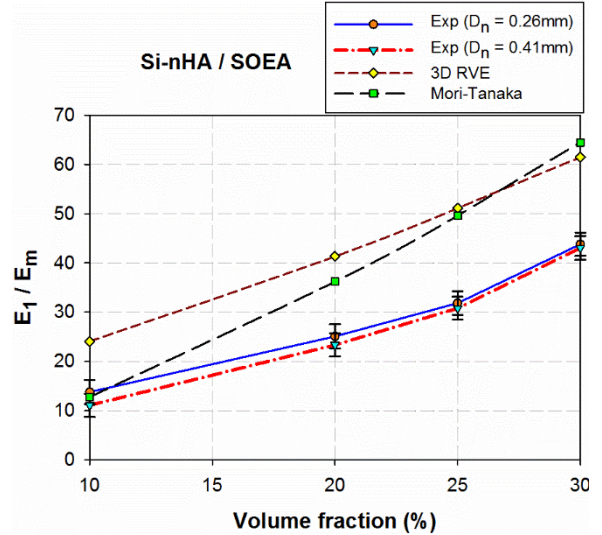


(b)
 Figure 61. Comparisons of Young's modulus versus various inclusion volume fractions among experimental, 3D RVE, and Mori-Tanaka results. (a) Si-nHA/SOEA+HEA nanocomposite (b) Si-nHA/SOEA nanocomposite.

All results in Figures 61 (a-b) are normalized by Young's modulus of matrices for each batch and demonstrated in Figure 62 (a-b). As it can be seen, the behavior and trend of each curve is identical with non-normalized curves. However, by increasing Si-nHA volume fraction, the stiffness enhancement in SOEA+HEA is greater than SOEA.



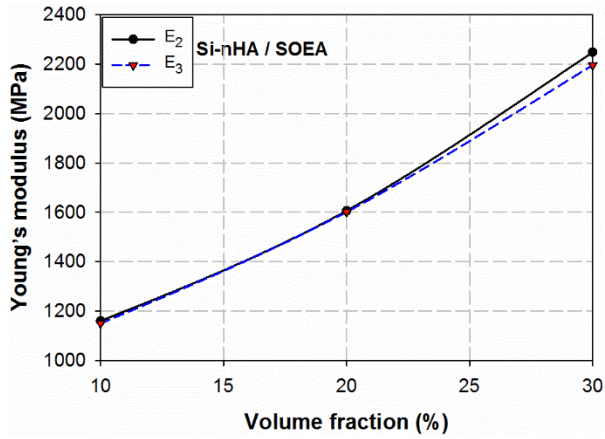
(a)



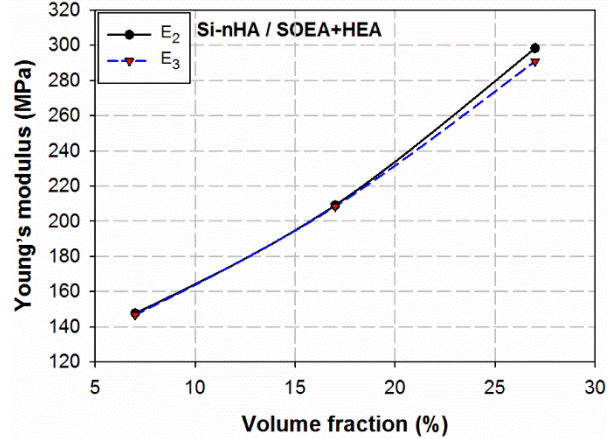
(b)

Figure 62. Comparisons of normalized Young's modulus versus various inclusion volume fractions among experimental, 3D RVE, and Mori-Tanaka results. (a) Si-nHA/SOEA+HEA nanocomposite (b) Si-nHA/SOEA nanocomposite.

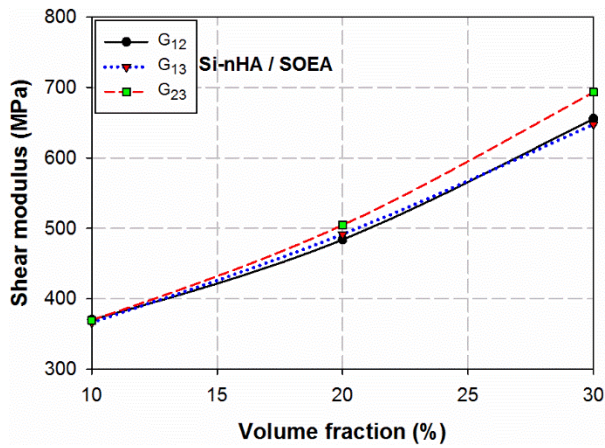
Figures 63 (a-f) exhibit computed orthotropic elastic constants versus various inclusion volume fractions using 3D RVEs for both 3D-printed nanocomposites (i.e., Si-nHA/SOEA and Si-nHA/SOEA+HEA). For Young's and shear modulus (Figures 63 (a-d)), as expected by increasing inclusion volume fraction the value of these constants also tend to be increased. In addition, due to the transversely isotropic behavior of perfectly aligned and staggered cylinders, the value of these constants in each volume fraction is close to each other. On the Poisson's ratios side, all of them naturally tend to be decreased by increasing the inclusion volume fraction. However, ν_{12} has a linear behavior and distinct trend compared to ν_{23} and ν_{13} . ν_{23} and ν_{13} also have a similar trend with small differences in their values for each volume fraction.



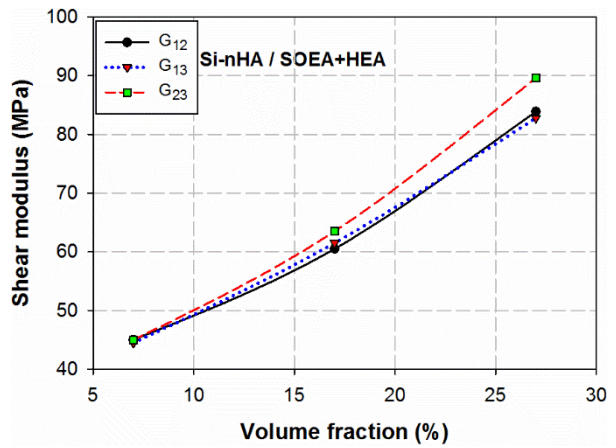
(a)



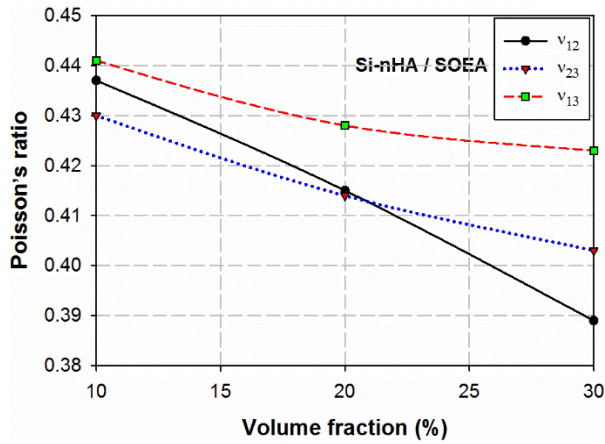
(b)



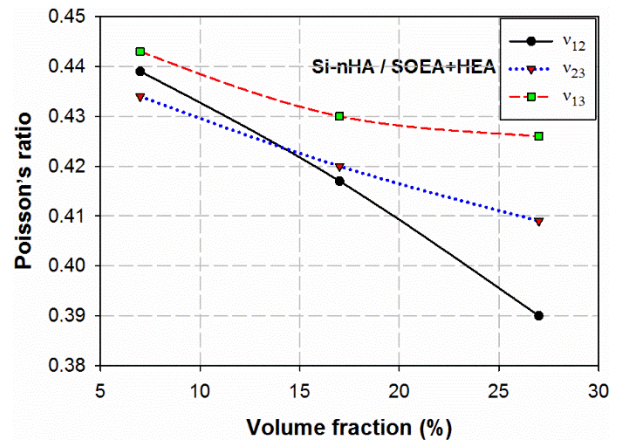
(c)



(d)



(e)



(f)

Figure 63. Computed orthotropic elastic constants using 3D RVE for both 3D-printed nanocomposites versus volume fraction. (a) E_2 and E_3 for Si-nHA/SOEA ink; (b) E_2 and E_3 for Si-nHA/SOEA+HEA ink; (c) G_{12} , G_{13} , and G_{23} for Si-nHA/SOEA ink; (d) G_{12} , G_{13} , and G_{23} for Si-nHA/SOEA+HEA ink; (e) ν_{12} , ν_{23} , and ν_{13} for Si-nHA/SOEA ink; (f) ν_{12} , ν_{23} , and ν_{13} for Si-nHA/SOEA+HEA ink.

Chapter 7: Discussion

The common characteristic among all nanocomposite batches presented in Figures (32-39) was remarkably better nanoparticle dispersions and alignments in those regions which were near the outer surfaces and conversely, there were improper misalignments and agglomerations in the middle of the filaments. This phenomenon was also reported by Hausmann et al. [101] which they investigated the dynamics of cellulose nanocrystals dispersions and alignments in a particular nanocomposite ink through DIW-type 3D printing. According to Hausmann et al. [101], the ink rheology as well as applied shear rate and stress have a crucial role in nanoparticle dispersions and alignments. One of the effective parameters on rheology and shear behavior is the viscosity of nanocomposite ink. Consequently, it can be clearly seen in Figures (32-39), Si-nHA/SOEA+HEA ink which benefits from lower viscosity has better nanoparticle dispersions and alignments compared to Si-nHA/SOEA ink which has the higher viscosity at all nanoparticle volume fractions. Higher nanoparticle volume fraction inks had better dispersions and alignments particularly near the outer surfaces of filament and nozzle tip. Siqueira et al. [102] 3D-printed a textured cellular microstructure using cellulose nanocrystal cylindrical shape nanoparticles. Figure 64 illustrates SEM image of their nanocomposite surface with 20 wt% of acetylated cellulose nanocrystals. Red arrows demonstrate the cross-section of cellulose nanocrystals. The dispersions and alignments of nanoparticles for 17-27% Si-nHA/SOEA+HEA ink and 20-30%Si-nHA/SOEA ink in regions 1 and 3 of the filaments (Figures 32-35 and 36-39) are almost analogous and comparable with Siqueira et al. [102] work presented in Figure 64. Another important parameter in nanoparticle distributions and alignments is their volume fraction. Surprisingly, in lower volume fractions (i.e., 7-10%), we observed poor dispersion and alignment and also a large number of small clusters were seen in both nanocomposite inks. These clusters were agglomerated in Si-nHA/SOEA ink and

while there were microscopic distances among nanoparticles in Si-nHA/SOEA+HEA ink. In fact, the compaction among nanoparticles which can occur by increasing nanoparticle volume fraction has integral effects on their alignments and dispersions.

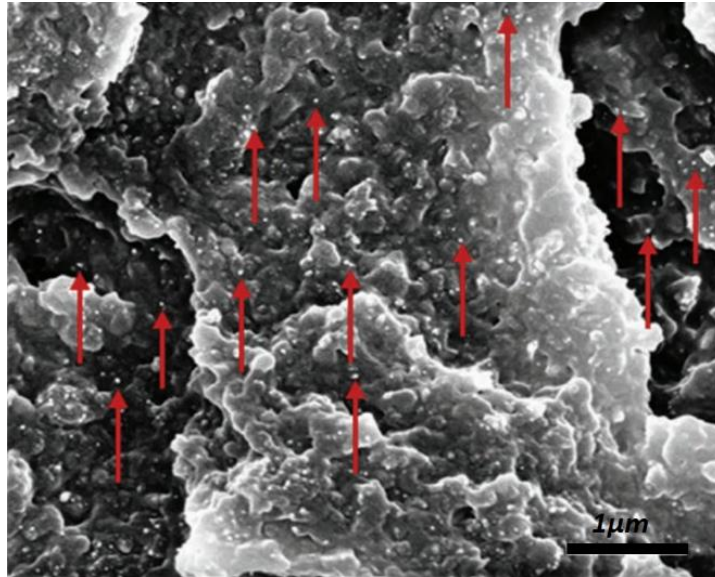


Figure 64. SEM image of a 3D-printed textured cellular microstructure using 20 wt% acetylated cellulose nanocrystal cylindrical shape nanoparticles [102].

As mentioned in chapter 1 and 2 natural and biological materials are thought to benefit from hierarchical architecture of staggered structure in different length scales from nano- to mesoscale. Indeed, one of the primary goals of biomimicry is developing the staggered structure and its underlying mechanisms to simultaneously enhance the strength and toughness of materials. A couple of key points can be understood from the batch of 17%Si-nHA/SOEA+HEA ink, including (i) despite the fact that HEA makes SOEA weaker, it decreases the SOEA viscosity and the ink rheology. Consequently, nanoparticles can be non-uniformly dispersed without agglomerations, and this rheology facilitates the dynamics of nanoparticles and shear stress rate behavior during 3D-printing in nozzle tip. (ii) Both 20%Si-nHA/SOEA and 17%Si-nHA/SOEA+HEA inks were

reinforced using same nanoparticles; however, the staggered nanostructure in latter one was substantially better than the former one. This is Similar to high-performance natural and biological materials which comprise of a weak and compliant matrix reinforced by stiff nanoparticles in a staggered structure. This batch of ink also was reinforced with a well dispersed and aligned nanostructure; thus, its performance was superior compared with 20%Si-nHA/SOEA which has remarkably stronger matrix but with an imperfectly staggered nanostructure particularly in the middle of filament. Based on Figures 32-35, by increasing Si-nHA volume fraction, inclusion misalignments tend to be increased. This issue is directly related to increasing viscosity and rheology of this ink because unlike Si-nHA/SOEA+HEA ink, the difference between results of both nozzle tips in this ink is relatively negligible. The influences of these mentioned points were easily observed in the stiffness comparisons results presented in Figures 60 (a) and (b).

The importance of accurately considering the shape, size and three-dimensional non-uniform dispersion of inclusions in biomimetic composites is highlighted through the results presented in chapter 6. According to Figure 51, the need to consider a 3D analysis versus a 2D ‘plane strain’ analysis, which is often assumed in many analytical and computational models of biomimetic composites, were presented in Chapter 6. The reason for discrepancy in Figure 51 stems from the inclusion cross-sectional shape and the corresponding inclusion dispersion. Based on the tri-histogram plots in Figures 18 and 19, the variations of theta and phi for cylindrical inclusions are lower than hexagonal platelet. This implies that cylindrical inclusions can achieve better packing than hexagonal (rectangular cross-section) inclusions [76]. This increases the efficiency of the load transfer from the matrix to the inclusions, thus leading to a stiffer RVE relative to the hexagonal platelet RVE at the same volume fraction [43]. Therefore, a 2D RVE model under predicts the stiffness of cylindrical inclusion biomimetic composites in the fiber direction. Furthermore, 2D

RVEs cannot provide all the orthotropic elastic constants, whereas 3D RVEs can. The results presented in Figure 52 and 53 demonstrate that unlike the hexagonal platelet model, in the cylindrical inclusion model, elastic coefficients were not sensitive to aspect ratios (ρ), except for E_1 and ν_{23} . This was expected for cylindrical inclusion due to their transversely isotropic responses. Understanding this issue can be effective in passing several obstacles in generating and applying biomimetic composites. The presented results for two different biomimetic composites have demonstrated that 3D RVEs with realistic non-uniform staggered inclusion dispersions that account for appropriate inclusion size and geometry, are critical for assessing their mechanical behavior. In fact, the local constraining effects for higher volume fractions can only be captured with such a model. Thus, the effect of the third dimension and the ability to simulate the actual response of inclusion-reinforced biomimetic composites in all directions is a significant advancement. Employing the SHCA for generating non-uniformly staggered and aligned 3D RVEs of two different biomimetic composites can be an effective method due to its straightforward and rapid nature. Consequently, not only can orthotropic elastic constants be evaluated, but also, in future work, the generated 3D RVEs may be used to predict the onset and evolution of local damage and cracking in different inclusion-reinforced biomimetic composites as well as local nonlinear or time-dependent behavior. Furthermore, these micromechanical models can be an applicable and efficacious tool in designing a variety of new composite material systems and optimizing their microstructures.

It can be eventually noted that based on comparative studies presented in Section 6.1 and 6.2.3, the 3D RVEs had relatively good and acceptable predictions for nano-scale inclusions; while their predictions for micro-scale inclusions were more reliable. This can depict the importance, challenges, and obstacles for fabricating the staggered nanostructures with simultaneous high

mechanical performances such as bone. Both 3D RVE models were validated with micro-scale inclusion in Section 6.1. Therefore, 3D RVE model can be a reference model of non-uniformly dispersed and perfectly aligned inclusions structure for different length scales based on the inclusion size. Accordingly, the smallest discrepancy between experimental and 3D RVE results means that batch of 3D-printed nanocomposite have more dispersed and aligned Si-nHA inclusions.

According to Figure 25, 17% Si-nHA/SOEA+HEA ink benefits from the best Si-nHA dispersions and alignments; thus, the smallest discrepancy among experimental, 3D RVE, Mori-Tanka results is in this ink. Moreover, the discrepancy between results of two nozzle tip diameters (D_n) 0.26 and 0.41 mm tends to be decreased by increasing Si-nHA volume fraction. This point is directly related to the observations from Figures 32-35, when Si-nHA dispersions and alignments in higher volume fractions were relatively analogous. Figure 61 (b) demonstrates E_1 versus volume fraction for Si-nHA/SOEA filaments which were 3D-printed using two nozzle tip sizes. This figure also shows a comparison of 3D RVE, Mori-Tanaka, and experimental results. Unlike Si-nHA/SOEA+HEA filaments, the discrepancy between experimental and 3D RVE results in this ink is notably greater than Si-nHA/SOEA+HEA presented in Figure 61 (a). However, based on the extensive difference between Young's modulus of SOEA and Si-nHA, 3D RVE and experimental results are still in the same trend and close to each other. Mori-Tanaka is entirely fitted with experimental result in 10% Si-nHA volume fraction, while according to Figure 36, this batch had the worst inclusion dispersions and alignments. Except 10% Si-nHA volume fraction, Mori-Tanaka increasing trend is entirely different with experimental data. However, by increasing inclusion volume fraction the Mori-Tanaka results tend to be closer to 3D RVE results. As it was expected, for each constant, the behaviors of both nanocomposites are identical due to non-uniformly dispersed and analogous

inclusion shapes; while, values are different because of the distinct elastic properties of matrices. Another significant parameter which has an integral effects on discrepancies between experimental and numerical results in Figures 60 (a) and (b) is the elastic properties of nanohydroxyapatite particles (nHA). The elastic properties of nHA presented in Table 3 and used for 3D RVE models were found in literature with approximately same percentage of crystalline phase. However, using the actual properties of nHA particle would make the results more accurate and reliable.

Although 3D RVE and Mori-Tanaka overestimated E_1 , results are still comparable with some batches of experimental results. 3D RVE model benefits from several potentials which Mori-Tanaka model is not able to capture them. Example of these shortcomings are listed as follows:

- (i) Considering exact inclusion shapes and dispersions
- (ii) Capturing local stress distribution and concentration
- (iii) Defining mechanical properties for inclusion and matrix interfaces
- (iv) Predicting the onset of fracture and also damage evolution.

All in all, due to abovementioned shortcomings in regard to Mori-Tanaka model, 3D FE micromechanical models are the potential and more reliable candidate as the computational tool.

Chapter 8: Conclusions

8.1. Conclusions

Three-dimensional FE micromechanical models were developed to virtually assess the mechanical performances of different nano- and micro-scale biomimetic materials prior to fabrication and experimental tests.

A new effective algorithm named staggered hard-core algorithm (SHCA) was developed for rapidly generating three-dimensional periodic staggered and aligned non-uniformly dispersed multi-inclusion representative volume elements (RVEs) for modeling the response of biomimetic composites. The resulting 3D RVE geometries were implemented in the commercial finite element software ABAQUS for micromechanical assessment using customized PYTHON scripts. Volume-averaged orthotropic elastic properties were subsequently computed and compared with available experimental data and well-known analytical models, revealing good correlation for low inclusion volume fractions. Although deemed true for all high inclusion volume fraction biomimetic composites, this was particularly the case for composites with cylindrical inclusions where a 3D assessment in lieu of a reduced 2D plane strain assessment is necessary for accurate microstructural representation. Furthermore, a comparative study of orthotropic elastic constants was performed for the cylindrical and hexagonal inclusion biomimetic composites studied. A distinct response to varying inclusion volume fractions and aspect ratios was revealed for each material system, providing insight for future material system design efforts. Also, the effects of inclusion properties, shape, aspect ratio and volume fraction on the mechanical properties of these materials were virtually investigated.

Two 3D-printable nanocomposite inks with various inclusion volume fractions were made to fabricate bone-mimetic filaments. Two different biopolymeric matrices were utilized for these nanocomposite inks including a vegetable oil-based polymer (soybean oil deoxidized acrylate (SOEA)) and SOEA+2-hydroxyethyl acrylate (HEA). These two biopolymeric resins were reinforced using various volume fractions of salinized nanohydroxyapatite (Si-nHA). A number of filaments were 3D-printed using two different nozzle tip sizes for both Si-nHA/SOEA and Si-nHA/SOEA+HEA nanocomposite inks. SEM observations demonstrated the better Si-nHA dispersions and alignments in siding regions compared with the middle of filament.

Several tensile tests were conducted on both biopolymeric resins using the dog-bone specimens, and thus their mechanical performances were measured. The results exhibited that the SOEA was remarkably stronger and stiffer compared to SOEA+HEA. Additionally, a number of tensile tests were implemented on 3D-printed nanocomposite filaments to extract stress-strain behavior and measure Young's modulus in the longitudinal direction. The results showed that by increasing Si-nHA volume fraction the strength and toughness of both 3D-printed nanocomposite filaments tend to be enhanced and decreased respectively; while their stiffness was linearly increased. However, in 17% Si-nHA/SOEA+HEA batch, both strength, and toughness were interestingly improved.

Furthermore, several 3D FE micromechanical models (3D RVEs) and well-established analytical model (Mori-Tanaka) were used based on material properties and volume fractions of both biopolymeric resins and nanoparticles. The computed Young's modulus from these micromechanical models was compared with experimental data for both 3D-printed nanocomposite inks. These comparisons revealed that 3D RVEs were able to simulate the relatively linear increase of Young's modulus versus increasing inclusion volume fraction. The predictions of 3D RVEs were relatively close to 3D-printed Si-nHA/SOEA+HEA ink. The 3D

RVEs results had remarkably better correlation for 3D-printed Si-nHA/SOEA+HEA ink compared to 3D-printed Si-nHA/SOEA ink. Mori-Tanaka predictions also were closed to experimental and 3D RVEs results for lower inclusion volume fractions in both 3D-printed nanocomposites. Eventually, orthotropic elastic constants were calculated using 3D RVEs for both nanocomposite inks.

8.2. Recommendations for future works

The following is a list of the main recommendations for the developed 3D FE micromechanical model:

- (i) Using developed 3D FE micromechanical models with misaligned inclusion can be more accurate and reliable. It was indicated in Section 5.1 that the SHCA can be modified and enable to generate the different degree of misaligned inclusions.
- (ii) Using a modified version of SHCA, 3D RVEs with different size of inclusion can be generated.
- (iii) Using the actual properties of nHA particle would make the results more accurate and reliable.
- (iv) The properties of nHA are sensitive to percentages of the crystalline phase. Due to various limitations in measuring nanoparticle properties, a parametric study can be performed to assess the sensitivity of developed models on changing nHA properties.
- (v) Various damage criteria and models can also be executed on these 3D FE micromechanical models to predict crack initiation and propagation. The ability of damage assessment will make these models a full-range computational tool.
- (vi) The inverse version of Mori-Tanka model can be implemented and compared with numerical and experimental results to assess its prediction ability for higher volume fractions.

(vii) The total simulation time for higher volume fractions models approximately was 24 h. Indeed, using copy mesh module and dummy element technique requires diminutive mesh size; however, by changing the geometry of models, the number of elements and thus simulation time can be decreased.

The following is a list of the main recommendations with regards to the experimental methods:

(i) 3D-printing filaments with proposed two nanocomposite inks in this study using very long nozzle tips can improve inclusion alignments particularly in the middle of filaments.

(ii) Adding other biopolymers instead of HEA to SOEA can change the rheology of nanocomposite ink which is one of the significant parameters for 3D-printing a non-uniformly staggered nanostructure.

(iii). In order to prove interlocking mechanisms, the crack trajectory and propagation of both 3D-printed nanocomposite inks can be assessed. In addition, by investigating crack initiation and total damage behavior, the mechanical performances of these materials can profoundly be understood.

(iv) By assessing the mechanical performances of these materials under fatigue loading, the merits and drawbacks of these materials can be discovered and improved.

References

- [1] Ritchie, R. O. (2011). The conflicts between strength and toughness. *Nature materials*, 10(11), 817.
- [2] Mann, S. (2001). *Biomineralization: principles and concepts in bioinorganic materials chemistry* (Vol. 5). Oxford University Press on Demand.
- [3] Wegst, U. G., Bai, H., Saiz, E., Tomsia, A. P., & Ritchie, R. O. (2015). Bioinspired structural materials. *Nature materials*, 14(1), 23.
- [4] Lei, H. J., Zhang, Z. Q., Han, F., Liu, B., Zhang, Y. W., & Gao, H. J. (2013). Elastic bounds of bioinspired nanocomposites. *Journal of Applied Mechanics*, 80(6), 061017.
- [5] Jäger, I., & Fratzl, P. (2000). Mineralized collagen fibrils: a mechanical model with a staggered arrangement of mineral particles. *Biophysical journal*, 79(4), 1737-1746.
- [6] Fratzl, P., & Weinkamer, R. (2007). Nature's hierarchical materials. *Progress in Materials Science*, 52(8), 1263-1334.
- [7] Fratzl, P. (2003). Cellulose and collagen: from fibres to tissues. *Current opinion in colloid & interface science*, 8(1), 32-39.
- [8] Studart, A. R. (2016). Additive manufacturing of biologically-inspired materials. *Chemical Society Reviews*, 45(2), 359-376.
- [9] Dimas, L. S., Bratzel, G. H., Eylon, I., & Buehler, M. J. (2013). Tough composites inspired by mineralized natural materials: computation, 3D printing, and testing. *Advanced Functional Materials*, 23(36), 4629-4638.
- [10] Grossman, M., Bouville, F., Erni, F., Masania, K., Libanori, R., & Studart, A. R. (2017). Mineral nano-interconnectivity stiffens and toughens nacre-like composite materials. *Advanced Materials*, 29(8), 1605039.

- [11] Le Ferrand, H., Bouville, F., Niebel, T. P., & Studart, A. R. (2015). Magnetically assisted slip casting of bioinspired heterogeneous composites. *Nature materials*, 14(11), 1172.
- [12] Compton, B. G., & Lewis, J. A. (2014). 3D-printing of lightweight cellular composites. *Advanced materials*, 26(34), 5930-5935.
- [13] Martin, J. J., Fiore, B. E., & Erb, R. M. (2015). Designing bioinspired composite reinforcement architectures via 3D magnetic printing. *Nature communications*, 6, 8641.
- [14] Erb, R. M., Sander, J. S., Grisch, R., & Studart, A. R. (2013). Self-shaping composites with programmable bioinspired microstructures. *Nature communications*, 4, 1712.
- [15] Bargardi, F. L., Le Ferrand, H., Libanori, R., & Studart, A. R. (2016). Biomimetic self-shaping ceramics. *Nature communications*, 7, 13912.
- [16] Feilden, E., Ferraro, C., Zhang, Q., García-Tuñón, E., D'elia, E., Giuliani, F., ... & Saiz, E. (2017). 3D Printing Bioinspired Ceramic Composites. *Scientific reports*, 7(1), 13759.
- [17] Guner, S. G., & Dericioglu, A. F. (2016). Nacre-mimetic epoxy matrix composites reinforced by two-dimensional glass reinforcements. *RSC Advances*, 6(39), 33184-33196.
- [18] Yaraghi, N. A., Guarín-Zapata, N., Grunenfelder, L. K., Hintsala, E., Bhowmick, S., Hiller, J. M., ... & Wuhler, R. (2016). A sinusoidally architected helicoidal biocomposite. *Advanced Materials*, 28(32), 6835-6844.
- [19] Zaheri, A., Fenner, J. S., Russell, B. P., Restrepo, D., Daly, M., Wang, D., ... & Espinosa, H. D. (2018). Revealing the Mechanics of Helicoidal Composites through Additive Manufacturing and Beetle Developmental Stage Analysis. *Advanced Functional Materials*, 28(33), 1803073.
- [20] Gu, G. X., Takaffoli, M., & Buehler, M. J. (2017). Hierarchically enhanced impact resistance of bioinspired composites. *Advanced Materials*, 29(28), 1700060.

- [21] Guiducci, L., Weaver, J. C., Bréchet, Y. J., Fratzl, P., & Dunlop, J. W. (2015). The geometric design and fabrication of actuating cellular structures. *Advanced Materials Interfaces*, 2(11), 1500011.
- [22] Wen, L., Weaver, J. C., & Lauder, G. V. (2014). Biomimetic shark skin: design, fabrication and hydrodynamic function. *Journal of Experimental Biology*, 217(10), 1656-1666.
- [23] Araya, S., Zolotovskiy, K., Veliz, F., Song, J. H., Reichert, S., Boyce, M. C., & Ortiz, C. (2013). presented in part at the International Conference on Education and research in Computer Aided Architectural Design in Europe. *Delft, The Netherlands*.
- [24] Mirkhalaf, M., Dastjerdi, A. K., & Barthelat, F. (2014). Overcoming the brittleness of glass through bio-inspiration and micro-architecture. *Nature communications*, 5, 3166.
- [25] Yin, Z., Dastjerdi, A., & Barthelat, F. (2018). Tough and deformable glasses with bioinspired cross-ply architectures. *Acta biomaterialia*.
- [26] Mirkhalaf, M., Zhou, T., & Barthelat, F. (2018). Simultaneous improvements of strength and toughness in topologically interlocked ceramics. *Proceedings of the National Academy of Sciences*, 115(37), 9128-9133.
- [27] He, J. L., Wang, J., Li, W. Z., & Li, H. D. (1997). Simulation of nacre with TiN/Pt multilayers and a study of their mechanical properties. *Materials Science and Engineering: B*, 49(2), 128-134.
- [28] Almqvist, N., Thomson, N. H., Smith, B. L., Stucky, G. D., Morse, D. E., & Hansma, P. K. (1999). Methods for fabricating and characterizing a new generation of biomimetic materials1. *Materials Science and Engineering: C*, 7(1), 37-43.
- [29] Tang, Z., Kotov, N. A., Magonov, S., & Ozturk, B. (2003). Nanostructured artificial nacre. *Nature materials*, 2(6), 413.

- [30] Bouville, F., Maire, E., Meille, S., Van de Moortèle, B., Stevenson, A. J., & Deville, S. (2014). Strong, tough and stiff bioinspired ceramics from brittle constituents. *Nature materials*, 13(5), 508.
- [31] Hunger, P. M., Donius, A. E., Wegst, U. G., 2013. Platelets self-assemble into porous nacre during freeze casting. *J. Mech. Behav. Biomed. Mater* 19, 87-93.
- [32] Walther, A., Bjurhager, I., Malho, J. M., Pere, J., Ruokolainen, J., Berglund, L. A., & Ikkala, O. (2010). Large-area, lightweight and thick biomimetic composites with superior material properties via fast, economic, and green pathways. *Nano letters*, 10(8), 2742-2748.
- [33] Yao, H. B., Tan, Z. H., Fang, H. Y., & Yu, S. H. (2010). Artificial Nacre-like Bionanocomposite Films from the Self-Assembly of Chitosan–Montmorillonite Hybrid Building Blocks. *Angewandte Chemie International Edition*, 49(52), 10127-10131.
- [34] Zhu, W., Lu, C. H., Chang, F. C., & Kuo, S. W. (2012). Supramolecular ionic strength-modulating microstructures and properties of nacre-like biomimetic nanocomposites containing high loading clay. *RSC Advances*, 2(15), 6295-6305.
- [35] Mirkhalaf, M., Barthelat, F., 2016. Nacre-like materials using a simple doctor blading technique: Fabrication, testing and modeling. *J. Mech. Behav. Biomed. Mater*, 56, 23-33.
- [36] Andres, C. M., Kotov, N. A., 2010. Inkjet deposition of layer-by-layer assembled films. *J. American Chem. Soc* 132(41), 14496-14502.
- [37] Bonderer, L. J., Feldman, K., & Gauckler, L. J. (2010). Platelet-reinforced polymer matrix composites by combined gel-casting and hot-pressing. Part I: Polypropylene matrix composites. *Composites Science and Technology*, 70(13), 1958-1965.

- [38] Bonderer, L. J., Feldman, K., & Gauckler, L. J. (2010). Platelet-reinforced polymer matrix composites by combined gel-casting and hot-pressing. Part II: Thermoplastic polyurethane matrix composites. *Composites Science and Technology*, 70(13), 1966-1972.
- [39] Erb, R. M., Libanori, R., Rothfuchs, N., & Studart, A. R. (2012). Composites reinforced in three dimensions by using low magnetic fields. *Science*, 335(6065), 199-204.
- [40] Sharp, E. L., Al-Shehri, H., Horozov, T. S., Stoyanov, S. D., & Paunov, V. N. (2014). Adsorption of shape-anisotropic and porous particles at the air–water and the decane–water interface studied by the gel trapping technique. *RSC Advances*, 4(5), 2205-2213.
- [41] Wei, M., Zhi, D., & Brandon, D. G. (2005). Microstructure and texture evolution in gel-cast α -alumina/alumina platelet ceramic composites. *Scripta materialia*, 53(12), 1327-1332.
- [42] Mura, T. (2013). *Micromechanics of defects in solids*. Springer Science & Business Media.
- [43] Dato, M. H. (2012). *Mechanics of fibrous composites*. Springer Science & Business Media.
- [44] Kaw, A. K. (2005). *Mechanics of composite materials*. CRC press.
- [45] Böhm, H. J. (2016). A short introduction to basic aspects of continuum micromechanics, CDL–FMD Report 3–1998, TU Wien, Vienna.
- [46] Jansson, S. (1992). Homogenized nonlinear constitutive properties and local stress concentrations for composites with periodic internal structure. *International Journal of Solids and Structures*, 29(17), 2181-2200.
- [47] Rao, M. V., Mahajan, P., & Mittal, R. K. (2008). Effect of architecture on mechanical properties of carbon/carbon composites. *Composite Structures*, 83(2), 131-142.

- [48] Rouf, K., Denton, N. L., & French, R. M. (2017). Effect of fabric weaves on the dynamic response of two-dimensional woven fabric composites. *Journal of Materials Science*, 52(17), 10581-10591.
- [49] Bahmani, A., Li, G., Willett, T. L., & Montesano, J. (2018). Three-dimensional microscopic assessment of randomly distributed representative volume elements for high fiber volume fraction unidirectional composites. *Composite Structures*, 192, 153-164.
- [50] Barthelat, F., & Rabiei, R. (2011). Toughness amplification in natural composites. *Journal of the Mechanics and Physics of Solids*, 59(4), 829-840.
- [51] Barthelat, F. (2014). Designing nacre-like materials for simultaneous stiffness, strength and toughness: Optimum materials, composition, microstructure and size. *Journal of the Mechanics and Physics of Solids*, 73, 22-37.
- [52] Begley, M. R., Philips, N. R., Compton, B. G., Wilbrink, D. V., Ritchie, R. O., & Utz, M. (2012). Micromechanical models to guide the development of synthetic 'brick and mortar' composites. *Journal of the Mechanics and Physics of Solids*, 60(8), 1545-1560.
- [53] Zhang, Z. Q., Liu, B., Huang, Y., Hwang, K. C., & Gao, H. (2010). Mechanical properties of unidirectional nanocomposites with non-uniformly or randomly staggered platelet distribution. *Journal of the Mechanics and Physics of Solids*, 58(10), 1646-1660.
- [54] Mirkhalaf, M., & Ashrafi, B. (2017). A numerical study on improving the specific properties of staggered composites by incorporating voids. *Materials Today Communications*, 13, 144-154.
- [55] Eshelby, J. D. (1957). The determination of the elastic field of an ellipsoidal inclusion, and related problems. *Proc. R. Soc. Lond. A*, 241(1226), 376-396.

- [56] Mori, T., & Tanaka, K. (1973). Average stress in matrix and average elastic energy of materials with misfitting inclusions. *Acta metallurgica*, 21(5), 571-574.
- [57] Abid, N., Mirkhalaf, M., & Barthelat, F. (2018). Discrete-element modeling of nacre-like materials: Effects of random microstructures on strain localization and mechanical performance. *Journal of the Mechanics and Physics of Solids*, 112, 385-402.
- [58] Rabiei, R., Bekah, S., & Barthelat, F. (2010). Failure mode transition in nacre and bone-like materials. *Acta biomaterialia*, 6(10), 4081-4089.
- [59] Tang, H., Barthelat, F., & Espinosa, H. D. (2007). An elasto-viscoplastic interface model for investigating the constitutive behavior of nacre. *Journal of the Mechanics and Physics of Solids*, 55(7), 1410-1438.
- [60] Barthelat, F., Tang, H., Zavattieri, P. D., Li, C. M., & Espinosa, H. D. (2007). On the mechanics of mother-of-pearl: a key feature in the material hierarchical structure. *Journal of the Mechanics and Physics of Solids*, 55(2), 306-337.
- [61] Abid, N., Pro, J. W., & Barthelat, F. (2018). Fracture mechanics of nacre-like materials using discrete-element models: Effects of microstructure, interfaces and randomness. *Journal of the Mechanics and Physics of Solids*.
- [62] Ahmadian, H., Yang, M., Nagarajan, A., & Soghrati, S. (2018). Effects of shape and misalignment of fibers on the failure response of carbon fiber reinforced polymers. *Computational Mechanics*, 1-19.
- [63] Ahmadian, H., Liang, B., & Soghrati, S. (2017). An integrated computational framework for simulating the failure response of carbon fiber reinforced polymer composites. *Computational Mechanics*, 60(6), 1033-1055.

- [64] Dai, G., & Mishnaevsky Jr, L. (2014). Graphene reinforced nanocomposites: 3D simulation of damage and fracture. *Computational Materials Science*, 95, 684-692.
- [65] Wang, R., Zhang, L., Hu, D., Liu, C., Shen, X., Cho, C., & Li, B. (2017). A novel approach to impose periodic boundary condition on braided composite RVE model based on RPIM. *Composite Structures*, 163, 77-88.
- [66] Wang, R., Zhang, L., Hu, D., Liu, X., Cho, C., & Li, B. (2017). Progressive damage simulation in 3D four-directional braided composites considering the jamming-action-induced yarn deformation. *Composite Structures*, 178, 330-340.
- [67] Yang, S., Tewari, A., & Gokhale, A. M. (1997). Modeling of non-uniform spatial arrangement of fibers in a ceramic matrix composite. *Acta Materialia*, 45(7), 3059-3069.
- [68] Melro, A. R., Camanho, P. P., & Pinho, S. T. (2008). Generation of random distribution of fibres in long-fibre reinforced composites. *Composites Science and Technology*, 68(9), 2092-2102.
- [69] Romanov, V., Lomov, S. V., Swolfs, Y., Orlova, S., Gorbatikh, L., & Verpoest, I. (2013). Statistical analysis of real and simulated fibre arrangements in unidirectional composites. *Composites Science and Technology*, 87, 126-134.
- [70] Jodrey, W. S., & Tory, E. M. (1985). Computer simulation of close random packing of equal spheres. *Physical review A*, 32(4), 2347.
- [71] Yang, L., Yan, Y., Ran, Z., & Liu, Y. (2013). A new method for generating random fibre distributions for fibre reinforced composites. *Composites Science and Technology*, 76, 14-20.
- [72] Buryachenko, V. A., Pagano, N. J., Kim, R. Y., & Spowart, J. E. (2003). Quantitative description and numerical simulation of random microstructures of composites and their effective elastic moduli. *International journal of solids and structures*, 40(1), 47-72.

- [73] Vaughan, T. J., & McCarthy, C. T. (2010). A combined experimental–numerical approach for generating statistically equivalent fibre distributions for high strength laminated composite materials. *Composites Science and Technology*, 70(2), 291-297.
- [74] Wang, W., Dai, Y., Zhang, C., Gao, X., & Zhao, M. (2016). Micromechanical modeling of fiber-reinforced composites with statistically equivalent random fiber distribution. *Materials*, 9(8), 624.
- [75] Zhang, T., & Yan, Y. (2017). A comparison between random model and periodic model for fiber-reinforced composites based on a new method for generating fiber distributions. *Polymer Composites*, 38(1), 77-86.
- [76] Li, G., Sharifpour, F., Bahmani, A., & Montesano, J. (2018). A new approach to rapidly generate random periodic representative volume elements for microstructural assessment of high volume fraction composites. *Materials & Design*, 150, 124-138.
- [77] Eglen, S. J., Lofgreen, D. D., Raven, M. A., & Reese, B. E. (2008). Analysis of spatial relationships in three dimensions: tools for the study of nerve cell patterning. *BMC neuroscience*, 9(1), 68.
- [78] Rodieck, R. W. (2003). The density recovery profile: a method for analysis of points in the plane applicable to retinal studies. *Visual Neuroscience*, 20(3), 349-349.
- [79] Fu, S. Y., Lauke, B., Mäder, E., Yue, C. Y., & Hu, X. (2000). Tensile properties of short-glass-fiber-and short-carbon-fiber-reinforced polypropylene composites. *Composites Part A: Applied Science and Manufacturing*, 31(10), 1117-1125.
- [80] Fritsch, A., Dormieux, L., Hellmich, C., & Sanahuja, J. (2009). Mechanical behavior of hydroxyapatite biomaterials: an experimentally validated micromechanical model for elasticity and strength. *Journal of Biomedical Materials Research Part A: An Official Journal of The*

Society for Biomaterials, The Japanese Society for Biomaterials, and The Australian Society for Biomaterials and the Korean Society for Biomaterials, 88(1), 149-161.

[81] Mujahid, M., Sarfraz, S., & Amin, S. (2015). On the formation of hydroxyapatite nano crystals prepared using cationic surfactant. *Materials Research*, 18(3), 468-472.

[82] Lung, C. Y. K., Sarfraz, Z., Habib, A., Khan, A. S., & Matinlinna, J. P. (2016). Effect of silanization of hydroxyapatite fillers on physical and mechanical properties of a bis-GMA based resin composite. *Journal of the mechanical behavior of biomedical materials*, 54, 283-294.

[83] Patel, N., Best, S. M., Bonfield, W., Gibson, I. R., Hing, K. A., Damien, E., & Revell, P. A. (2002). A comparative study on the in vivo behavior of hydroxyapatite and silicon substituted hydroxyapatite granules. *Journal of Materials Science: Materials in Medicine*, 13(12), 1199-1206.

[84] Porter, A. E., Patel, N., Skepper, J. N., Best, S. M., & Bonfield, W. (2003). Comparison of in vivo dissolution processes in hydroxyapatite and silicon-substituted hydroxyapatite bioceramics. *Biomaterials*, 24(25), 4609-4620.

[85] Hijón, N., Cabanas, M. V., Pena, J., & Vallet-Regí, M. (2006). Dip coated silicon-substituted hydroxyapatite films. *Acta Biomaterialia*, 2(5), 567-574.

[86] Vallet-Regí, M., & Arcos, D. (2005). Silicon substituted hydroxyapatites. A method to upgrade calcium phosphate based implants. *Journal of Materials chemistry*, 15(15), 1509-1516.

[87] Pietak, A. M., Reid, J. W., Stott, M. J., & Sayer, M. (2007). Silicon substitution in the calcium phosphate bioceramics. *Biomaterials*, 28(28), 4023-4032.

[88] Zhang, C., Garrison, T. F., Madbouly, S. A., & Kessler, M. R. (2017). Recent advances in vegetable oil-based polymers and their composites. *Progress in Polymer Science*, 71, 91-143.

- [89] Miao, S., Wang, P., Su, Z., & Zhang, S. (2014). Vegetable-oil-based polymers as future polymeric biomaterials. *Acta biomaterialia*, *10*(4), 1692-1704.
- [90] Miao, S., Zhu, W., Castro, N. J., Nowicki, M., Zhou, X., Cui, H., ... & Zhang, L. G. (2016). 4D printing smart biomedical scaffolds with novel soybean oil epoxidized acrylate. *Scientific reports*, *6*, 27226.
- [91] Martínez-Vázquez, F. J., Cabañas, M. V., Paris, J. L., Lozano, D., & Vallet-Regí, M. (2015). Fabrication of novel Si-doped hydroxyapatite/gelatine scaffolds by rapid prototyping for drug delivery and bone regeneration. *Acta biomaterialia*, *15*, 200-209.
- [92] Wang, L., Weng, L., Song, S., Zhang, Z., Tian, S., & Ma, R. (2011). Characterization of polyetheretherketone–hydroxyapatite nanocomposite materials. *Materials Science and Engineering: A*, *528*(10-11), 3689-3696.
- [93] Liu, H., & Webster, T. J. (2010). Mechanical properties of dispersed ceramic nanoparticles in polymer composites for orthopedic applications. *International journal of nanomedicine*, *5*, 299.
- [94] Wang, L., Weng, L., Song, S., & Sun, Q. (2010). Mechanical properties and microstructure of polyetheretherketone–hydroxyapatite nanocomposite materials. *Materials Letters*, *64*(20), 2201-2204.
- [95] Wozniak, M., Graule, T., de Hazan, Y., Kata, D., & Lis, J. (2009). Highly loaded UV curable nanosilica dispersions for rapid prototyping applications. *Journal of the European Ceramic Society*, *29*(11), 2259-2265.
- [96] Wozniak, M., de Hazan, Y., Graule, T., & Kata, D. (2011). Rheology of UV curable colloidal silica dispersions for rapid prototyping applications. *Journal of the European Ceramic Society*, *31*(13), 2221-2229.

- [97] Standard, A. S. T. M. D638-14, 2014. Standard test method for tensile properties of plastics. ASTM International, West Conshohocken, PA.
- [98] Akbarzadeh, A. H., Abedini, A., & Chen, Z. T. (2015). Effect of micromechanical models on structural responses of functionally graded plates. *Composite Structures*, *119*, 598-609.
- [99] Abedini, A., & Chen, Z. T. (2014). A micromechanical model of particle-reinforced metal matrix composites considering particle size and damage. *Computational Materials Science*, *85*, 200-205.
- [100]Mortazavian, S., & Fatemi, A. (2015). Effects of fiber orientation and anisotropy on tensile strength and elastic modulus of short fiber reinforced polymer composites. *Composites part B: engineering*, *72*, 116-129.
- [101]Hausmann, M. K., Rühls, P. A., Siqueira, G., Läuger, J., Libanori, R., Zimmermann, T., & Studart, A. R. (2018). Dynamics of Cellulose Nanocrystal Alignment during 3D Printing. *ACS nano*, *12*(7), 6926-6937.
- [102]Siqueira, G., Kokkinis, D., Libanori, R., Hausmann, M. K., Gladman, A. S., Neels, A., ... & Studart, A. R. (2017). Cellulose nanocrystal inks for 3D printing of textured cellular architectures. *Advanced Functional Materials*, *27*(12), 1604619.